# Differential Equation Models for Understanding Phenomena beyond Experimental Capabilities

by

Wendy K. Caldwell

A Dissertation Presented in Partial Fulfillment
of the Requirements for the Degree
Doctor of Philosophy

Approved April 2019 by the
Graduate Supervisory Committee:

Stephen Wirkus, Chair
Erik Asphaug
Erika T. Camacho
Sharon Crook
Catherine S. Plesko
Hal Smith

ARIZONA STATE UNIVERSITY

May 2019

ABSTRACT

Mathematical models are important tools for addressing problems that exceed experimental capabilities. In this work, I present ordinary and partial differential equation (ODE, PDE) models for two problems: Vicodin abuse and impact cratering.

The prescription opioid Vicodin is the nation's most widely prescribed pain reliever. The majority of Vicodin abusers are first introduced via prescription, distinguishing it from other drugs in which the most common path to abuse begins with experimentation. I develop and analyze two mathematical models of Vicodin use and abuse, considering only those patients with an initial Vicodin prescription. Through adjoint sensitivity analysis, I show that focusing efforts on prevention rather than treatment has greater success at reducing the total population of abusers. I prove that solutions to each model exist, are unique, and are non-negative. I also derive conditions for which these solutions are asymptotically stable.

Verification and Validation (V&V) are necessary processes to ensure accuracy of computational methods. Simulations are essential for addressing impact cratering problems, because these problems often exceed experimental capabilities. I show that the Free Lagrange (FLAG) hydrocode, developed and maintained by Los Alamos National Laboratory, can be used for impact cratering simulations by verifying FLAG against two analytical models of aluminum-on-aluminum impacts at different impact velocities and validating FLAG against a glass-into-water laboratory impact experiment. My verification results show good agreement with the theoretical maximum pressures, and my mesh resolution study shows that FLAG converges at resolutions low enough to reduce the required computation time from about 28 hours to about 25 minutes.

Asteroid 16 Psyche is the largest M-type (metallic) asteroid in the Main Asteroid

Belt. Radar albedo data indicate Psyche's surface is rich in metallic content, but estimates for Psyche's composition vary widely. Psyche has two large impact structures in its Southern hemisphere, with estimated diameters from 50 km to 70 km and estimated depths up to 6.4 km. I use the FLAG hydrocode to model the formation of the largest of these impact structures. My results indicate an oblique angle of impact rather than a vertical impact. These results also support previous claims that Psyche is metallic and porous.

# DEDICATION

*For my family, for their endless love, support, and encouragement. I could not have done this without you.*

*Mama, Daddy, Mike, and Laura: You are the best parents a girl could ask for.*

*Misty: You are the greatest sister and friend. Your daily texts made this possible.*

*Paw: I wish you were still alive to see me now. I think you would be proud.*

*To the women in my family: Thank you for defying gender roles. I never grew up thinking I shouldn't have a career, that I shouldn't be smart, or that I shouldn't be good at math. You inspire me every day. Thank you for giving me someone to admire.*

ACKNOWLEDGMENTS

It would be impossible to acknowledge everyone who helped me along this journey in the short space I have been allotted, but, nevertheless, I will try. First and foremost, I had the most incredible adviser. Thank you, Steve, for believing in me, guiding me, and talking me off the math ledge every semester. I had the incredible privilege of finishing my last two years at LANL. Cathy and Abby, thanks for sharing your expertise with me and for being amazing mentors. I have learned so much from both of you.

I am grateful to my committee for their guidance and expertise, which has made this a stronger dissertation. I have learned and grown so much because of each of you. Erika, thank you being what every little math girl wants to be when she grows up. Sharon, thank you for your career advice and academic guidance. Hal, thank you for your encouraging words throughout my graduate career. Erik, thank you for helping me think of research topics applicable to both applied mathematics and planetary science.

To my professors at ASU and UTK (Go Vols!), I cannot thank you enough for all you have taught me. There are far too many of you to name here. Oliver Beckstein, thank you for your patience as I learned to navigate the differences between the worlds of mathematics and physics. Conrad Plaut, thank you for believing in me and recognizing my potential. Jochen Denzler, thank you for going out of your way to help me understand differential equations. Paul Bourdon, thank you for teaching me how to write a proper proof – it made me a better mathematician. Morwen Thistlethwaite, thank you for your mentorship and encouragement. Yang Kuang, thank you for your flexibility during my concussion – this stuff is hard enough without brain damage.

I could not have survived grad school without my amazing ASU family. Theresa, you were my first and best ASU friend. Morgan and Emily, thanks for the girls'

nights and hand pants. Danielle and Katie, we won't always be office mates but we will always be math sisters. Jennifer and Erika, you were great office mates and friends. Terri and John, I am so glad I ended up with an office on your floor.

To my LANL colleagues, this work would not have been possible without your support. Nick and Brandon, thanks for teaching me how to untangle meshes and fix tiny time steps. Chris, thanks for being my go-to guy for debugging and general questions. Miles, thanks for helping me with porosity and material models. Jimmy, thanks for being a great group leader and for reading this entire dissertation. Rob and the computer gods, thanks for letting me be first in line to run my huge asteroid simulations. Louise Mendius, thanks for making this more readable.

I have the most amazing fiancé. Nicolas, thank you for flying to visit me every other weekend, especially the last few months when all I did was work on my dissertation or sleep. Je t'aime pour toujours.

To my family, thank you for always believing in me. To Katie, thank you for being my first Arizona friend. Judy, Paul, Teri, Shawna, James: thanks for being my Arizona family.

This work was supported in part by the National Science Foundation (NSF Grant DMPS-1263374), the National Security Agency (NSA Grant H98230-13-1-0261), the Office of the President of Arizona State University, the Office of the Provost of Arizona State University (ASU), the Center for Space and Earth Science Emerging Ideas Space Science program, the Graduate College at ASU, the Advanced Simulation and Computing (ASC)–Integrated Codes (IC) and the ASC–Threat Reduction (TR) programs at LANL. Los Alamos National Laboratory, an affirmative action/equal opportunity employer, is operated by Triad National Security, LLC, for the National Nuclear Security Administration of the U.S. Department of Energy under contract 89233218NCA000001.

TABLE OF CONTENTS

CHAPTER Page

CHAPTER Page

CHAPTER Page

CHAPTER Page

LIST OF TABLES

Table Page

Table Page

LIST OF FIGURES

Figure Page

Figure Page

Figure Page

Chapter 1

# INTRODUCTION

Mathematical models are an essential tool to understanding problems that exceed experimental capabilities. Early models provided a general understanding but lacked the complexity needed to capture all of the relevant dynamics. As the field of applied mathematics grew, mathematical modeling techniques became more complex. Today, mathematical models are capable of describing phenomena on much larger spatial and temporal scales.

With the rise of supercomputing, complex problems can be solved numerically at much less computational expense. Supercomputers allow modeling of individual particles in fluid flows, shock wave propagation through a variety of materials, and simulations of subatomic particles. Supercomputers can simulate these problems in three dimensions, giving a much more accurate representation of these phenomena. From the mid-1960 to the mid-1970s, computers were first able to perform one million ($1 \times 10^6$) floating point operations per second (FLOPS). In the late 1990s, that number was increased by six orders of magnitude to one trillion ($1 \times 10^{12}$) FLOPS. Today, supercomputers like Trinity at Los Alamos National Laboratory are capable of speeds on the order of petaflops ($1 \times 10^{15}$), one quadrillion floating point operations per second [81].

This thesis consists of two primary subjects, ordinary differential equation (ODE) modeling of Vicodin abuse in the United States and computational partial differential equation (PDE) modeling of impact crater formation. Because of the difference in subject matter, this introduction serves as an introduction to the thesis itself rather than an introduction to each topic in this work. Subject-specific introductions precede

each part to assist the reader in understanding the content that lies ahead.

## 1.1 Mathematical Biology

Problems in mathematical biology often exceed experimental capabilities because of ethical constraints. To understand the spread of human immunodeficiency virus (HIV), for example, it is unacceptable to infect select individuals with HIV and then monitor how the infection spreads. Furthermore, to model in vivo processes, laboratory experiments would be unable to replicate the correct environment. For problems like these, mathematical modeling has proven to provide valuable contributions to the field without experimentation.

HIV models have been used to describe the infection process at the cellular level by modeling both viral infection and clearance [108]. For some infectious diseases, such as hepatitis and HIV, transmission can occur through contact with an infected individual or from mother to offspring through the placenta [129]. For these diseases, modeling can provide insight into when such diseases give rise to epidemics [129].

For physiology and biophysics applications, models have been used to describe biological processes in vivo. Modeling of the giant muscular protein titin has shown that its behavior in the body often mimics that of a spring [54]. Modeling of the squid giant axon highlighted the role of sodium and potassium ions in the membrane [63]. Coupled oscillator models have been used in neuroscience applications to describe axonal delay [40]. Mathematical models of photoreceptor interactions have contributed to the understanding of the degenerative eye condition retinitis pigmentosa [31].

In addition to biological and biophysical applications, mathematical modeling has been used to describe social and behavioral phenomena. Models describing substance use and abuse have provided insight into these problems. Models have been used to describe smoking tobacco [76], drinking alcohol [101, 118], and using heroin [145].

Mathematical models have also been used to describe psychological conditions such as bulimia [142] and bipolar disorder [41].

Mathematical models often have the benefit of providing results relatively immediately, whereas awaiting experimental results and data can take from days to years. Forecasting and nowcasting techniques coupled with computing capability have led to forecasting models that can predict future epidemics with reasonable accuracy by supplementing surveillance data with Internet data streams [13, 51, 60, 112, 116]. Providing meaningful predictions is one advantage of using mathematical models.

## 1.2 Planetary Science

Problems in planetary science often exceed experimental capabilities because of spatial and/or temporal scales. Understanding the formation of the universe, for example, would be both too large and would take billions of years. Models, however, can provide insight into key processes. Many terrestrial objects in our solar system contain silicate mantles, yet Mercury consists mostly of iron core material. Modeling simulations have been able to demonstrate how Mercury was likely stripped of its silicate material as a result of collisions [9]. For planetary systems with planets of mass similar to Jupiter, modeling has shown how multiple planets in such a system can develop vastly different orbits [89].

Models have also been used to predict the current state of bodies in the solar system, such as the composition of Mars [80]. Modeling lightcurves from asteroids with large light variations provided insight into relations for scattering properties [135]. Computer simulations were able to provide predictions for the Lunar Crater Observation and Sensing Satellite (LCROSS) mission by modeling both crater formation and the resulting vapor plume [75]. Modeling the current status of solid bodies in the solar system can provide meaningful predictions for expectations related to upcoming

missions to these bodies.

## 1.3 Thesis Summary

Chapter 2 provides a more detailed introduction to the mathematical biology modeling in this work. This chapter describes the familiar $SIR$ (susceptible-infected-recovered) compartmental ODE model that is widely accepted as the inaugural population model for infectious disease spread. This chapter provides an overview of how these models are used to understand epidemiology, providing a foundation for the following two chapters.

Chapter 3 introduces the U.S. drug abuse problem concerning the prescription opioid Vicodin. In this chapter, I develop and analyze two mathematical models using an extension of the $SIR$ approach described in Chapter 2. Using sensitivity analysis, I examine parameters associated with treatment and prevention to determine those parameters that are the most effective in mitigating the Vicodin abuse problem. To my knowledge, the models in this chapter are the first to address the prescription drug epidemic using population-level ODEs, as well as the first models to address Vicodin specifically.

Chapter 4 provides a detailed mathematical analysis of nonlinear SIAD model presented in Chapter 3. In this chapter, I focus on demonstrating the biological relevance of the model by proving that solutions to the model are non-negative and finite for all finite positive time. I also prove that the model has a solution that exists and is unique. Finally, I examine the positive steady state, including determining conditions under which this steady state exists.

Chapter 5 provides a more detailed introduction to the impact cratering modeling in this work. For these models, I rely on hydrodynamics code (hydrocode) modeling to capture the important physics and solid mechanics in impact crater formation.

This chapter introduces the components of hydrocode modeling, providing a foundation for the following two chapters.

Chapter 6 contains the verification and validation study I use to demonstrate that the FLAG hydrocode is capable of impact cratering simulations. In this chapter, I consider two verification problems and one validation problem deemed to have acceptable benchmarks by the planetary science community. In addition to following the benchmark problem setup, I also use constitutive models in the verification problem to demonstrate FLAG's capability to model solid materials. I compare my results to theoretical results in the verification problem and experiment results in the validation problem. I also include 3D results of the verification problem. The work in this chapter demonstrates that FLAG is an acceptable hydrocode for modeling crater formation.

Chapter 7 explores models of Asteroid 16 Psyche's largest impact crater. In 2D, I simulate the impact and resulting crater using a variety of materials for both Psyche and impactor. I compare these results to the estimated dimensions of the actual crater. I then choose one material, the nickel alloy Monel, as both Psyche and impactor in a porosity study. In this study, I vary the porosity of Psyche from 30% to 80% to determine its effect on the crater size and dimensions. In 3D, I vary the impact angle and porosity to simulate the formation of the crater.

Chapter 8 summarizes my conclusions from each chapter. In this chapter, I also discuss ongoing work and possible future work.

Chapter 2

# INTRODUCTION TO SIR MODELING WITH ORDINARY DIFFERENTIAL EQUATIONS

Mathematical models have long been used to describe natural phenomena, and ordinary differential equation models are particularly poignant for addressing research questions about quantities that change over time. As the field of applied mathematics grew, mathematical modeling techniques became more complex. Mathematical models are particularly useful when experiments are not feasible. Many factors affect the ability of a problem to be explored through experimentation, among them ethical concerns, legal limitations, and spatial and/or temporal scale.

## 2.1 Classic $SIR$ Model

The classic $SIR$ model, sometimes referred to as the Kermack-McKendrick model, describes the flow of individuals through stages of susceptibility, infection, and recovery [73]. In the familiar notation associated with this model, $S$ represents the population of individuals susceptible to a disease, $I$ represents the population of individuals infected with the disease, and $R$ represents the population of individuals who have recovered from the disease. The positive parameters $\beta$ and $\gamma$ represent the infection and removal rates, respectively [73]. Thus, the standard model is [73, 102]:

$$\begin{aligned} \frac{dS}{dt} &= -\beta SI \\ \frac{dI}{dt} &= \beta SI - \gamma I \\ \frac{dR}{dt} &= \gamma I. \end{aligned}$$

The model transmission is considered mass action if $S, I$, and $R$ are population densities and pseudo mass action if these variables represent scalar quantities [52]. As evident in the model equations, this model assumes a constant population, i.e.,

$$\frac{dS}{dt} + \frac{dI}{dt} + \frac{dR}{dt} = 0,$$

and the total population $N$ can be defined as

$$S + I + R = N.$$

Initial populations are often denoted with the subscript 0 and are assumed to be non-negative to preserve the biological relevance of the model [102].

## 2.2 $SEIR$ Models

Since introduced in 1927, the $SIR$ model has been adapted to describe a variety of epidemics. A common modification is the inclusion of a compartment of exposed individuals $E$, which accounts for the latency period present in some infections [102]. In the common notation, the parameter $\sigma$ represents the rate at which exposed individuals become infected. In the familiar notation, the $SEIR$ model is [8]:

$$\begin{aligned}
\frac{dS}{dt} &= -\beta SI \\
\frac{dE}{dt} &= \beta SI - \sigma E \\
\frac{dI}{dt} &= \sigma E - \gamma I \\
\frac{dR}{dt} &= \gamma I.
\end{aligned}$$

As in the common $SIR$ model, the $SEIR$ has a constant population, or, equivalently,

$$\frac{dS}{dt} + \frac{dE}{dt} + \frac{dI}{dt} + \frac{dR}{dt} = 0,$$

and the total population $N$ can be defined as

$$S + E + I + R = N.$$

In these types of compartmental models, the average time an individual spends in each compartment can be expressed as the reciprocal of the associated parameter. For example, in the $SIR$ and $SEIR$ models, the average infective period for an individual is $\frac{1}{\gamma}$ [59]. This property of these types of models provides a mechanism for defining parameter values.

$SIR$-type models do not require constant populations. Endemic models that incorporate both births and deaths often have varying total populations. Incorporating birth and death at the same rate $\mu$, and using the same notation as in the previous modeling examples, we have the following $SEIR$ model with a non-constant total population [78]:

$$\begin{aligned} \frac{dS}{dt} &= -\beta SI + \mu - \mu S \\ \frac{dE}{dt} &= \beta SI - (\sigma + \mu) E \\ \frac{dI}{dt} &= \sigma E - (\gamma + \mu) I \\ \frac{dR}{dt} &= \gamma I - \mu R. \end{aligned}$$

This type of model allows individuals to exit the population at various stages in the epidemic process. For this model, the total population $N$ can be defined as

$$S + E + I + R = N \tag{2.1}$$

as before, but the change in $N$ is no longer 0:

$$\frac{dS}{dt} + \frac{dE}{dt} + \frac{dI}{dt} + \frac{dR}{dt} = \mu(1 - S - E - I - R) = \mu(1 - N) \neq 0. \tag{2.2}$$

## 2.3 $SIVD$ Model

Further modifications of the standard $SIR$ model have included additional compartments for recovered individuals. Getz and Lloyd-Smith developed the $SIVD$

model. In this model, recovery is divided into two compartments: $V; D$. The $V$ compartment contains recovered individuals who have recovered and are immune, which Getz and Lloyd-Smith refer to as "naturally vaccinated" individuals, while the $D$ compartment contains the deceased population [52]. In the common notation, the $SIVD$ model is

$$\begin{aligned} \frac{dS}{dt} &= -\beta SI + \rho V \\ \frac{dI}{dt} &= \beta SI - (\gamma_V + \gamma_D) I \\ \frac{dV}{dt} &= \gamma_V I - \rho V \\ \frac{dD}{dt} &= \gamma_D I, \end{aligned} \tag{2.3}$$

where $\gamma_V$ and $\gamma_D$ are the removal rates for the $V$ and $D$ compartments, respectively, and $\rho$ is the rate at which those in $V$ lose their immunity and return to $S$ [52]. The $SIVD$ model is noteworthy in that $\rho$ can also be interpreted as a relapse rate. In this model, as in the standard $SIR$ and $SEIR$ models, the total population $N$ is

$$S + I + V + D = N,$$

and this population is constant, i.e.,

$$\frac{dS}{dt} + \frac{dI}{dt} + \frac{dV}{dt} + \frac{dD}{dt} = 0.$$

## 2.4 $SIR$-type Model for Illicit Drug Use

$SIR$ modeling techniques have been expanded further to include substance abuse. White and Comiskey developed a three-compartment heroin use model [145]. In their model, the infected compartment indicates users not in treatment, and the recovered

compartment indicates users in treatment. In the common notation, the model is

$$\begin{aligned}
\frac{dS}{dt} &= \Lambda - \beta SI - \mu S \\
\frac{dI}{dt} &= \beta SI - \gamma I + \rho IR - (\mu + \delta_I) I \\
\frac{dR}{dt} &= \gamma I - \rho IR - (\mu + \delta_R) R,
\end{aligned}$$

where $\delta_I$ and $\delta_R$ are removal rates that include drug-related deaths and recovery [145]. As usual, the total population $N$ is

$$S + I + R = N.$$

As in the modified $SEIR$ model, this model has a non-constant population [145]:

$$\frac{dS}{dt} + \frac{dI}{dt} + \frac{dR}{dt} = \Lambda - \mu (S + I + R) - \delta_I I - \delta_R R = \Lambda - \mu N - \delta_I I - \delta_R R \neq 0.$$

## 2.5 Basic Reproduction Number $\mathfrak{R}_0$

In $SIR$-type models, an often analyzed value is the basic reproduction number, the number of infections arising from a single infected individual [21]. This value, denoted $\mathfrak{R}_0$, indicates the number of secondary infections expected in a completely susceptible population. The value of $\mathfrak{R}_0$ is crucial to mathematical epidemiology because it is the threshold at which an epidemic occurs. When $\mathfrak{R}_0 < 1$, the disease is contained. When $\mathfrak{R}_0 > 1$, the disease becomes endemic [21].

## 2.6 $SIR$-type Modeling for Vicodin Abuse in the United States

In the following two chapters, I develop and analyze two $SIR$-type models for Vicodin abuse in the United States. These models are, to my knowledge, the first deterministic mathematical models to describe prescription drug abuse and the prescription opioid epidemic as well as the drug Vicodin.

In Chapter 3, I present one linear model and one nonlinear model, and I perform

adjoint sensitivity analysis on each of these models to determine whether treatment or prevention plays a larger role in reducing the number of Vicodin abusers. I use computer simulations to demonstrate how the populations associated with Vicodin use, abuse, and treatment change over time, eventually reaching steady states.

In Chapter 4, I show these models are biologically relevant by proving the model populations are positive and bounded for all positive time. I show that each of these models has a unique solution. Finally, I examine the steady states and basic reproduction $\mathfrak{R}_0$ to better understand the Vicodin abuse problem.

# Chapter 3

# MODELING VICODIN ABUSE

## 3.1 Introduction

Vicodin is the most widely prescribed pain reliever in the United States [93]. Vicodin contains acetaminophen, the active ingredient in Tylenol, and hydrocodone, an opioid analgesic [91]. The United States comprises 4% of the world's population, yet it uses 99% of the world's hydrocodone supply [86]. An increase in Vicodin prescriptions over the past two decades has resulted in a corresponding increase in Vicodin abuse [91]. From 1993 to 2003, Vicodin abuse rates increased from 7% to 16% [37]. In 1999, approximately nine million Americans admitted to using prescription drugs for non-medical reasons [44]. An estimated two million people are currently abusing Vicodin [43].

The most common path to Vicodin abuse begins with a legal prescription and not illegal experimentation, which distinguishes Vicodin from other drugs. Most abusers obtain Vicodin from their own prescription or that of a friend or relative [97]. Vicodin abuse can have a number of serious consequences, among them liver failure, slowed heart rate, difficulty breathing, jaundice, seizure, and death [113]. Many prescribers report being unaware of the drug's potential for chemical and physical dependence, and many patients are not informed of the risk of dependency when they begin taking Vicodin [38, 106].

Educating medical professionals on the risks associated with Vicodin has proven successful in limiting the number of prescriptions [106]. However, 40% of medical professionals indicated they had received no training on these risks. Preventative

measures focused on increasing awareness in physicians, pharmacists, and the general public of the potential for Vicodin abuse have been largely neglected, although this information can enhance the ability to recognize abuse and thus aid in preventing its spread [85, 86]. A study of pharmacists in the United States and Canada indicated that nearly 90% of pharmacists reported that they had refused to fill a prescription when they had concerns of drug abuse, and more than 75% had attempted to contact the prescribing physician when they had such concerns [12]. A program implemented in California to educate prescribers on the risks associated with Vicodin led to a 95% decrease in the number of Vicodin prescriptions at the end of the two-year study [106].

Until late 2014, Vicodin was classified as a Schedule III narcotic [42, 91]. Since then, the United States Drug Enforcement Administration (DEA) has classified Vicodin as a Schedule II drug, a class more heavily regulated [140]. However, the available data since this change in scheduling are not yet sufficient for modeling. I plan to revisit the parameter values after sufficient time since the new drug scheduling has elapsed.

In the following sections, I develop two deterministic mathematical models for the population introduced to Vicodin with a prescription. In each model, I study the dynamics of the population as users transition between compartments representing acute medical use, chronic use, abuse, and treatment. We also allow for re-entry into the abuse compartment through relapse while in treatment. Relapse is an essential component in substance abuse, and substance abuse models for alcohol and heroin have included a relapse component as well [77, 118, 145]. We perform adjoint sensitivity analysis on each model to determine whether parameters associated with prevention or treatment have a greater effect on the population of Vicodin abusers. Through these models, I gain insight into how to address the Vicodin abuse problem

in the United States.

In Section 3.2, I outline the methods I used for this work. I explain the compartmental modeling approach used to develop both models. I also outline the purposes of sensitivity analysis and its common uses. I introduce the adjoint method of sensitivity analysis, which I use to further study both models.

Section 3.3 examines a linear model, the Compartmental Vicodin Transition (CVT) Model, in which the monthly rate of new prescriptions and the relapse rate are constant parameters. I describe the model with a system of ordinary differential equations. I identify ranges for each of the model's parameters, which I derive in Appendix B. Using the adjoint method, I derive the sensitivity equations for the model and plot the sensitivity index of each parameter. Finally, I simulate the model and plot the results.

Section 3.4 examines the Social Interaction with Abuse-Dependent Prescription Rate (SIAD) Model, a nonlinear model in which the relapse term is affected by social interaction between abusers and those in treatment. Additionally, I scale the monthly rate of new prescriptions by a term containing a new awareness/intervention parameter. I believe this parameter can play a role in accounting for the new scheduling of Vicodin. I identify a range for the new parameter and a modified range for the relapse parameter, which I derive in Appendix B. I again employ the adjoint method to derive the sensitivity equations, and I plot the sensitivity index for each parameter. I then simulate the model and plot the results.

I discuss my results and highlight possible future work in Section 3.5. I include details derivations of estimated parameter ranges in Appendix B.

## 3.2 Methods

I used standard compartmental modeling techniques for the population of Vicodin users introduced through prescription. I then employed adjoint sensitivity analysis of the positive steady state to determine which parameter values have the greatest influence on the size of the population of Vicodin abusers.

### *3.2.1 SIR Modeling Approach*

I used a traditional $SIR$ modeling approach with parameter values equal to the transition rates between compartments [59]. The model considers only those individuals with an initial Vicodin prescription; that is, I allow only one entry point into the population. I divided the population of individuals with Vicodin prescriptions into five compartments: acute ($\leq$ 3 months) medical use $M$; chronic ($>$ 3 months) medical use $C_1$ and $C_2$; abuse (use without prescription or inconsistent with prescription instructions) $A$; treatment $T$. I used two compartments for chronic use for a more realistic representation of the prolonged nature of chronic treatment. The additional compartment prevents chronic users from leaving the compartment almost immediately after entering it. Individuals can leave compartments $M$, $C_1$, $C_2$, and $A$ by transitioning to the next compartment. Individuals can exit the $T$ compartment either by successful treatment, in which case they exit the population entirely, or by relapse, in which case they re-enter the $A$ compartment. Individuals can exit the population by ceasing Vicodin use from every compartment except for $A$. The only way to exit the $A$ compartment is by entering the $T$ compartment.

I did not include the possibility of exiting the $A$ compartment through death from overdose for several reasons. Although there are data sources for drug overdose death, many of these sources do not distinguish between prescription opioid overdoses

and other types of drug overdoses. Furthermore, of those that do make such a distinction, the number of overdoses attributed solely to Vicodin, as opposed to other prescription opioids or a combination of Vicodin and another substance, remains unreported. Additionally, while some data sources distinguish between intentional and unintentional overdose, the majority do not. Thus, I excluded death from overdose [11, 33, 34, 103, 107].

I described the population of Vicodin users with systems of ordinary differential equations. I measured the population of Vicodin users in number of people. The time steps were in increments of one month. For these models, for data reported in days, I considered 30 days to be equal to one month.

### *3.2.2 Sensitivity Analysis*

Sensitivity analysis is one of several methods used in quantifying uncertainties in a given parameter space [88]. It involves examining partial derivatives of the system with respect to each parameter to obtain a sensitivity index, a quantity used to determine a parameter's effect on the system. Mathematically, sensitivities are partial derivatives of a model variable with respect to a model parameter [32]. The sensitivity index of a variable with respect to a parameter quantifies how small changes in the parameter value result in changes in the variable. Sensitivity analysis can be done either globally or locally. Global sensitivity analysis can identify all uncertainties in a multi-dimensional parameter space [88]. Common techniques include the partial rank correlation coefficient (PRCC) and extended Fourier amplitude sensitivity test (eFAST) methods [88]. Although global sensitivity analysis can offer many insights into a model and its uncertainty, it is often computationally expensive.

Local sensitivity analysis focuses on small perturbations in parameter values and how those changes propagate through the system and affect the final output [55]. Lo-

cal sensitivity analysis is less computationally expensive than its global counterpart, with the benefit of having the potential to provide answers to numerous sensitivity questions in a short period of time [55]. Local sensitivity analysis can be performed through two methods: forward sensitivity analysis and adjoint sensitivity analysis. Forward sensitivity analysis is common with systems involving many variables and relatively few parameters, but this method becomes less feasible with many parameters [32]. Consider a vector of variables $x \in \mathbb{R}^n$ and vector of parameters $p \in \mathbb{R}^m$. To find the sensitivity index $S$ of a variable $x_i$ with respect to a parameter $p_j$, calculate $S = \frac{\partial x_i}{\partial p_j}$ [32].

#### *3.2.2.1 Adjoint Method*

Consider vectors $x \in \mathbb{R}^n$ and $p \in \mathbb{R}^m$ and an objective function $f(x,p) : \mathbb{R}^n \times \mathbb{R}^m \to \mathbb{R}$, and ODE system of a vector $x$ of $n$ variables and a vector $p$ of $m$ parameters [20]. Further consider a constraint function $g(x,p) : \mathbb{R}^n \times \mathbb{R}^m \to \mathbb{R}^n$ satisfying $g(x,p) = 0$ with $\frac{\partial g}{\partial x} = g_x$ nonsingular. The general approach to the adjoint method involves calculating sensitivities of $f$ with respect to $p$ $\left(\frac{\partial f_{x_i}}{\partial p_j}\right)$ by minimizing $f$ subject to the constraint $g$ [20, 32]. For ease of explanation, let $x$ be a function of $p$ so that $f(x,p)$ becomes $f(x(p))$. Note that $\nabla f = f_x x_p$ and $\nabla g = 0$ [20]. Expanding,

$$\nabla g = g_x x_p + g_p = 0,$$

which leads to

$$x_p = -g_x^{-1} g_p$$

when taking advantage of the nonsingular nature of $g_x$ [20]. Substituting into the definition of $\nabla f$ [20]:

$$\nabla f = -f_x g_x^{-1} g_p.$$

This results in the adjoint equation

$$g_x^H \lambda = -f_x^H \tag{3.1}$$

where $H$ denotes the (Hermitian) transpose and $\lambda$ is a vector of adjoint variables [20].

Cao et al. present an integral derivation using the $\lambda$ to represent the Lagrange multiplier vector in [32]. The augmented objective function is [32]:

$$f - \int_0^T \lambda^H g dt.$$

Because $g = 0$, the sensitivity of $f$ with respect to $p$ becomes [32]:

$$\int_0^T \left( \dot{f}_p + \dot{f}_x x_p \right) dt - \int_0^T \lambda^H \left( g_p + g_x x_p + g_{\dot{x}} \dot{x}_p \right) dt,$$

where

$$f(x,p) = \int_0^T \dot{f}(x,t,p) dt.$$

Bradley presents an alternative derivation that also uses the Lagrange multiplier vector in [20]. Define $\mathcal{L} := f + \lambda^H g = f$ because $g = 0$ [20]. Then

$$\begin{aligned} \nabla f = \nabla \mathcal{L} &= f_x \nabla x + \nabla \lambda^H \underbrace{g}_{=0} + \lambda^H \left( g_x \nabla x + g_p \right) \\ &= f_x x_p + \lambda^H \left( g_x x_p + g_p \right), \end{aligned}$$

which becomes $\left( f_x + \lambda^H g_x \right) x_p + \lambda^H g_p$ [20]. Note that when Equation (3.1) holds, the equation for $\nabla f$ becomes

$$\nabla f = \lambda^H g_p.$$

Thus, the adjoint method eliminates the need to calculate $x_p$ and reduces the number of computations required to compute sensitivity indices, particularly when the $p$ vector of parameters is large compared to the $x$ vector of variables [20, 32].

To further describe the process of computing the sensitivity indices, consider an ODE of the form

$$\dot{x} = \bar{h}(x, p, t),$$

so that the implicit form is

$$h\left(x, \dot{x}, p, t\right) = \dot{x} - \bar{h}(x, p, t)$$

with initial conditions of the form $g(x(0), p) = 0$ [20].

The adjoint sensitivity algorithm involves a three-step process for calculating the sensitivity of a variable $x$ with respect to a parameter $p$. The first step of the algorithm is to integrate the implicit ODE $h$ using initial conditions $g$ [20]. The second step uses initial conditions $\lambda(T) = 0$ to cancel terms from the integrand of $\mathcal{L}$ and eliminate the need to calculate $x_p$ explicitly [20]. The third step involves calculating the sensitivity with a reduced integrand as a result of previous substitutions [20]. The three-step algorithm in [20] is in Algorithm 1.

**Algorithm 1** Adjoint Sensitivity Algorithm fot Sensitivity of Model Variable $x$ with Respect to Parameter $p$ [20]

1. Integrate $h = 0$ for $x$ from 0 to $T$ using initial conditions $g$
2. Integrate $f_x + \lambda^H \left(h_x - \nabla h_{\dot{x}}\right) - \dot{\lambda}^H h_{\dot{x}} = 0$ for $\lambda$ from T to 0 with initial conditions $\lambda(T) = 0$
3. $f_p = \int_0^T \left(f_p + \lambda^H h_p\right) dt + \lambda^H h_{\dot{x}}\big|_0 \, g_{x(0)}^{-1} g_p$

### 3.3 Compartmental Vicodin Transition Model

I developed and analyzed the Compartmental Vicodin Transition (CVT) model, a linear model of the Vicodin abuse problem. I performed adjoint sensitivity analysis on the model to determine which parameters had the greatest influence on the population of Vicodin abusers. I ran simulations on the model using data-driven parameter values. Table 3.1 lists the ranges for these parameter values. I derive these ranges in Appendix B.

### *3.3.1 Model Description*

The linear model is a system of ordinary differential equations consisting of Equations (3.2)–(3.6). The model considers only those people introduced to Vicodin through their own prescription. I assumed a constant number of new prescriptions per month $\Lambda$. I defined the $M$ compartment to have a maximum time of three months, after which those still using Vicodin transition into $C_1$ at rate $\alpha_1$. Acute users who cease Vicodin treatment before this time exit the population at rate $\alpha_2$. There was no maximum time for either chronic compartment. People can remain chronic users of Vicodin indefinitely, they can stop using Vicodin and exit the population at rate $\beta$, or they can transition into the next compartment at rate $\delta$. While it is likely that the $\beta$ and $\delta$ values are different for the $C_1$ and $C_2$ compartments, available data are not robust enough to assign different values in simulations (e.g. $\delta_1, \delta_2$). Once in the $A$ compartment, people can again stay indefinitely or seek treatment [138, 143]. I considered only one means of exiting this compartment, seeking treatment at rate $\varepsilon$. Once in the $T$ compartment, an individual remains for at least one month and at most 12 months. These durations were because of data that indicate relapses occur overwhelmingly within the first year of treatment and that treatment should last at least one month [22, 98]. Those individuals who successfully complete treatment and stop abusing Vicodin exit the population at rate $\gamma_2$. Those individuals who relapse

re-enter the $A$ compartment.

$$\frac{dM}{dt} = \Lambda - (\alpha_1 + \alpha_2)\, M \tag{3.2}$$

$$\frac{dC_1}{dt} = \alpha_1 M - (\delta + \beta) C_1 \tag{3.3}$$

$$\frac{dC_2}{dt} = \delta C_1 - (\delta + \beta) C_2 \tag{3.4}$$

$$\frac{dA}{dt} = \delta C_2 + \gamma_1 T - \varepsilon A \tag{3.5}$$

$$\frac{dT}{dt} = \varepsilon A - (\gamma_1 + \gamma_2)\, T \tag{3.6}$$

For the purposes of this model, I considered relapse to be returning to pre-treatment abuse levels and not isolated incidents such as taking one pill. Table 3.1 lists the model parameters. $\Lambda$ has unit people, while all other parameters have unit 1/month. Figure 3.1 gives a visual representation of the model.

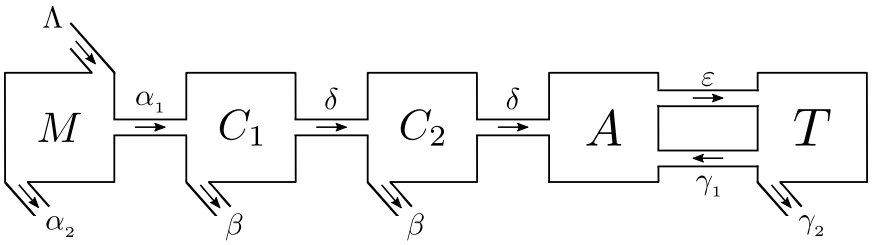


**Figure 3.1:** Diagram Depicting the CVT Model, a Linear Compartmental Model. Users Transition through Acute Medical Use ($M$), Chronic Medical Use ($C_1, C_2$), Abuse ($A$), and Treatment ($T$), with the Possibility of Relapse.

| Parameter | Definition | Value Range<br>Unit |
|---|---|---|
| $\Lambda$ | new Vicodin prescriptions<br>per month | $[2671212, 3303044]$<br>people |
| $\alpha_1$ | monthly rate at which acute users<br>become chronic users | $[0.0377, 0.362]$<br>$\text{month}^{-1}$ |
| $\alpha_2$ | monthly rate at which acute users<br>stop using Vicodin | $[0.0664, 0.962]$<br>$\text{month}^{-1}$ |
| $\beta$ | monthly rate at which chronic users<br>stop using Vicodin | $[0.051, 0.190]$<br>$\text{month}^{-1}$ |
| $\delta$ | monthly rate of chronic users transitioning<br>to the next compartment | $[0.0177, 0.131]$<br>$\text{month}^{-1}$ |
| $\varepsilon$ | monthly rate at which abusers<br>enter treatment | $[0.014, 0.042]$<br>$\text{month}^{-1}$ |
| $\gamma_1$ | monthly constant relapse rate of abusers<br>in treatment | $[0.0375, 0.45]$<br>$\text{month}^{-1}$ |
| $\gamma_2$ | monthly successful treatment rate | $[0.0458, 0.55]$<br>$\text{month}^{-1}$ |

**Table 3.1:** Parameter Value Ranges for the CVT Model. Detailed Derivations of These Ranges are in Appendix B.

### *3.3.2 Derivation of Adjoint Equations*

I considered the CVT model, using the familiar dot notation to represent the time derivative and prime notation $'$ to represent the transpose, to avoid confusion with the $T$ compartment. I used $k$ as an indexing variable to indicate each compartment, where $k \in \{M, C_1, C_2, A, T\}$. I began by rewriting the set of ODEs as a zero matrix

by subtracting the right-hand side from the left-hand side in Equations (3.2)–(3.6):

$$\vec{F}\left(t, \vec{x}, \dot{\vec{x}}, \vec{p}\right) = \begin{bmatrix} \dot{M} - \Lambda + (\alpha_1 + \alpha_2)\, M \\ \dot{C_1} - \alpha_1 M + (\delta + \beta) C_1 \\ \dot{C_2} - \delta C_1 + (\delta + \beta) C_2 \\ \dot{A} - \delta C_2 - \gamma_1 T + \varepsilon A \\ \dot{T} - \varepsilon A + (\gamma_1 + \gamma_2)\, T \end{bmatrix} = 0_{5\times 1},$$

where

$$\vec{x} = \begin{bmatrix} M & C_1 & C_2 & A & T \end{bmatrix}'$$

and

$$\vec{p} = [\Lambda \quad \alpha_1 \quad \alpha_2 \quad \delta \quad \beta\varepsilon \quad \gamma_1 \quad \gamma_2 \quad u_M \quad u_{C_1} \quad u_{C_2} \quad u_A \quad u_T]',$$

where $u_k$ represents initial condition parameters used for computing sensitivity indices of compartment $k$. I then defined a vector $\vec{y(0)}$ that contained the $u_k$ percentage changes of the initial population sizes in each compartment:

$$\vec{y(0)} = \begin{bmatrix} M(0)\,(1 - u_M) \\ C_1(0)\,(1 - u_{C_1}) \\ C_2(0)\,(1 - u_{C_2}) \\ A(0)\,(1 - u_A) \\ T(0)\,(1 - u_T) \end{bmatrix}.$$

I defined the objective function using the integral definition of the population of Vicodin abusers. While the conventional notation is to use $T$ as the upper limit of integration, I used $S$ to represent the upper limit of integration to avoid confusion with the $T$ compartment:

$$A\left(\vec{x}, \vec{p}\right) = \int_0^S g\left(\vec{x}, t, \vec{p}\right) dt = \int_0^S \dot{A} dt.$$

Following the derivation [20], I wrote the adjoint in terms of the Lagrange multiplier $\lambda = \begin{bmatrix} \lambda_M & \lambda_{C_1} & \lambda_{C_2} & \lambda_A & \lambda_T \end{bmatrix}'$, where prime ($'$) denotes the transpose. I used subscript notation to denote partial derivatives, $I$ to denote the identity matrix, and $0_{n\times n}$ to denote the $n \times n$ 0 matrix. The adjoint is

$$g_x + \lambda' \left( F_x - \dot{F}_{\dot{x}} \right) - \dot{\lambda}' F_{\dot{x}} = 0 \ , \tag{3.7}$$

where

$$g_x = \dot{A}_x = \begin{bmatrix} \dot{A}_M & \dot{A}_{C_1} & \dot{A}_{C_2} & \dot{A}_A & \dot{A}_T \end{bmatrix} = \begin{bmatrix} 0 & 0 & \delta & -\varepsilon & \gamma_1 \end{bmatrix}, \tag{3.8}$$

$$F_x = \begin{bmatrix} \alpha_1 + \alpha_2 & 0 & 0 & 0 & 0 \\ -\alpha_1 & \delta + \beta & 0 & 0 & 0 \\ 0 & -\delta & \delta + \beta & 0 & 0 \\ 0 & 0 & -\delta & \varepsilon & -\gamma_1 \\ 0 & 0 & 0 & -\varepsilon & \gamma_1 + \gamma_2 \end{bmatrix},$$

$$\dot{x} = \begin{bmatrix} \dot{M} & \dot{C}_1 & \dot{C}_2 & \dot{A} & \dot{T} \end{bmatrix}',$$

$$F_{\dot{x}} = I_{5\times 5},$$

and

$$\dot{F}_{\dot{x}} = 0_{5\times 5}.$$

Because $\dot{F}_{\dot{x}} = 0$, the $\lambda' \left( F_x - \dot{F}_{\dot{x}} \right)$ term in (3.7) simplifies to $\lambda' F_x$. Thus,

$$\lambda' F_x = \begin{bmatrix} \varphi & \psi \end{bmatrix}, \tag{3.9}$$

where

$$\varphi = \begin{bmatrix} (\alpha_1 + \alpha_2)\lambda_M - \alpha_1 \lambda_{C_1} & (\delta + \beta)\lambda_{C_1} - \delta \lambda_{C_2} \end{bmatrix}$$

and

$$\psi = \begin{bmatrix} (\delta + \beta)\lambda_{C_2} - \delta \lambda_A & \varepsilon \lambda_A - \varepsilon \lambda_T & \gamma_1 \lambda_A + (\gamma_1 + \gamma_2)\lambda_T \end{bmatrix}.$$

Because $F_{\dot{x}}$ is the identity matrix, the $\dot{\lambda}' F_{\dot{x}}$ term in (3.7) simplifies to

$$\dot{\lambda}' = \begin{bmatrix} \dot{\lambda_M} & \dot{\lambda_{C_1}} & \dot{\lambda_{C_2}} & \dot{\lambda_A} & \dot{\lambda_T} \end{bmatrix}. \tag{3.10}$$

Substituting (3.8) - (3.10) into (3.7), I obtained the adjoint equations:

$$\begin{aligned}
(\alpha_1 + \alpha_2)\,\lambda_M - \alpha_1 \lambda_{C_1} - \dot{\lambda_M} &= 0 \\
(\delta + \beta)\,\lambda_{C_1} - \delta \lambda_{C_2} - \dot{\lambda_{C_1}} &= 0 \\
\delta + (\delta + \beta)\,\lambda_{C_2} - \delta \lambda_A - \dot{\lambda_{C_2}} &= 0 \\
-\varepsilon + \varepsilon \lambda_A - \varepsilon \lambda_T - \dot{\lambda_A} &= 0 \\
\gamma_1 - \gamma_1 \lambda_A + (\gamma_1 + \gamma_2)\,\lambda_T - \dot{\lambda_T} &= 0,
\end{aligned}$$

with initial conditions $\lambda_k(S) = 0$. I simultaneously solved the initial value problem $F = 0$, with initial compartment populations

$$\vec{x}(0) = \begin{bmatrix} M(0) & C_1(0) & C_2(0) & A(0) & T(0) \end{bmatrix}',$$

leading to the general sensitivity equation

$$A_p = \int_0^S (g_p + \lambda' F_p)\, dt + \lambda' F_{\dot{x}}|_{t=0}\, y_{x(0)}^{-1} y_p, \tag{3.11}$$

where

$$g_p = \dot{A}_p = \begin{bmatrix} 0_{1\times 3} & C_2 & 0 & -A & T & 0_{1\times 6} \end{bmatrix}, \tag{3.12}$$

$$F_p = \begin{bmatrix}
-1 & M & M & 0 & 0 & & & \\
0 & -M & 0 & C_1 & C_1 & & 0_{3\times 3} & \\
 & & & C_2 - C_1 & C_2 & & & 0_{5\times 5} \\
 & 0_{3\times 3} & & -C_2 & 0 & A & -T & 0 \\
 & & & 0 & 0 & -A & T & T
\end{bmatrix},$$

$$y_p = \begin{bmatrix} & -M(0) & 0 & 0 & 0 & 0 \\ & 0 & -C_1(0) & 0 & 0 & 0 \\ 0_{5\times 8} & 0 & 0 & -C_2(0) & 0 & 0 \\ & 0 & 0 & 0 & -A(0) & 0 \\ & 0 & 0 & 0 & 0 & T \end{bmatrix},$$

and

$$y_{x(0)}^{-1} = \begin{bmatrix} \frac{1}{1-u_M} & 0 & 0 & 0 & 0 \\ 0 & \frac{1}{1-u_{C_1}} & 0 & 0 & 0 \\ 0 & 0 & \frac{1}{1-u_{C_2}} & 0 & 0 \\ 0 & 0 & 0 & \frac{1}{1-u_A} & 0 \\ 0 & 0 & 0 & 0 & \frac{1}{1-u_T} \end{bmatrix}.$$

$\lambda'$ and $F_{\dot{x}}$ are as previously defined. The $\lambda' F_p$ term in (3.11) is $[X \quad Y]$, where

$$X = \begin{bmatrix} -\lambda_M & (\lambda_M - \lambda_{C_1})\, M & \lambda_M M & (\lambda_{C_1} - \lambda_{C_2})\, C_1 + (\lambda_{C_2} - \lambda_A)\, C_2 & \lambda_{C_1} C_1 + \lambda_{C_2} C_2 \end{bmatrix}$$

and

$$Y = \begin{bmatrix} (\lambda_A - \lambda_T)\, A & (\lambda_T - \lambda_A)\, T & \lambda_T T & 0 & 0 & 0 & 0 & 0 \end{bmatrix}. \tag{3.13}$$

The $F_{\dot{x}}|_{t=0}\, y_{x(0)}^{-1} y_p$ term is

$$\begin{bmatrix} & \frac{-M(0)}{1-u_M} & 0 & 0 & 0 & 0 \\ & 0 & \frac{-C_1(0)}{1-u_{C_1}} & 0 & 0 & 0 \\ 0_{5\times 8} & 0 & 0 & \frac{-C_2(0)}{1-u_{C_2}} & 0 & 0 \\ & 0 & 0 & 0 & \frac{-A(0)}{1-u_A} & 0 \\ & 0 & 0 & 0 & 0 & \frac{-T(0)}{1-u_T} \end{bmatrix}. \tag{3.14}$$

Multiplying this by $\lambda'$ yields the $\lambda'\, F_{\dot{x}}|_{t=0}\, y_{x(0)}^{-1} y_p$ term from (3.11):

$$\lambda'\, F_{\dot{x}}|_{t=0}\, y_{x(0)}^{-1} y_p = \begin{bmatrix} 0_{1\times 8} & -\lambda_M \frac{M(0)}{1-u_M} & -\lambda_{C_1} \frac{C_1(0)}{1-u_{C_1}} & -\lambda_{C_2} \frac{C_2(0)}{1-u_{C_2}} & -\lambda_A \frac{A(0)}{1-u_A} & -\lambda_T \frac{T(0)}{1-u_T} \end{bmatrix}. \tag{3.15}$$

Substituting (3.12) - (3.15) into (3.11), I obtained the sensitivity equations (using subscripts to denote partial derivatives):

$$\begin{aligned}
A_{\Lambda} &= \int_0^S -\lambda_M dt \\
A_{\alpha_1} &= \int_0^S (\lambda_M - \lambda_{C_1}) M dt \\
A_{\alpha_2} &= \int_0^S \lambda_M M dt \\
A_{\delta} &= \int_0^S [(\lambda_{C_1} - \lambda_{C_2}) C_1 + (\lambda_{C_2} - \lambda_A + 1) C_2] dt \\
A_{\beta} &= \int_0^S [\lambda_{C_1} C_1 + \lambda_{C_2} C_2] dt \\
A_{\varepsilon} &= \int_0^S (\lambda_A - \lambda_T - 1) A dt \\
A_{\gamma_1} &= \int_0^S (\lambda_T - \lambda_A + 1) T dt \\
A_{\gamma_2} &= \int_0^S \lambda_T T dt \\
A_{u_M} &= -\lambda_M \frac{M(0)}{1 - u_M} \\
A_{u_{C_1}} &= -\lambda_{C_1} \frac{C_1(0)}{1 - u_{C_1}} \\
A_{u_{C_2}} &= -\lambda_{C_2} \frac{C_2(0)}{1 - u_{C_2}} \\
A_{u_A} &= -\lambda_A \frac{A(0)}{1 - u_A} \\
A_{u_T} &= -\lambda_T \frac{T(0)}{1 - u_T}.
\end{aligned}$$

### *3.3.3 Adjoint Sensitivity Analysis*

To find the sensitivity index of compartment $A$ at equilibrium with respect to each parameter, I took the partial derivative of $A$ with respect to the parameter and then divided this result by the ratio of $A$ to the parameter. The resulting quantity is the percent change in $A$ divided by the percent change in the parameter, or the elasticity of $A$ with respect to the parameter. The parameters I tested were those associated

with prevention ($\delta$ and $\beta$) and treatment ($\gamma_1$ and $\gamma_2$), as well as the rate of seeking treatment ($\varepsilon$). Table 3.2 lists these elasticities.

| Parameter | Elasticity Term |
|---|---|
| $\beta$ | $\frac{-2\beta}{\delta+\beta}$ |
| $\delta$ | $\frac{2\beta}{\delta+\beta}$ |
| $\varepsilon$ | $-1$ |
| $\gamma_1$ | $\frac{\gamma_1}{\gamma_1+\gamma_2}$ |
| $\gamma_2$ | $\frac{-\gamma_1}{\gamma_1+\gamma_2}$ |

**Table 3.2:** Elasticities of $A$ with Respect to Treatment and Prevention Parameters at Equilibrium. Note That the Prevention Parameters $\delta$ and $\beta$ are Equal in Magnitude, While the Treatment Parameters $\gamma_1$ and $\gamma_2$ are Also Equal in Magnitude.

Let $\lambda_K$ represent the Lagrange multiplier for the $K$ compartment, and let $u_K$ represent the initial condition of compartment $K$. Then, solving the adjoint equation, using $S$ as the upper limit of integration to avoid confusion with the $T$ compartment, I have the following sensitivity equations:

$$\begin{aligned}
\frac{\partial A}{\partial \beta} &= \int_0^S \left(\lambda_{C_1} C_1 + \lambda_{C_2} C_2\right) dt \\
\frac{\partial A}{\partial \delta} &= \int_0^S \left[\left(\lambda_{C_1} - \lambda_{C_2}\right) C_1 + \left(\lambda_{C_2} - \lambda_A + 1\right) C_2\right] dt \\
\frac{\partial A}{\partial \varepsilon} &= \int_0^S \left(\lambda_A - \lambda_T - 1\right) A dt \\
\frac{\partial A}{\partial \gamma_1} &= \int_0^S \left(-\lambda_A + \lambda_T + 1\right) T dt \\
\frac{\partial A}{\partial \gamma_2} &= \int_0^S \lambda_T T dt.
\end{aligned}$$

Figure 3.2 shows the normalized sensitivity indices at equilibrium. I changed each displayed parameter by 10% and plotted the corresponding changes in the Vicodin abuser equilibrium population, denoted $A^*$. The prevention parameters $\delta$ and $\beta$ are

equal in magnitude and have the greatest effect on $A^*$. The treatment parameters $\gamma_1$ and $\gamma_2$ are also equal in magnitude and have the least effect on $A^*$. The treatment-seeking parameter $\varepsilon$ has a magnitude between that of the prevention and treatment parameters.

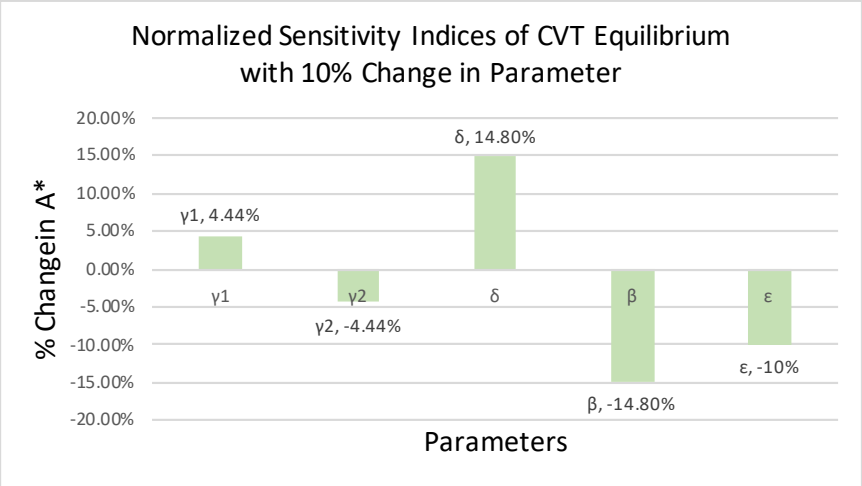


**Figure 3.2:** Sensitivity Indices of Prevention $(\delta, \beta)$, Treatment $(\gamma_1, \gamma_2)$, and Treatment-seeking $(\varepsilon)$ Parameters of the CVT Model at Equilibrium. The Normalized Sensitivity Indices of $\delta$ and $\beta$ are Equal in Magnitude, While Those of $\gamma_1$ and $\gamma_2$ are Also Equal in Magnitude.

Figure 3.3 shows the magnitudes of the sensitivity indices over a period of 250 months ($S = 250$). The sensitivity indices of prevention parameters $\delta$ and $\beta$ converge to one another, and the sensitivity indices of treatment parameters $\gamma_1$ and $\gamma_2$ converge to one another. The prevention parameters have sensitivity indices of the greatest magnitude, while the treatment parameters have sensitivity indices of the least magnitude. The treatment-seeking parameter $\varepsilon$ has a magnitude between those of the prevention and treatment parameters. All of the indices do appear to stabilize around 200 months, converging to their elasticity terms from Table 3.2 divided by the percentage change (10%).

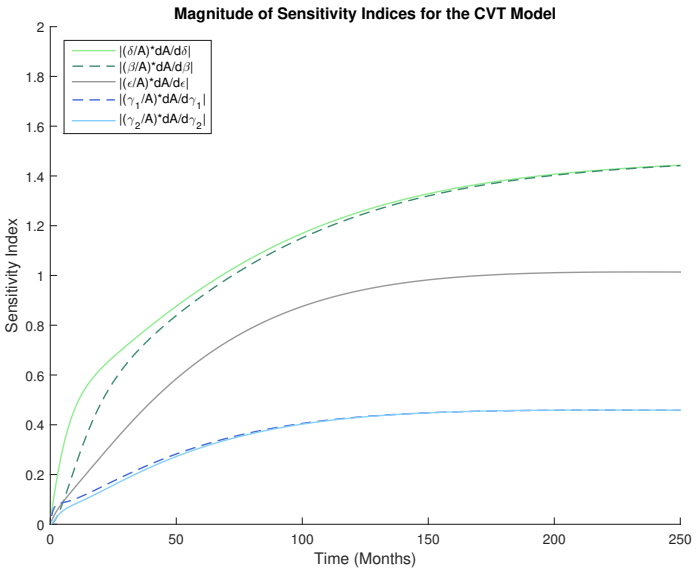


**Figure 3.3:** Sensitivity Indices of Prevention $(\delta, \beta)$, Treatment $(\gamma_1, \gamma_2)$, and Treatment-seeking $(\varepsilon)$ Parameters of the CVT Model over Time. $\delta$ and $\beta$ Converge to One Another, As Do $\gamma_1$ and $\gamma_2$. The Indices Stabilize around 200 Months.

### *3.3.4 Simulation Results*

Using a built-in variable order method in MATLAB (ode15s), I simulated the model over 250 one-month time steps. The simulation initial conditions are in Table 3.3, and the parameter values I used are in Table 3.4.

| Compartment | Initial Population |
|---|---|
| $M$ | 37,600,000 |
| $C_1$ | 5,640,000 |
| $C_2$ | 3,760,000 |
| $A$ | 2,000,000 |
| $T$ | 700,000 |

**Table 3.3:** Initial Populations of Acute Vicodin Users, Chronic Vicodin Users, Vicodin Abusers, and Individuals in Treatment for Vicodin Abuse Used in the CVT Model Simulation. These Values Were Based on Available Data (See Appendix B).

| Parameter | Simulation Value |
|---|---|
| $\Lambda$ | 3,000,000 |
| $\alpha_1$ | 0.220 |
| $\alpha_2$ | 0.45 |
| $\beta$ | 0.140 |
| $\delta$ | 0.050 |
| $\varepsilon$ | 0.030 |
| $\gamma_1$ | 0.240 |
| $\gamma_2$ | 0.293 |

**Table 3.4:** Parameter Values Used in the CVT Model Simulation.

The initial conditions were based on available data (see Appendix B). For the parameter values, I selected values from the ranges in Table 3.1. Figure 3.4 show the simulation plot.

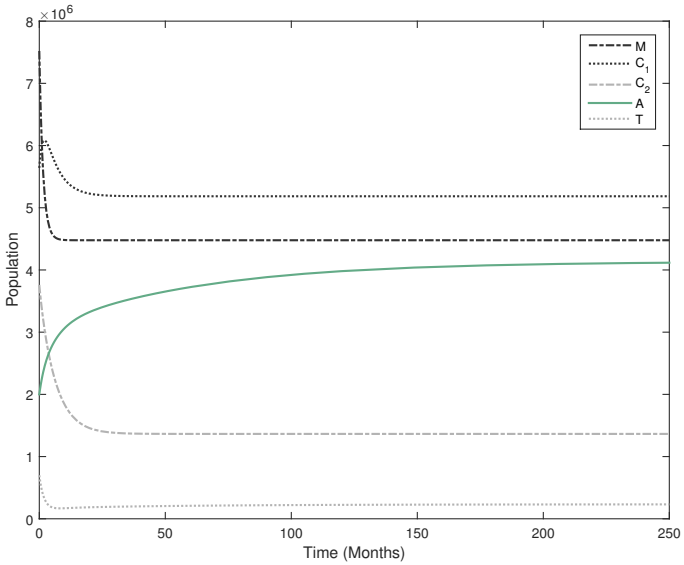


**Figure 3.4:** Simulation of the CVT Model over 250 Months. Most of the Populations Appear to Reach a Steady State by about 24 Months, with the Population of Vicodin Abusers Stabilizing at a Population Approximately Double the Initial Population after about 200 Months.

Based on the simulation, most of the populations reach a steady state by about 24 months (two years). The number of Vicodin abusers in the steady state is higher than the initial number of two million abusers and reaches slightly more than four million abusers after about 200 months (16–17 years). The populations in each of the other compartments decline to their steady states.

## 3.4 Social Interaction with Abuse-Dependent Prescription Rate Model

I modified the CVT model into a nonlinear model, the Social Interaction with Abuse-Dependent Prescription Rate (SIAD) model. I again performed adjoint sensitivity analysis to determine which parameters have the greatest influence on the population of Vicodin abusers. I then ran simulations using data-driven parameter values.

### *3.4.1 Model Description*

The SIAD model differs from the CVT model in two ways. First, I introduced a new parameter, $\rho$, a per capita awareness/intervention parameter with unit 1/people. I scaled the entrance into the model population ($\Lambda$ in the CVT model) by $1 + \rho A$. If $\rho$ is 0, then the entrance is the same as the CVT model. As $\rho$ increases (i.e., prescribers become aware of Vicodin abuse), the number of new acute users each month decreases. Studies of pharmacists and prescribers indicate that when abuse is suspected, or when prescribers are educated on the risks of abuse, the number of prescriptions written and filled decreases [12, 106].

For the second modification, I allowed social interaction between abusers and those in treatment to drive relapse. While the relapse term in the CVT model is $\gamma_1 T$, the relapse term in this model is $\gamma_1 AT$, and the $\gamma_1$ parameter has unit $\frac{1}{\text{people}\times\text{month}}$. This modification is based on research that indicates social interactions contribute

to relapse rates [36]. The SIAD model is described by the system of ordinary differential equations consisting of Equations (3.16)–(3.20). Figure 3.5 depicts a visual representation of the model.

$$\frac{dM}{dt} = \frac{\Lambda}{1+\rho A} - (\alpha_1 + \alpha_2)\, M \tag{3.16}$$

$$\frac{dC_1}{dt} = \alpha_1 M - (\delta + \beta) C_1 \tag{3.17}$$

$$\frac{dC_2}{dt} = \delta C_1 - (\delta + \beta) C_2 \tag{3.18}$$

$$\frac{dA}{dt} = \delta C_2 + \gamma_1 A T - \varepsilon A \tag{3.19}$$

$$\frac{dT}{dt} = \varepsilon A - \gamma_1 A T - \gamma_2 T \tag{3.20}$$

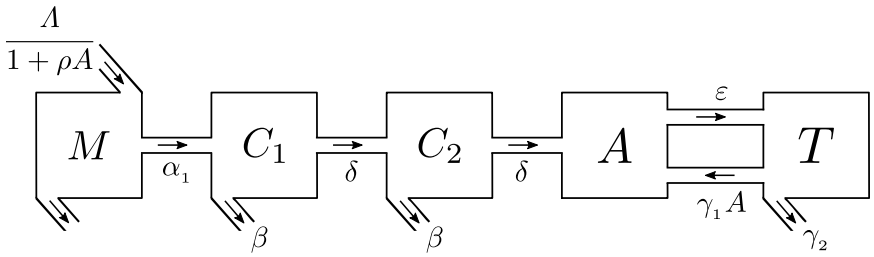


**Figure 3.5:** Diagram Depicting the SIAD Model, a Nonlinear Variation of the CVT Model. The Entrance into the Acute Medical Use Compartment $M$ is No Longer Constant but Scaled by $1 + \rho A$, Where $\rho$ is an Awareness/Intervention Parameter. The Relapse Rate is No Longer Constant but Now Includes Social Interaction between Individuals in Treatment and Individuals Abusing Vicodin.

Table 3.5 shows the parameter value ranges for the new $\rho$ parameter the relapse parameter $\gamma_1$, which differs in units from the CVT model. Appendix B contains the derivations of these ranges.

| Parameter | Definition | Value Range<br>Unit |
|---|---|---|
| $\rho$ | prescriber per capita<br>awareness and intervention rate | $[0, 9.5 \times 10^{-6}]$<br>people$^{-1}$ |
| $\gamma_1$ | monthly social interaction-driven<br>relapse rate | $[7.545 \times 10^{-10}, 9.054 \times 10^{-9}]$<br>people$^{-1}$ month$^{-1}$ |

**Table 3.5:** Ranges for Parameters Differing from the CVT Model. Unlisted Parameters Remain Unchanged from the CVT Model and Are in Table 3.1.

### *3.4.2 Adjoint Sensitivity Analysis*

Using the same notation in the CVT model, I solved the adjoint equation to obtain the following sensitivity equations for our parameters:

$$\begin{aligned}
\frac{\partial A}{\partial \beta} &= \int_0^S \left(\lambda_{C_1} C_1 + \lambda_{C_2} C_2\right) dt \\
\frac{\partial A}{\partial \delta} &= \int_0^S \left[\left(\lambda_{C_1} - \lambda_{C_2}\right) C_1 + \left(\lambda_{C_2} - \lambda_A + 1\right) C_2\right] dt \\
\frac{\partial A}{\partial \varepsilon} &= \int_0^S \left(\lambda_A - \lambda_T - 1\right) A dt \\
\frac{\partial A}{\partial \gamma_1} &= \int_0^S \left(-\lambda_A + \lambda_T + 1\right) AT dt \\
\frac{\partial A}{\partial \gamma_2} &= \int_0^S \lambda_T T dt.
\end{aligned}$$

Sensitivity equations for $\beta, \delta, \varepsilon$, and $\gamma_2$ remain the same for the SIAD model as in the CVT model. The difference comes in the nonlinearity of the relapse term, which appears in the integrand of the sensitivity equation for the relapse parameter $\gamma_1$.

Figure 3.6 shows the magnitudes of the sensitivity indices over a period of 250 months ($S = 250$). The prevention parameters $\delta$ and $\beta$ converge to one another after about 50 months. The treatment parameters $\gamma_1$ and $\gamma_2$ have a negligible effect in this model (see Appendix C). The treatment-seeking parameter $\varepsilon$ has an effect less

than that of the prevention parameters. The indices appear to stabilize around 100 months.

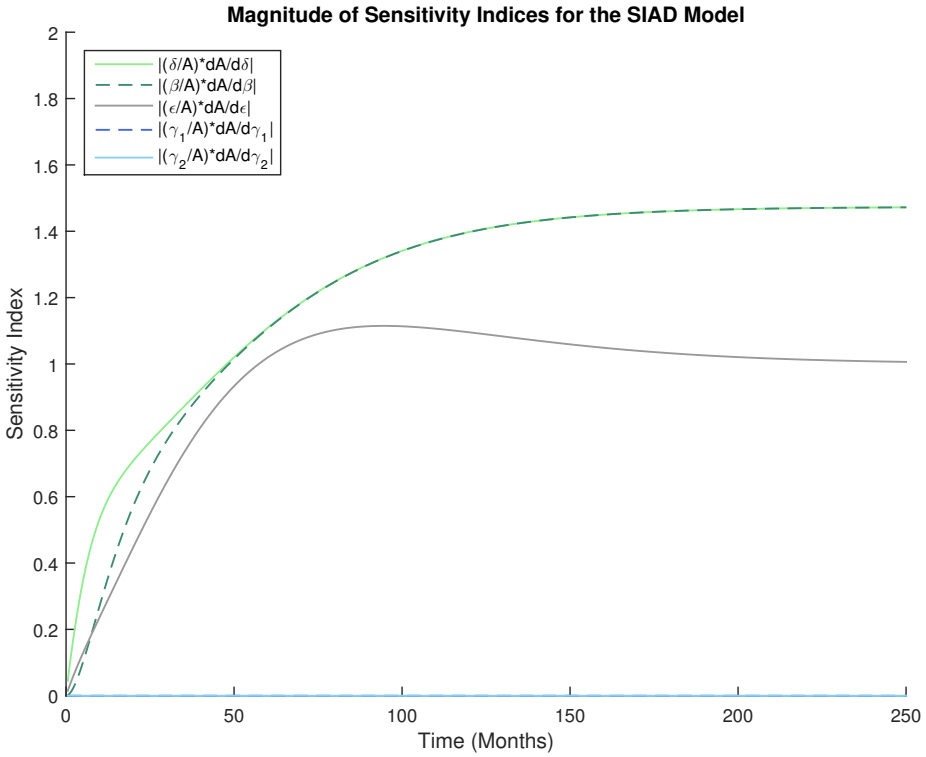


**Figure 3.6:** Sensitivity Indices of Treatment $(\gamma_1, \gamma_2)$, Prevention $(\delta, \beta)$, and Treatment-seeking $(\varepsilon)$ Parameters of the SIAD Model over Time. While the Treatment Parameters are Non-zero, Their Effects Are Negligible Compared to Other Parameters.

### *3.4.3 Simulation Results*

Using the same built-in variable order method in MATLAB, I simulated the model over 250 one-month time steps. Table 3.6 lists parameter values that differ from the CVT model. Other parameter values are identical to those listed in Table 3.4. The new parameter $\rho$ is included in this simulation, and $\gamma_1$ has been scaled to accommodate the change in units in the SIAD model. The initial conditions are the same as in the CVT model (see Table 3.3 and Appendix B).

| Parameter | CVT Simulation Value | SIAD Simulation Value |
|---|---|---|
| $\gamma_1$ | 0.240 | $8 \times 10^{-10}$ |
| $\rho$ | N/A | $1 \times 10^{-6}$ |

**Table 3.6:** Parameter Value Changes and Additions in the SIAD Model Simulations Compared to the CVT Model Simulations.

Figure 3.7 shows the simulation plot. Based on the simulation, the populations in each compartment appear to reach their steady states around the same time, after about 100 months (8–9 years).

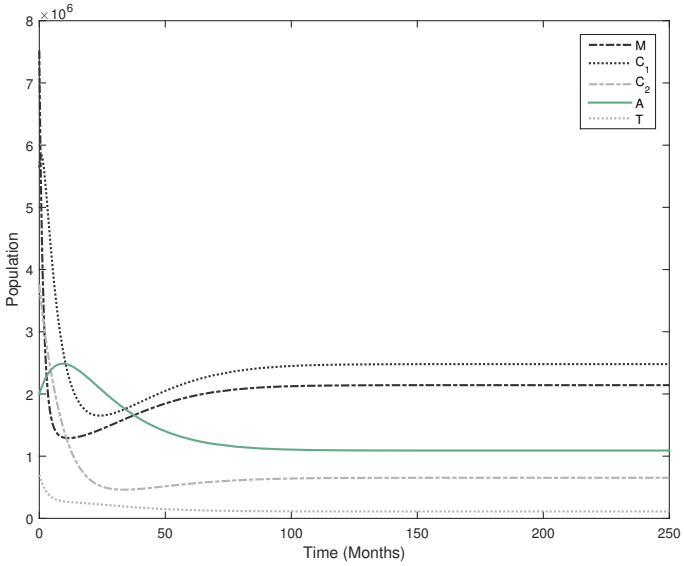


**Figure 3.7:** Simulation of the SIAD Model over 250 Months. The Populations Appear to Reach Their Steady States around 100 Months. The Population of Vicodin Abusers Stabilizes at Slightly More than One Million Vicodin Abusers, a Decrease of Almost 50% of the Original Two Million Abusers.

The population of Vicodin abusers decreases considerably in this model. After an initial spike in the beginning of the simulation, the population then decreases to a steady state of slightly more than one million Vicodin abusers. The simulation reaches a steady state about 50 months (4–5 years) sooner than in the CVT model, which I

attribute to the nonlinear model entrance and relapse terms. The CVT model holds these values as constant, while they vary according to the population of abusers in the SIAD model.

## 3.5 Discussion

The CVT model gave a linear representation of the population of Vicodin users. Beginning with an initial prescription for acute medical use, the model allowed for patients to transition into compartments for chronic use, abuse, and treatment, with the option of leaving the population along the way if Vicodin use ceased. Linear models such as the CVT model provide a basic insight into an epidemiological problem. By modeling the population as an epidemic, I captured the usual progression of Vicodin abuse, beginning with an initial prescription. The possibility of relapse set this model apart from typical $SIR$ models and further illustrated the unique dynamics of the prescription drug problem in the United States.

Finding the sensitivity index of each parameter with respect to the abuse compartment provided insight into addressing the Vicodin abuse problem. By examining how changes in each parameter affect the overall population of Vicodin abusers, I determined that focusing efforts on preventative measures is the most promising method of reducing the number of Vicodin abusers in the United States.

The SIAD model gave a nonlinear representation of the Vicodin abuse population. As in the CVT model, I considered only the typical path of Vicodin abusers: those who were initially prescribed Vicodin. The nonlinearities of this model allowed for a more realistic view of Vicodin abuse dynamics. By introducing an awareness/intervention parameter, the model allowed for the number of new acute users to decrease as awareness of abuse increased. The relapse rate, assumed constant in the CVT model, was driven by social interactions between abusers and those in treatment. As

more interaction occurred, relapse rates increased, whereas decreased social interaction resulted in a decrease in relapses.

In both models, the parameters associated with prevention $(\delta, \beta)$ had the highest sensitivity indices. Further, in both models, the indices of these parameters converged to one another, showing an equal effect on the population of Vicodin abusers, after 200 months for the CVT model and 50 months for the SIAD model. Prior to converging, the $\delta$ parameter showed a slightly higher sensitivity index than the $\beta$ parameter in both models. Thus, I concluded that initially the focus should be on changing the rate at which chronic Vicodin users become abusers, while afterward equal focus can be applied to changing this rate and the rate at which chronic Vicodin users stop Vicodin treatment. The change in DEA scheduling of Vicodin is a possible means of changing these rates, and it is also possible that this change will cause an increase in the value of $\rho$, the awareness/intervention parameter in the SIAD model. However, more data are needed before drawing any such conclusions.

It is worth noting that in the SIAD model, treatment success and relapse rates had no effect on the population of Vicodin abusers. Because social interaction often plays a role in treatment and relapse, I believe that this model is the more accurate of the two because it captures the important dynamics of social interaction.

In both models, $\varepsilon$, the rate at which abusers seek treatment, had a measurable effect. Although this effect is not as strong as that of the prevention parameters, my sensitivity analyses showed that this parameter can affect the population of abusers and thus should not be neglected. I therefore recommend that at least some efforts to combat the Vicodin abuse problem target this rate so that more abusers enter treatment programs.

Although these models focused specifically on Vicodin, they could be adapted to include other prescription drugs. Parameter values could be reassessed to reflect

other prescription drugs that have risks of physical and chemical dependency. These models provide a foundation for modeling substance abuse of pharmaceuticals. Substances for which the most common path to abuse arises from a medical reason could be better understood by modeling in this manner.

### *3.5.1 Future Work*

Both models considered only the population of Vicodin users with an initial prescription. While the majority of Vicodin users begin using with a prescription, the models could be further adapted to include those who were first introduced to Vicodin through other means, such as experimentation.

There are many aspects that affect an individual's likelihood to become an abuser. The demographics with the highest abuse rates include men between the ages of 20 and 64 and those living in poor and rural populations [107]. Introducing an age-structured model could help better represent the populations most at risk of becoming abusers. A spatial component to determine the rurality of an individual (distance from a larger city) could also capture these dynamics.

Monte Carlo simulations could be used to span the parameter space to better understand the effects of parameter values on each compartment, as could global sensitivity analysis. I could further adapt these models to allow parameter values to change over time rather than remain constant, which I anticipate may be a more realistic interpretation of the parameter values.

As more robust data sets become available, we plan to re-examine parameter values and adjust them as needed. If new data sets suggest that another means of exiting the abuse compartment is necessary, we can modify the model to include death from overdose and the cessation of Vicodin abuse caused by the abuse of another substance (a gateway drug effect).

Finally, a cost-benefit analysis could be useful, especially when informing policy change. These models indicate that prevention parameters have the greatest effect on the population of Vicodin abusers. However, I have not determined the cost of affecting these parameters. Given a fixed budget, the sensitivity analysis could be used to determine which combination of parameters would have the greatest effect on reducing Vicodin abusers while maintaining certain fiscal constraints.

# Chapter 4

# ANALYSIS OF VICODIN ABUSE MODELS

Chapter 3 introduced two deterministic mathematical models for Vicodin abuse in the United States. In that chapter, I relied on computational methods to solve the systems of ordinary differential equations. In the current chapter, I focus on the mathematical analysis of the nonlinear SIAD model, with a summary of the results from the linear CVT model. Section 4.1 summarizes these results.

For $SIR$-type models that describe populations, solutions must be non-negative for all model time in order to be considered biologically relevant (i.e., no compartment has a negative population). Likewise, solutions must be bounded above for all model time (i.e., no compartment has a population that grows to $\infty$). Section 4.2.2 contains proofs that solutions to each model equation are non-negative for all positive time if initial conditions and parameter values are positive. Section 4.2.3 contains proofs that solutions to each model equation are bounded for all positive time if initial conditions and parameter values are positive.

Relying on computational methods for solutions can pose an issue if a particular method always converges to a certain solution. For example, computing the square root of 4 with a calculator will always produce a result of 2, yet another solution (-2) exists. For this reason, it is important to know whether or not a particular problem has a unique solution, and, for more complicated problems, whether or not a solution exists. Section 4.2.1 contains proofs that the model has a unique solution.

## 4.1 Summary of Compartmental Vicodin Transition Model Results

The Compartmental Vicodin Transition (CVT) model [29] consists of five compartments representing various stages in the path from acute medical use ($M$), chronic medical use ($C_1, C_2$), abuse ($A$), and treatment ($T$) (with possible relapse); this path is the most common for people abusing Vicodin [97]. The model equations are

$$\dot{M} = \Lambda - (\alpha_1 + \alpha_2)\, M \tag{3.2}$$

$$\dot{C_1} = \alpha_1 M - (\delta + \beta) C_1 \tag{3.3}$$

$$\dot{C_2} = \delta C_1 - (\delta + \beta) C_2 \tag{3.4}$$

$$\dot{A} = \delta C_2 + \gamma_1 T - \varepsilon A \tag{3.5}$$

$$\dot{T} = \varepsilon A - (\gamma_1 + \gamma_2)\, T. \tag{3.6}$$

Parameter definitions are in Table 3.1 in Chapter 3.

Simulations of the CVT model showed the population of Vicodin abusers had approximately doubled after about 200 months, at which point the population appears to reach a steady state. The other compartments in the model appear to reach their steady states after approximately 24 months.

Adjoint sensitivity analysis showed that $\delta$ and $\beta$, the parameters associated with prevention, had the greatest (in magnitude) sensitivity indices with respect to changes in the population of $A^*$. $\gamma_1$ and $\gamma_2$, the parameters associated with treatment, had the lowest (in magnitude) sensitivity indices, and $\varepsilon$, the treatment-seeking parameter, had a sensitivity index greater (in magnitude) than the treatment parameters but lower (in magnitude) than the prevention parameters. The sensitivity results indicate that prevention is the most effective means of reducing the number of Vicodin abusers.

## 4.2 Social Interaction with Abuse-Dependent Prescription Rate Model

I consider the Social Interaction with Abuse-Dependent Prescription Rate (SIAD) model, a nonlinear Vicodin abuse model with relapse [29], with positive initial conditions and positive parameter values:

$$\dot{M} = \frac{\Lambda}{1+\rho A} - (\alpha_1 + \alpha_2)\, M \tag{3.16}$$

$$\dot{C_1} = \alpha_1 M - (\delta + \beta) C_1 \tag{3.17}$$

$$\dot{C_2} = \delta C_1 - (\delta + \beta) C_2 \tag{3.18}$$

$$\dot{A} = \delta C_2 + \gamma_1 A T - \varepsilon A \tag{3.19}$$

$$\dot{T} = \varepsilon A - \gamma_1 A T - \gamma_2 T \tag{3.20}$$

### *4.2.1 Local Existence and Uniqueness of Solutions*

**Theorem 4.2.1.** *Local solutions to the SIAD model with initial data in the region* $\Omega := \{(M, C_1, C_2, A, T) : M > 0, C_1 > 0, C_2 > 0, A > 0, T > 0\} \subset \mathbb{R}^5$ *exist and are unique.*

*Proof.* The proof requires applying the Fundamental Existence-Uniqueness Theorem for nonlinear systems from [109], analogous to the Picard-Lindelöf Theorem [79]. To apply the theorem, it is sufficient to show the right-hand side of each model equation is $C^1$ in $\Omega$, which implies local Lipschitz continuity [109]. Note that the only potential discontinuity in the model equations and their derivatives occurs in Equation (3.16) if $A = -\frac{1}{\rho}$. However, this value does not lie in $\Omega$ and can thus be excluded. Then the right-hand side of each model equation is continuously differentiable. Applying the Fundamental Existence and Uniqueness Theorem to the SIAD model, there exists an

interval $[-a, a]$ with $a > 0$ on which the SIAD model has a unique solution, as desired [109]. □

### *4.2.2 Non-negativity of Solutions*

To show that solutions to the SIAD model with non-negative initial data and parameter values remain non-negative for all positive time, consider Proposition A.1 defined in [137]. This proposition guarantees non-negativity of solutions on the interval of existence to systems of differential equations with non-negative initial data given that solutions exist and are unique (see Theorem 4.2.1) for all $t \geq 0$ and provided that each differential equation in the system is non-negative when the differential equation variable is set to 0 and all other variables are assumed non-negative [137].

**Theorem 4.2.2.** *Given non-negative initial conditions and parameter values, solutions to the SIAD model are non-negative on the interval of existence.*

*Proof.* To verify the $\dot{M}$ equation satisfies the conditions of Proposition A.1 in [137], let $M = 0$, and assume $A \geq 0$. Then

$$\begin{aligned} \dot{M} &= \frac{\Lambda}{1 + \rho \underbrace{A}_{\geq 0}} - (\alpha_1 + \alpha_2) \underbrace{M}_{=0} \\ &= \frac{\Lambda}{1 + \rho A} \geq 0. \end{aligned} \tag{4.1}$$

To verify the $\dot{C}_1$ equation satisifes the conditions of Proposition A.1 in [137], let $C_1 = 0$, and assume $M \geq 0$. Then

$$\begin{aligned} \dot{C}_1 &= \alpha_1 \underbrace{M}_{\geq 0} - (\delta + \beta) \underbrace{C_1}_{=0} \\ &= \alpha_1 M \geq 0. \end{aligned} \tag{4.2}$$

To verify the $\dot{C}_2$ equation satisfies the conditions of Proposition A.1 in [137], let $C_2 = 0$, and assume $C_1 \geq 0$. Then

$$\begin{aligned}\dot{C}_2 &= \delta \underbrace{C_1}_{\geq 0} - (\delta + \beta) \underbrace{C_2}_{=0} \\ &= \delta C_1 \geq 0. \end{aligned} \tag{4.3}$$

To verify the $\dot{A}$ equation satisfies the conditions of Proposition A.1 in [137], let $A = 0$, and assume $C_2, T \geq 0$. Then

$$\begin{aligned}\dot{A} &= \delta \underbrace{C_2}_{\geq 0} + \gamma_1 \underbrace{A}_{=0} T - \varepsilon \underbrace{A}_{=0} \\ &= \delta C_2 \geq 0. \end{aligned} \tag{4.4}$$

To verify the $\dot{T}$ equation satisfies the conditions of Proposition A.1 in [137], let $T = 0$, and assume $A \geq 0$. Then

$$\begin{aligned}\dot{T} &= \varepsilon \underbrace{A}_{\geq 0} - \gamma_1 A \underbrace{T}_{=0} - \gamma_2 \underbrace{T}_{=0} \\ &= \varepsilon A \geq 0. \end{aligned} \tag{4.5}$$

Combining (4.1–4.5), Proposition A.1 in [137] applies to the SIAD model, and solutions are non-negative on the interval of existence, as desired. □

### *4.2.3 Solutions to the SIAD Model Are Bounded Above by a Constant on Any Finite Interval* $[0, S]$

Recall from Theorem 4.2.2 that solutions to the SIAD model are non-negative on the interval of existence given non-negative initial conditions and parameter values. We wish to show that solutions to the SIAD model are bounded above by a constant on the interval $[0, S]$ for any finite $S > 0$.

**Lemma 4.2.3.** *$M$ is bounded above by a constant on any finite interval $[0, S]$.*

*Proof.* Using the model equation for $\dot{M}$:

$$\begin{aligned}\dot{M} &= \frac{\Lambda}{1+\rho A} - (\alpha_1 + \alpha_2)\, M \\ &\leq \frac{\Lambda}{1+\rho A} \text{ because } M \geq 0 \\ &\leq \Lambda \text{ because } A \geq 0\ .\end{aligned}$$

Thus, $\dot{M} \leq \Lambda$. Integrating both sides from with respect to $t$:

$$\begin{aligned}\int_0^S \dot{M} dt &\leq \int_0^S \Lambda dt \\ M\,(S) - M(0) &\leq \Lambda S \\ M(S) &\leq M(0) + \Lambda S.\end{aligned}$$

Define $K_M := M(0) + \Lambda S$. Then, for $t \in [0, S]$, $M \leq K_M$, as desired. □

**Lemma 4.2.4.** *$C_1$ is bounded above by a constant on any finite interval $[0, S]$.*

*Proof.* Using the model equation for $\dot{C}_1$:

$$\begin{aligned}\dot{C}_1 &= \alpha_1 M - (\delta + \beta) C_1 \\ &\leq \alpha_1 M \text{ because } C_1 \geq 0 \\ &\leq \alpha_1 K_M \text{ because } M \leq K_M\ .\end{aligned}$$

Thus, $\dot{C}_1 \leq \alpha_1 K_M$. Integrating both sides with respect to $t$:

$$\begin{aligned}\int_0^S \dot{C}_1 dt &\leq \int_0^S \alpha_1 K_M dt \\ C_1\,(S) - C_1(0) &\leq \alpha_1 K_M S \\ C_1(S) &\leq C_1(0) + \alpha_1 K_M S\ .\end{aligned}$$

Define $K_{C_1} := C_1(0) + \alpha_1 K_M S$. Then, for $t \in [0, S]$, $C_1 \leq K_{C_1}$, as desired. □

**Lemma 4.2.5.** *$C_2$ is bounded above by a constant on any finite interval $[0, S]$.*

*Proof.* Using the model equation for $\dot{C}_1$:

$$\begin{aligned}\dot{C}_2 &= \delta C_1 - (\delta + \beta)C_2 \\ &\leq \delta C_1 \text{ because } C_2 \geq 0 \\ &\leq \delta K_{C_1} \text{ because } C_1 \leq K_{C_1} \ . \end{aligned} \tag{4.6}$$

Thus, $\dot{C}_1 \leq \delta K_{C_1}$. Integrating both sides with respect to $t$:

$$\begin{aligned}\int_0^S \dot{C}_2 dt &\leq \int_0^S \delta K_{C_1} dt \\ C_2(S) - C_2(0) &\leq \delta K_{C_1} S \\ C_2(S) &\leq C_2(0) + \delta K_{C_1} S \ . \end{aligned}$$

Define $K_{C_2} := C_2(0) + \delta K_{C_1} S$. Then, for $t \in [0, S], C_2 \leq K_{C_2}$, as desired. □

**Lemma 4.2.6.** *$A$ and $T$ are bounded above by constants on any finite interval $[0, S]$.*

*Proof.* Define $Z := A + T$, and note that $\dot{Z} = \dot{A} + \dot{T}$. Because $A$ and $T$ are non-negative, it is sufficient to show that $Z$ is bounded above by a constant. Using the model equations for $\dot{A}$ and $\dot{T}$:

$$\begin{aligned}\dot{Z} &= \delta C_2 - \gamma_2 T \\ &\leq \delta C_2 \text{ because } T \geq 0 \\ &\leq \delta K_{C_2} \text{ because } C_2 \leq K_{C_2} \ . \end{aligned}$$

Thus, $\dot{Z} \leq \delta K_{C_2}$. Integrating both sides with respect to $t$:

$$\begin{aligned}\int_0^S \dot{Z} dt &\leq \int_0^S \delta K_{C_2} \\ Z(S) - Z(0) &\leq \delta K_{C_2} S \\ Z(S) &\leq Z(0) + \delta K_{C_2} S \ . \end{aligned}$$

Define $K_Z := Z(0) + \delta K_{C_2} S$. Then, for $t \in [0, S], Z \leq K_Z$, as desired. Further, because $Z = A + T$ and $A, T \geq 0$, $A, T \leq K_Z$. □

**Theorem 4.2.7.** *Solutions to the SIAD model are bounded above on any finite interval* $[0, S]$.

*Proof.* The theorem follows from combining Lemmas (4.2.3–4.2.6). □

From Theorem 2 in Section 2.4 of Perko [109], because the condition in Theorem 4.2.7 holds for any positive $S$, solutions are defined for all $t \geq 0$.

### *4.2.4 Steady State Analysis*

**Theorem 4.2.8.** *The positive steady state of the SIAD model is locally asymptotically stable provided the eigenvalues of the associated Jacobian matrix are real.*

*Proof.* I first find the positive steady state $E^* = (M^*, C_1^*, C_2^*, A^*, T^*)$ by setting each model equation equal to 0.

$$\begin{aligned} \dot{M} &= \frac{\Lambda}{1 + \rho A^*} - (\alpha_1 + \alpha_2) M^* = 0 \\ &\implies M^* = \frac{\Lambda}{(1 + \rho A^*)(\alpha_1 + \alpha_2)}, \end{aligned} \tag{4.7}$$

which is positive because $\rho, \alpha_1, \alpha_2 > 0$ and $A \geq 0$.

$$\begin{aligned} \dot{C}_1 &= \alpha_1 M^* - (\delta + \beta) C_1^* = 0 \\ &\implies C_1^* = \frac{\alpha_1 M^*}{\delta + \beta}, \end{aligned} \tag{4.8}$$

which is positive because $M^*, \alpha_1, \delta, \beta > 0$. Substituting the definition of $M^*$:

$$C_1^* = \frac{\alpha_1 \Lambda}{(1 + \rho A^*)(\alpha_1 + \alpha_2)(\delta + \beta)}. \tag{4.9}$$

$$\begin{aligned} \dot{C}_2 &= \delta C_1^* - (\delta + \beta) C_2^* = 0 \\ &\implies C_2^* = \frac{\delta C_1^*}{\delta + \beta}, \end{aligned} \tag{4.10}$$

which is positive because $C_1^*, \delta, \beta > 0$. Substituting the definition of $C_1^*$:

$$C_2^* = \frac{\alpha_1 \delta \Lambda}{(1 + \rho A^*)(\alpha_1 + \alpha_2)(\delta + \beta)^2}. \tag{4.11}$$

$$\begin{aligned} \dot{A} &= \delta C_1^* + \gamma_1 A^* T^* - \varepsilon A^* = 0 \\ \implies A^* &= \frac{\delta C_2^*}{\varepsilon - \gamma_1 T^*}, \end{aligned} \tag{4.12}$$

which is positive provided

$$\varepsilon - \gamma_1 T^* > 0. \tag{4.13}$$

$$\begin{aligned} \dot{T} &= \varepsilon A^* - \gamma_1 A^* T^* - \gamma_2 T^* \\ \implies T^* &= \frac{\varepsilon A^*}{\gamma_1 A^* + \gamma_2}, \end{aligned} \tag{4.14}$$

which is positive provided $A^*$ is positive. Substituting the definitions of $C_2^*$ and $T^*$ into $A^*$:

$$\begin{aligned} A^* &= \frac{\delta C_2^*}{\varepsilon - \gamma_1 T^*} \\ A^* &= \frac{\frac{\alpha_1 \delta^2 \Lambda}{(1+\rho A^*)(\alpha_1+\alpha_2)(\delta+\beta)^2}}{\varepsilon - \frac{\gamma_1 \varepsilon A^*}{\gamma_1 A^* + \gamma_2}} \\ A^* &= \frac{\frac{\alpha_1 \delta^2 \Lambda}{(1+\rho A^*)(\alpha_1+\alpha_2)(\delta+\beta)^2}}{\frac{\varepsilon \gamma_2}{\gamma_1 A^* + \gamma_2}} \\ A^* &= \frac{\alpha_1 \delta^2 \Lambda (\gamma_1 A^* + \gamma_2)}{\varepsilon \gamma_2 (1 + \rho A^*)(\alpha_1 + \alpha_2)(\delta + \beta)^2} \end{aligned}$$

$$A^* \varepsilon \gamma_2 (1 + \rho A^*)(\alpha_1 + \alpha_2)(\delta + \beta)^2 = \alpha_1 \delta^2 \Lambda (\gamma_1 A^* + \gamma_2)$$

$$\rho\varepsilon\gamma_2\left(\alpha_1+\alpha_2\right)\left(\delta+\beta\right)^2A^{*2}+\left[\varepsilon\gamma_2\left(\alpha_1+\alpha_2\right)\left(\delta+\beta\right)^2-\gamma_1\alpha_2\delta^2\Lambda\right]A^*-\alpha_1\delta^2\gamma_2\Lambda=0. \tag{4.15}$$

The coefficient of $A^{*2}$ is positive, and the constant term is negative. Regardless of whether the coefficient of $A^*$ is positive or negative, there is exactly one sign change. By Descartes' Rule of Signs, there is one positive real root. Substituting $-A^*$ for $A^*$, the only sign change occurs in the coefficient of $A^*$. In this case, there is exactly one sign change and thus one negative real root by Descartes' Rule of Signs. Because each value in $E^*$ can be expressed in terms of $A^*$, and because there is only one biologically relevant value for $A^*$, the positive steady state is unique. Substituting the positive solution of Equation (4.15) into each component of $E^*$ results in the steady state expressed solely in parameter values (see Appendix D).

To determine the stability of $E^*$, I examine the eigenvalues of the Jacobian matrix of the system at $E^*$. The Jacobian matrix at $E^*$ is

$$\begin{bmatrix} -\left(\alpha_1+\alpha_2\right) & 0 & 0 & -\frac{\Lambda\rho}{\left(1+\rho A^*\right)^2} & 0 \\ \alpha_1 & -\left(\delta+\beta\right) & 0 & 0 & 0 \\ 0 & \delta & -\left(\delta+\beta\right) & 0 & 0 \\ 0 & 0 & \delta & -\left(\varepsilon-\gamma_1T^*\right) & \gamma_1A^* \\ 0 & 0 & 0 & \varepsilon-\gamma_1T^* & -\left(\gamma_1A^*+\gamma_2\right) \end{bmatrix}.$$

I find the eigenvalues by setting the following equal to 0:

$$\begin{vmatrix} -\left(\alpha_1+\alpha_2+\lambda\right) & 0 & 0 & -\frac{\Lambda\rho}{\left(1+\rho A^*\right)^2} & 0 \\ \alpha_1 & -\left(\delta+\beta+\lambda\right) & 0 & 0 & 0 \\ 0 & \delta & -\left(\delta+\beta+\lambda\right) & 0 & 0 \\ 0 & 0 & \delta & -\left(\varepsilon-\gamma_1T^*+\lambda\right) & \gamma_1A^* \\ 0 & 0 & 0 & \varepsilon-\gamma_1T^* & -\left(\gamma_1A^*+\gamma_2+\lambda\right) \end{vmatrix}.$$

Following the procedure for finding the determinant of a $5\times5$ matrix, find the char-

acteristic polynomial $P(\lambda) = \varphi\psi - \zeta\eta = 0$, where

$$\begin{aligned}
\varphi &= -(\alpha_1 + \alpha_2 + \lambda)\,[-(\delta + \beta + \lambda)][-(\delta + \beta + \lambda)] \\
\psi &= (\varepsilon - \gamma_1 T^* + \lambda)\,(\gamma_1 A^* + \gamma_2 + \lambda) - (\varepsilon - \gamma_1 T^*)\,\gamma_1 A^* \\
\zeta &= \alpha_1 \delta^2 \\
\eta &= \frac{\Lambda\rho}{(1 + \rho A^*)^2}\,(\gamma_1 A^* + \gamma_2 + \lambda)\,.
\end{aligned}$$

Expanding, I have:

$$\begin{aligned}
\varphi &= -\lambda^3 - [\alpha_1 + \alpha_2 + 2(\delta + \beta)]\,\lambda^2 - \left[2\,(\alpha_1 + \alpha_2)\,(\delta + \beta) + (\delta + \beta)^2\right]\lambda \\
&\quad - \left[(\alpha_1 + \alpha_2)\,(\delta + \beta)^2\right] \qquad (4.16) \\
\psi &= \lambda^2 + (\varepsilon - \gamma_1 T^* + \gamma_1 A^* + \gamma_2)\,\lambda + \gamma_2\,(\varepsilon - \gamma_1 T^*) \qquad (4.17) \\
\zeta\eta &= \left[\frac{\alpha_1 \delta^2 \Lambda\rho}{(1 + \rho A^*)^2}\right]\lambda + \frac{\alpha_1 \delta^2 \Lambda\rho\,(\gamma_1 A^* + \gamma_2)}{(1 + \rho A^*)^2}. \qquad (4.18)
\end{aligned}$$

Define

$$\begin{aligned}
\mathbf{A} &:= \alpha_1 + \alpha_2 + 2(\delta + \beta) > 0 \\
\mathbf{B} &:= 2\,(\alpha_1 + \alpha_2)\,(\delta + \beta) + (\delta + \beta)^2 > 0 \\
\mathbf{C} &:= (\alpha_1 + \alpha_2)\,(\delta + \beta)^2 > 0 \\
\mathbf{D} &:= \varepsilon - \gamma_1 T^* + \gamma_1 A^* + \gamma_2 > 0 \text{ because } \varepsilon - \gamma_1 T^* > 0 \\
\mathbf{E} &:= \gamma_2\,(\varepsilon - \gamma_1 T^*) > 0 \text{ because } \varepsilon - \gamma_1 T^* > 0 \\
\mathbf{F} &:= \frac{\alpha_1 \delta^2 \Lambda\rho}{(1 + \rho A^*)^2} > 0 \\
\mathbf{G} &:= \frac{\alpha_1 \delta^2 \Lambda\rho\,(\gamma_1 A^* + \gamma_2)}{(1 + \rho A^*)^2} > 0.
\end{aligned}$$

Then

$$\begin{aligned}
\varphi &= -\left[\lambda^3 + \mathbf{A}\lambda^2 + \mathbf{B}\lambda + \mathbf{C}\right] \\
\psi &= \lambda^2 + \mathbf{D}\lambda + \mathbf{E} \\
\zeta\eta &= \mathbf{F}\lambda + \mathbf{G},
\end{aligned}$$

and the characteristic polynomial becomes

$$\begin{aligned} P(\lambda) &= \varphi\psi - \zeta\eta = 0 \\ &= -\lambda^5 - (\mathbf{A}+\mathbf{D})\lambda^4 - (\mathbf{AD}+\mathbf{B}+\mathbf{E})\lambda^3 - (\mathbf{AE}+\mathbf{BD}+\mathbf{C})\lambda^2 \\ &\quad -(\mathbf{BE}+\mathbf{CD})\lambda - \mathbf{CE} - \mathbf{F}\lambda - \mathbf{G} \\ &= -\lambda^5 - (\mathbf{A}+\mathbf{D})\lambda^4 - (\mathbf{AD}+\mathbf{B}+\mathbf{E})\lambda^3 - (\mathbf{AE}+\mathbf{BD}+\mathbf{C})\lambda^2 \\ &\quad -(\mathbf{BE}+\mathbf{CD}+\mathbf{F})\lambda - (\mathbf{CE}+\mathbf{G}). \end{aligned} \tag{4.19}$$

The Routh-Hurwitz criterion for stability was inconclusive in this case, and in general, fifth-degree polynomials have no formula for solutions [1]. However, Descartes' Rule of Signs can lead to a condition for which $E^*$ is locally asymptotically stable. White and Comiskey also used this method to analyze the stability of the steady state of their heroin epidemic model in [145].

Because the coefficients of $P(\lambda)$ have no sign changes, from Descartes' Rule of Signs, I can conclude there are 0 possible positive real roots. I next examine $P(-\lambda)$ to determine the possible number of negative real roots:

$$\begin{aligned} P(-\lambda) &= \lambda^5 - (\mathbf{A}+\mathbf{D})\lambda^4 + (\mathbf{AD}+\mathbf{B}+\mathbf{E})\lambda^3 - (\mathbf{AE}+\mathbf{BD}+\mathbf{C})\lambda^2 \\ &\quad +(\mathbf{BE}+\mathbf{CD}+\mathbf{F})\lambda - (\mathbf{CE}+\mathbf{G}). \end{aligned} \tag{4.20}$$

From Descartes' Rule of Signs, from the five sign changes, I know I have 5, 3, or 1 negative real root. If all eigenvalues are real numbers, then I must have five negative eigenvalues, and $E^*$ is a stable node, as desired. □

**Conjecture 4.2.9.** *The positive steady state of the SIAD model is asymptotically stable.*

Numerical analysis suggests the steady state is asymptotically stable. However, in the case of complex eigenvalues, the stability of the steady state is indeterminable at present.

### 4.2.5 Basic Reproduction Number

Consider the steady state $E^*$ from Section 4.2.4:

$$E^* = \left( \frac{\Lambda}{(1+\rho A^*)(\alpha_1+\alpha_2)}, \frac{\alpha_1 M^*}{\delta+\beta}, \frac{\delta C_1^*}{\delta+\beta}, \frac{\delta C_2^*}{\varepsilon-\gamma_1 T^*}, \frac{\varepsilon A^*}{\gamma_1 A^*+\gamma_2} \right). \tag{4.21}$$

Note that for an epidemic to be present, $E^*$ must exist and be biologically relevant (i.e., $E^* \geq 0$, with $A^* > 0$). Because all populations and parameters are non-negative, $E^*$ exists and is biologically relevant provided $A^* > 0$. Because populations and parameter values are assumed non-negative, $A^* > 0$ when $\varepsilon - \gamma_1 T^* > 0$:

$$\begin{aligned} \varepsilon - \gamma_1 T^* &> 0 \\ \varepsilon &> \gamma_1 T^* \\ \frac{\varepsilon}{\gamma_1 T^*} &> 1. \end{aligned}$$

Thus, for the SIAD model,

$$\mathfrak{R}_0 = \frac{\varepsilon}{\gamma_1 T^*}.$$

Substituting the definition of $T^*$ into $\mathfrak{R}_0$:

$$\begin{aligned} \mathfrak{R}_0 &= \frac{\varepsilon}{\gamma_1 \left( \frac{\varepsilon A^*}{\gamma_1 A^* + \gamma_2} \right)} \\ &= \frac{\varepsilon\gamma_1 A^* + \varepsilon\gamma_2}{\gamma_1 \varepsilon A^*} \\ &= 1 + \frac{\gamma_2}{\gamma_1 A^*}. \end{aligned}$$

Note that $\mathfrak{R}_0 > 1$, so the positive steady state $E^*$ always exists.

Chapter 5

# INTRODUCTION TO HYDROCODE MODELING

## 5.1 Components of Hydrocodes

Hydrodynamics codes (hydrocodes) are computer codes that model continuous media. Initially developed for fluid flow modeling, hydrocodes have evolved to include additional features that allow hydrocode modeling to address a broader set of problems. Hydrocode simulations are necessary for problems that exceed experimental capabilities because they can handle multi-physics simulations and large components. These computer codes have three primary components: laws of motion; equation of state; and constitutive model [35].

The laws of motion involve equations for the conservation of momentum (5.1), mass (5.2), and energy (5.3) [96].

$$\frac{\rho D\mathbf{u}}{Dt} = -\nabla P \tag{5.1}$$

$$\frac{D\rho}{Dt} + \rho\nabla \cdot \mathbf{u} = 0 \tag{5.2}$$

$$\frac{dE}{dt} + P\frac{dV}{dt} = 0, \tag{5.3}$$

where $\mathbf{u}$ is velocity, $\rho$ is density, $P$ is pressure, $E$ is internal energy (per unit mass), and $V$ is volume [96]. $D$ is the Lagrangian differential $\left(\frac{\partial}{\partial t} + \mathbf{u}\cdot\nabla\right)$, $\nabla$ is the gradient, and $\nabla\cdot$ is the divergence [95].

The equation of state (EOS) is included to relate pressure, density, and internal energy. The EOS accounts for compressibility effects such as shock heating and density changes. The constitutive model expresses the stress tensor as a function of strain, strain rate effects, internal energy, and damage [35].

## 5.2 Discretization Methods

Hydrocodes can be discretized by several methods: finite-difference, finite-element, finite-volume, and Smooth Particle Hydrodynamics (SPH) [35, 46, 96]. In the finite-different method, forward (5.4), backward (5.5), or central (5.6) difference equations replace the spatial derivatives [35]:

$$\frac{\partial f}{\partial x}(x_n) = \frac{f_{n+1} - f_n}{\Delta x} \tag{5.4}$$

$$= \frac{f_n - f_{n-1}}{\Delta x} \tag{5.5}$$

$$= \frac{f_{n+1} - f_{n-1}}{2\Delta x}. \tag{5.6}$$

Thus, the finite-different discretization is pointwise.

In contrast, the finite-element discretization method employed rectilinear or curved elements rather than points to divide the space [35]. Futhermore, unlike the structured finite-difference discretization, the finite-element method does not require a structured grid [35]. Each element has an associated set of nodes, and interpolation methods are used to calculate physical quantities at the nodes [15, 35].

Like finite-element methods, finite-volume methods do not require a structured grid. These methods compute fluxes between cells and are locally conservative. The finite-volume method can be used on triangular meshes in addition to rectilinear grids [46].

Finally, the SPH method divides the problem into sets of points, with each point having known velocity, thermal energy, and mass [35]. Hence, the points are called particles. The particles are not connected and are thus able to move freely [35].

## 5.3 Eulerian, Lagrangian, and ALE Approaches

In addition to different discretization methods, hydrocodes can also solve problems with Eulerian, Lagrangian, or Arbitrary Lagrangian-Eulerian (ALE) approaches

[15, 35, 96]. Eulerian methods track materials through a rigid mesh, allowing for a Lagrangian time step in which the mesh may deform in then implementing a remapping step that returns each point in the computational mesh to its original location [35]. This process can give rise to mixed-material cells that are often averaged over materials, creating the potential for reduced accuracy for quantities in mixed-material cells [35]. Advantages of the Eulerian approach include allowing for arbitrarily large deformations and turbulent flow [15].

Lagrangian codes consist of a mesh that moves and deforms with the material [35]. One advantage of the Lagrangian approach is that it allows for modeling solid material properties such as strain and stress evolution because this approach allows for tracking material history within a given cell [35]. The Lagrangian approach can become problematic when cells undergo intense deformation, leading to cells that can change shape but not volume and mesh tangles [35].

ALE codes remap the solution from the Lagrangian mesh to a fixed Eulerian mesh in a manner defined by the user [15]. The ALE approach combines the benefits of the Eulerian and Lagrangian approaches and thus has many of the same advantages and disadvantages associated with each.

## 5.4 Equations of State

The EOS component of a hydrocode defines a relationship between the physical properties of a material. The simplest form of an EOS is the ideal gas law

$$PV = nRT,$$

where $V$ is the volume, $n$ is the number of moles, $R$ is the ideal gas constant, and $T$ is the temperature [96]. Another common analytic EOS is the Mie-Grüneisen EOS

$$P - P_0 = \frac{\gamma}{V}\left(E - E_0\right),$$

where the subscript 0 denotes the reference state. $\gamma$ is the Grüneisen constant

$$\gamma = -\left(\frac{\partial \ln(\nu)}{\partial \ln(V)}\right), \tag{5.7}$$

where $\nu$ represents the vibration frequency [96].

For metals undergoing shocks, a linear EOS is

$$U_s = C_0 + S_1 U_p, \tag{5.8}$$

where $U_s$ is the shock velocity, $C_0$ is the material sound speed at 0 pressure, $S_1$ is the linear EOS coefficient, and $U_p$ is the particle velocity [96].

Tabular equations of state are derived from experimental data and are a useful tool for hydrocode simulations [83]. Like analytic equations of state, they relate material quantities like pressure, temperature, and energy. The experimental values are often from experiments in which the materials undergo considerable deformation, making them a good EOS choice when an analytic option is unavailable or when the modeled materials experience extreme conditions, such as shock loading and phase transitions [83].

## 5.5 Constitutive Models

Constitutive models describe how stress and strain evolve in a material as it undergoes loading. These models can account for elastic and plastic deformation as well as degradation from damage evolution. Constitutive models often calculate stress as a function of strain, which is particularly useful in velocity-driven hydrocodes because the total strain rate is known [96]. Hooke's Law, which states that stress is proportional to strain, is one of the earliest observations of the stress-strain relationship [96]. Chapter 6 describes in detail the constitutive models used in this work.

## 5.6 Hydrocode Modeling of Impact Craters in FLAG

In the following two chapters, I used the Free Lagrange (FLAG) hydrocode to model impact crater formation. FLAG is a finite-volume ALE code developed by and maintained at Los Alamos National Laboratory. FLAG has been used for a variety of physics applications [5, 50, 121], and this work presents a novel use for this hydrocode.

In Chapter 6, I verify and validate (V&V) FLAG for impact cratering simulations using problems defined and accepted by the planetary science community [110]. For verification, I simulate an 1-km diameter aluminum sphere impacting an aluminum target at impact velocities of 5 km/s and 20 km/s. I describe five constitutive models that I use in the verification problems, and I also use strengthless materials to allow for a direct comparison to previously published literature. I perform a mesh resolution study of the verification problem, and I show both convergence and simulation time to demonstrate the varied computational cost associated with each resolution. For validation, I simulate a 2-mm diameter glass sphere impacting a water target at an impact velocity of 4.64 km/s. I compare my results to experimental data and to previously published literature. This work demonstrates that FLAG can indeed be used for impact cratering simulations. Although a number of hydrocodes have previously been tested for such work, FLAG has the capability to model not only material strength properties but also to evolve damage in cells, a vital component to the late stages of crater formation. Demonstrating that FLAG is an acceptable tool for impact cratering models introduces a novel use of this code and lays a foundation for further impact cratering work in FLAG.

Following the successful V&V of FLAG for impact cratering, I go on to model Asteroid 16 Psyche in Chapter 7. Psyche is the largest M-type (metallic) asteroid in the Main Asteroid Belt [82]. Estimates for Psyche's material properties vary

considerably, and an upcoming NASA mission to Psyche is scheduled for a 2022 launch date [82, 90, 141]. I use FLAG to simulate the 70-km diameter crater on the southern hemisphere of Psyche. I perform 2D scoping simulations using various material compositions (silicon dioxide, nickel, iron, and Monel) and constitutive models (Preston-Tonks-Wallace, Steinberg-Guinan, perfect plasticity) to represent Psyche and the impactor in order to determine the likely composition of Psyche. Using the nickel alloy Monel for both impactor and Psyche, I perform a porosity study by varying the porosity of Psyche from 30% to 80%. These 2D simulations provide insight into the likely material composition of Psyche, and the resulting crater depths from these runs indicate that the impact was likely oblique. Using the results from my 2D simulations, I select materials and porosities for 3D simulations. In the 3D simulations, I vary the angle of impact from 45 degrees to 60 degrees from vertical. My 3D results showed the various stages of impact crater formation, including the latter modification stage, sometimes referred to as crater collapse. By using solid material models in FLAG, my simulations were able to capture how the terrain surrounding the impact crater was affected by the impact.

Chapter 6

# VERIFICATION AND VALIDATION OF THE FLAG HYDROCODE FOR IMPACT CRATERING SIMULATIONS

## 6.1 Introduction

Impacts have had a lasting impression on the solar system since its beginning. Evidence of impacts exists in the numerous craters that cover the solid bodies in the solar system [64]. Closer to home, approximately 50 meteroids with diameters greater than 10 cm enter Earth's atmosphere daily, while those with diameters greater than 2 m enter the atmosphere several times per year [19]. Most of these smaller objects disintegrate in the atmosphere [19]. Objects with diameters larger than 20 m have the potential to cause substantial damage through megaton-scale airbursts. These objects enter the atmosphere about once per century [19]. Objects with the potential to have catastrophic effects occur less frequently: every 1000 years for objects with diameters around 100 m; every 100,000 years for objects with diameters around 1 km; every 100 million years for objects with diameters around 10 km [4, 94]. Artificial impact missions such as Deep Impact and the Lunar Crater Observation Sensing Satellite (LCROSS) have provided insight into the impact cratering process, allowing observations of ejecta, impact plumes, temperature, and crater dimensions [3, 58]. The forthcoming Double Asteroid Redirection Test (DART) mission will test kinetic impactor asteroid deflection by striking Didymos-B with a 500 kg impactor at an impact velocity of about 6 km/s and measuring the resulting change in orbital period [132]. However, missions of this nature are infrequent, and the spatial scale of large impacts prohibits experimentation. As a result, scientists must rely on numerical

methods to study impact cratering.

Impact crater formation can be divided into three stages: contact and compression; excavation; modification. The initial stage involves the impact of the projectile with the surface, resulting in a transfer of energy and momentum. The materials in the target and projectile compress, resulting in shock waves [95]. During excavation, the shock wave expands through the target material, weakening into an elastic wave. Target material may be vaporized, creating a vapor plume affecting any surrounding atmosphere, or projected out of the crater, creating an ejecta blanket [95]. During the modification stage, debris ceases to flow up and out of the crater and instead flows downward toward the center of the crater, known as crater collapse [95]. The ability to accurately model these stages opens the door to investigate many outstanding questions about the universe such as the ages of target surfaces, erosion on target surfaces, relative ages of different geologic features, and duration of crater retention [56, 111]. However, one of the only measures of accuracy I have to compare model results is through comparison to the geometry of the craters left following impacts from solid projectiles, although mineral phases can provide insight into pressure history if samples are available. As seen from the formation process, crater size and geometry depend on many factors, among them the size, velocity, and composition of the impactor, the composition of the target, and local gravity [64]. The impact cratering process includes a strength-gravity transition for many large craters. The circumstances surrounding the impact determine whether crater formation is dominated by gravity or by material strength [104]. Housen and Holsapple define the strength-gravity transition as a function of gravity, impactor radius, and impact velocity, which they also express in terms of crater dimensions, density, mass density, strength, and impact velocity [66]. For craters in the strength regime, solid material properties are essential to understanding how impact craters form. Hence, accurate

numerical simulations of impacts and the resulting craters require codes that are able to capture shock dynamics as well as model how materials react under shock conditions.

The Free Lagrange (FLAG) hydrodynamics code (hydrocode) [24, 25, 26], maintained and developed at Los Alamos National Laboratory, is a multiphysics research code with access to various physics models and a diverse set of numerical methods. Recall that hydrocodes like FLAG use numerical methods to solve the equations for momentum, mass, and energy introduced in Chapter 5:

$$\frac{\rho D\mathbf{u}}{Dt} = -\nabla P \tag{5.1}$$

$$\frac{D\rho}{Dt} + \rho\nabla \ \cdot \ \mathbf{u} = 0 \tag{5.2}$$

$$\frac{dE}{dt} + P\frac{dV}{dt} = 0 \ . \tag{5.3}$$

FLAG relies on a finite volume formulation to compute continuum mechanics solutions (namely through approximating solutions to the Euler equations) using either a staggered-grid or cell-centered hydrodynamics algorithm. FLAG uses a fully unstructured grid, allowing an arbitrary polyhedral mesh, that can accommodate physical processes in 1, 2, and 3 spatial dimensions [61]. Several mesh optimization methods are available such as adaptive mesh refinement (AMR), and advection through arbitrary Langrangian-Eulerian (ALE) techniques [27]. FLAG is a fully parallel code, so the user can indicate the number of processors per dimension or allow FLAG to make this determination [61].

FLAG has an extensive library of tools and models to account for material behavior under various loading conditions allowing it to model gases, viscous materials, and solids. One important feature of FLAG is that it incorporates material equations of state (EOS) in both analytical and tabular forms [61]. The EOS relates pressure, density, and internal energy. A material's EOS accounts for compressibility effects

such as shock heating and density changes and is a critical component for accurately modeling shock wave propagation through materials [35]. FLAG has been previously used to study a variety of shock physics problems such as multiphase effects in shock-driven particle-gas instabilities [18], free-surface spallation and transport [50], and Rayleigh-Taylor instabilities and spallation in simulated plate impact experiments [39, 139]. FLAG has been verified and validated for a number of applications with simulations of the Noh problem [27], the Sedov problem [27], the Sod shock tube [27], and comparison to flyer plate experiments [121]. However, FLAG has not yet been used to model impact craters. In this work, I demonstrate that FLAG can be used for such problems through use of two V&V problems common to the planetary science community. These problems were first presented by Pierazzo et al. to test several hydrocodes used for impact cratering simulations [110]. These V&V problems test both the early stages of impact cratering, dominated by thermodynamic properties rather than material properties, and crater evolution over time, which is affected by the impactor and target materials along with gravity.

Code verification problems demonstrate that an algorithm solves the problem as intended, while code validation problems test its ability to match experimental data. The verification problem that I rely on here models an aluminum sphere impacting an aluminum target at 5 km/s and 20 km/s [110]. These aluminum-aluminum impact problems test a code's capability to capture key processes in the early stages of impact cratering, namely the contact and compression, and initial parts of the excavation stages that are driven by shock wave propagation. How well a code captures shock physics occurring during these early stages of impact cratering can be determined by calculating quantities such as the maximum shock pressure, shock pressure decay, temperature, and internal energy [110]. The verification simulations are run as strengthless to remain consistent with Pierazzo et al., who attribute the choice of

strengthless materials to the early stages of crater formation that are studied with this problem [110]. In addition to replicating the verification problem in the same manner as Pierazzo et al. [110], I also performed the verification using FLAG's capability of modeling material strength, which plays a role in lower-velocity impacts. The validation problem involves a laboratory experiment of a glass sphere impacting a water target, with data points measuring the evolution of the resulting crater radius and depth over time [110]. This validation problem tests a code's ability to model the kinematics of impact cratering, in addition to processes active in the later stages of crater formation such as material flow and ejection [110]. Although water does not display stress and damage in the same way as solid materials, the crater formation process is evident in the water's displacement. Water impacts are necessarily strengthless, and I use a strengthless impactor to remain consistent with Pierazzo et al. [110]. Together, these V&V problems allow for evaluation of both early and late stages of impact cratering, involving thermodynamic properties and material behavior under shock conditions. In addition to the V&V analysis, I conduct a mesh resolution study on FLAG using the aluminum-on-aluminum verification problem. I discuss the mesh resolution in terms of cells per projectile radius (cppr), following the same method used by Pierazzo et al. [110].

As mentioned previously, these V&V problems were first used to test hydrocodes by Pierazzo et al. [110]. In this work, several hydrocodes that have been and continue to be used for impact cratering simulations were tested. Several of the previous codes studied were purely Eulerian formulations. While there are advantages of this method such as handling vorticity and shear without the risk of mesh tangling, it is more difficult to account for material strength, damage, and deformation than in Lagrangian approaches. ALE frameworks, as that used in FLAG, can be quite advantageous for impact cratering simulations because they can accommodate both vorticity and solid

material properties. Of the eight codes tested by Pierazzo et al., half are multidimensional (1D, 2D, and 3D) Eulerian approaches: SOVA [127], ZEUS-MP2 [57], CTH [92], and RAGE [53]. These codes have different features valuable to cratering problems including frameworks that can accommodate multi-material problems, radiation hydrodynamics, and AMR. More similar to FLAG, iSALE [6, 68], ALE3D [123], and AUTODYN [10, 17] are all ALE codes. iSALE, however, is limited to 2D and was developed primarily to model fluid flows at a wide range of speeds. ALE3D is based on a finite element formulation rather than finite volume, and can address problems in 2 and 3 spatial dimensions. AUTODYN is perhaps the most similar in approach to FLAG as it is a coupled finite difference code with 2D and 3D capabilities with Lagrangian, Eulerian, and ALE. AUTODYN additionally has smooth particle hydrodynamics (SPH) techniques, but it is expensive, and the source code is unavailable to users. Finally, SPH [16] was also included by [110] and is a multidimensional (1D, 2D, and 3D) SPH code without an underlying grid. For the verification problem, the hydrocodes tested by Pierazzo et al. [110] had an average peak shock pressure of 40.4 GPa in the 5 km/s vertical impact, with a low of 28.4 GPa (ZEUS-MP) and a high of 48 GPa (SOVA). In the 20 km/s vertical impact, the codes had an average peak shock pressure of 379 GPa, with a low of 335 GPa (ZEUS-MP) and a high of 411 GPa (SOVA) [110]. For the validation problem, the tested hydrocodes mostly had errors less than 15% in early time (less than 3.5 ms), with the exception of SOVA (25%) and ZEUS-MP (50%) [110]. Codes run at resolutions of 5 cppr underestimated the radius by 11% and depth by 14%, while codes run at resolutions of 10 cppr underestimated the radius by 7% and depth by 10% [110].

In this work I add FLAG to the list of hydrocodes that have been verified and validated for impact cratering simulations. FLAG combines many of the desirable features found in other codes commonly used in planetary science. For example,

FLAG is massively parallel, conservative because of its finite volume approach, and is capable of solving problems in 1D, 2D, and 3D. Because of its parallelization, FLAG provides accurate results at reduced computational cost, lending itself to solving large problems like those found in planetary science [61]. Furthermore, FLAG has AMR capabilities, radiation hydrodynamics, allows the user to select the unit set, and can accommodate multi-material cells. Beyond these features, FLAG allows the user to choose from a variety of material models including a diverse set of EOS, both analytical and tabular, and various strength models describing plastic flow, work hardening, and damage in solid materials under shock conditions. Hence, FLAG offers a wide range of methods to capture the important physics at play in impact cratering.

## 6.2 Material Models

Using strengthless materials was important to allow for a direct comparison with previously published results. However, solid aluminum was used as the material for both target and impactor. Material properties associated with solid metals can affect crater formation, and laboratory experiments indicate that as impact velocity increases, material strength plays a decreasing role. At lower impact velocities, the impactor remains rigid and only penetrates the target to a depth up to 1 projectile radius. With sufficiently high impact velocities, the impactor undergoes intense shattering and deformation, rendering the material essentially strengthless [28, 95]. For this reason, I also performed the verification problems using five constitutive models, described in this section. I expect that using constitutive models in the 5 km/s impacts will lead to better results. In the 20 km/s impacts, I expect strengthless materials to be a better match.

Modeling with solid materials presents its own set of challenges that must be addressed. Solid materials are inherently different from fluids and thus have additional

properties to consider. The strength of a solid refers to its ability to resist changing shape [95]. Strain measures deformation, and stress refers to the force over a given area that causes deformation [95]. Constitutive models provide a means of accounting for the mechanical properties of materials by describing the relationship between stress and strain [122].

One of the earliest observations of the relationship between stress and strain comes from Hooke's Law, which states that stress ($\sigma$) is proportional to strain ($\epsilon$): $\sigma = E\epsilon$, where $E$ is the proportionality pressure constant [95]. Considering a stress tensor ($\sigma_{ijk}$) and a stiffness tensor ($C_{ijk}$), this relationship can be expressed as

$$\sigma_{ijk} = C_{ijk} \left| \epsilon_k \right| .$$

However, the relationships between stress and strain are often more complex. Solid metals have both elastic and plastic properties. An ideal elastic material deforms under forces but returns to its original state once the deforming forces are removed, while an ideal plastic material resists strain until a certain threshold limit is reached [95]. Consequently, the material responses of solid metals in hydrocodes is often modeled using both elastic and plastic attributes. The transition between the elastic and plastic regimes occurs at the yield point for the material [7]. Once in the plastic regime, materials can exhibit constant deformation or deformation that incorporates hardening behavior [122]. Constitutive models capture these properties, typically by calculating material flow stress as a function of material properties such as temperature and strain rate. Figure 6.1 shows schematic stress-strain curves for perfectly plastic materials, materials that exhibit linear hardening behavior, ductile materials, and brittle materials.

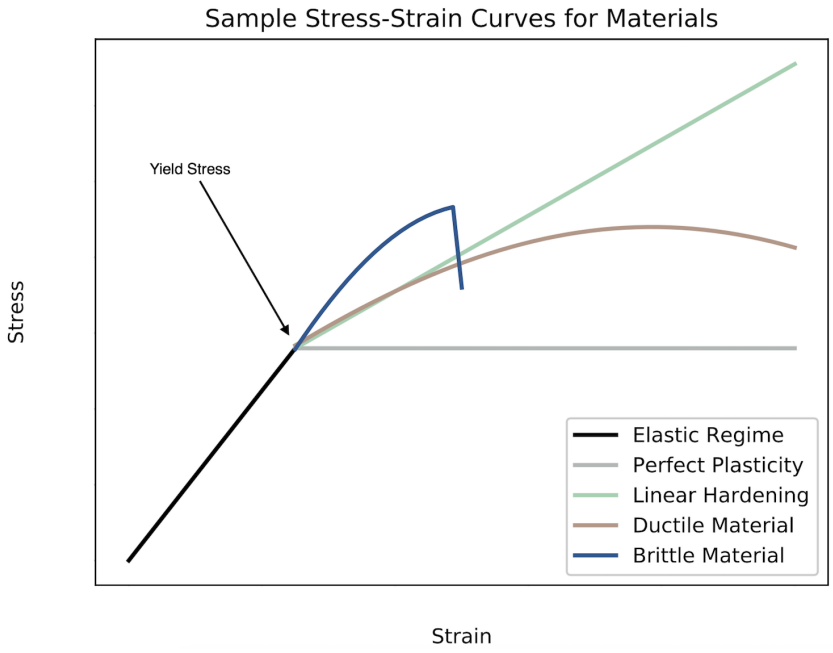


**Figure 6.1:** Sample Stress-strain Curves for Perfectly Plastic Materials, Materials That Harden Linearly, Ductile Materials, and Brittle Materials.

In the verification problem, I use five constitutive models for the aluminum target and the aluminum impactor: perfect plasticity; linear hardening; Johnson-Cook (JC) [71]; Steinberg-Guinan (SG) [130]; Preston-Tonks-Wallace (PTW) [115]. The perfect plasticity (pp), linear hardening (lh), and Johnson-Cook models assume a constant shear modulus, while the Steinberg-Guinan and Preston-Tonks-Wallace models calculate the shear modulus as a function of temperature and pressure. This section describes each of these models. In this chapter, I adopt the following unified notation for all models presented here:

| Notation | Description | Unit | Models |
|---|---|---|---|
| $A$ | quasistatic room temperature flow stress | Pa | JC |
| $B$ | strain hardening effect | Pa | JC |
| $b$ | material exponent | – | PTW |

| | | | |
|---|---|---|---|
| $C$ | strain-rate coefficient | – | JC |
| $G$ | shear modulus | Pa | SG, PTW |
| $G_0$ | reference shear modulus | Pa | SG, PTW |
| $\bar{K}$ | hardening parameter | – | lh |
| $M$ | atomic mass | kg | PTW |
| $m$ | temperature exponent | – | JC |
| $n$ | hardening exponent | – | JC, SG |
| $P$ | pressure | Pa | SG |
| $p$ | Voce hardening law constant | – | PTW |
| $s_0$ | dimensionless saturation stress at 0 K | – | PTW |
| $s_\infty$ | dimensionless saturation stress near melt | – | PTW |
| $T$ | temperature | K | SG, PTW |
| $\hat{T}$ | homologous temperature $\left(\frac{T}{T_m}\right)$ | – | JC, PTW |
| $T_0$ | reference temperature | K | SG |
| $T_m$ | melt temperature | K | PTW |
| $v$ | specific volume | $\frac{\mathrm{m}^3}{kg}$ | SG |
| $v_0$ | reference specific volume | $\frac{\mathrm{m}^3}{kg}$ | SG |
| $Y$ | flow stress | Pa | SG |
| $Y_0$ | reference yield stress | Pa | pp, lh, SG |
| $Y_{\max}$ | upper bound for work hardening | Pa | SG |
| $y_0$ | dimensionless saturation stress at 0 K | – | PTW |
| $y_1$ | material parameter | – | PTW |
| $y_2$ | material parameter | – | PTW |
| $y_\infty$ | dimensionless yield stress near melt | – | PTW |

| | | | |
|---|---|---|---|
| $\alpha$ | temperature parameter | – | PTW |
| $\beta$ | work-hardening coefficient | – | SG |
| $\gamma$ | strain dependence constant | – | PTW |
| $\epsilon$ | equivalent plastic strain | – | lh, JC, SG, PTW |
| $\dot{\epsilon}$ | plastic strain rate | $s^{-1}$ | PTW |
| $\hat{\dot{\epsilon}}$ | dimensionless plastic strain rate | – | JC |
| $\epsilon_i$ | initial $\epsilon$ | – | SG |
| $\eta$ | compression $\left(\frac{v_0}{v}\right)$ | – | SG |
| $\theta$ | initial strain hardening | – | PTW |
| $\kappa$ | material constant | – | PTW |
| $\rho$ | density | $\frac{kg}{m^3}$ | PTW |
| $\sigma$ | von Mises flow stress | Pa | JC |
| $\tau$ | material stress | Pa | pp, lh |
| $\hat{\tau}_s$ | dimensionless work-hardening saturation stress | – | PTW |
| $\hat{\tau}_y$ | dimensionless yield stress | – | PTW |

Table 6.1: Table of Notation Used in Material Models.

### *6.2.1 Perfect Plasticity*

The perfect plasticity model assumes no work hardening, so that the material stress $\tau$ remains constant once it has reached the flow stress $Y_0$ [128]:

$$\tau = Y_0.$$

### 6.2.2 Linear Hardening

In linear hardening, a material exhibits linear work hardening behavior once it meets the yield criterion:

$$\tau = Y_0 + \bar{K}\epsilon,$$

where $\tau$ is the stress, $Y_0$ is the flow stress, $\bar{K}$ is the isotropic hardening modulus, and $\epsilon$ is the equivalent plastic strain [122, 128].

### 6.2.3 Johnson-Cook

The Johnson-Cook model includes effects of both strain hardening and strain-rate hardening as well as thermal softening [71]. To understand the Johnson-Cook model, it is important to understand the role of the von Mises flow stress. Consider the deviatoric stress tensor

$$\begin{bmatrix} \sigma_1 & 0 & 0 \\ 0 & \sigma_2 & 0 \\ 0 & 0 & \sigma_3 \end{bmatrix}.$$

The second principal invariant, denoted $J_2$, is

$$J_2 = \sigma_1\sigma_3 + \sigma_2\sigma_3 + \sigma_1\sigma_2 = \frac{1}{2}\left(\sigma_1^2 + \sigma_2^2 + \sigma_3^2\right).$$

The von Mises yield criterion states that when $J_2$ reaches some critical value, a material undergoes plastic yield. The von Mises effective stress can be calculated in terms of $J_2$ : $\sqrt{3J_2}$ [122]. The Johnson-Cook model calculates the von Mises flow stress $\sigma$ as a function of equivalent plastic strain $\epsilon$, dimensionless plastic strain rate $\hat{\dot{\epsilon}}$, and temperature $T$:

$$\sigma = \left[A + B\epsilon^n\right]\left[1 + C\ln\hat{\dot{\epsilon}}\right]\left[1 - \hat{T}^m\right],$$

where $A$ describes the yield stress (Pa in SI units), $B$ describes the effects of strain hardening (Pa in SI units), $n$ is an exponent that describes the effects of strain

hardening, $C$ is a unitless strain-rate constant, $\hat{T}$ is the homologous temperature $\left(\frac{T}{T_m}\right)$, and $m$ is a unitless temperature exponent [71]. Each factor used in calculating $\sigma$ can be further described as follows [71]:

$$\begin{aligned} A + B\epsilon^n &: \text{ stress as a function of strain, with } \hat{\dot{\epsilon}} = 1, \hat{T} = 0 \\ 1 + C \ln \hat{\dot{\epsilon}} &: \text{ effects of strain rate} \\ 1 - \hat{T}^m &: \text{ effects of temperature.} \end{aligned}$$

### *6.2.4 Steinberg-Guinan*

The Steinberg-Guinan model describes the shear modulus and flow stress for metals at high-strain rates [130]. The model assumes a reference state with temperature $T_0 = 300$ K, pressure $P = 0$, and equivalent plastic strain $\epsilon = 0$. The model calculates the shear modulus $G$ as

$$G = G_0 \left[1 + \left(\frac{G'_P}{G_0}\right) \frac{P}{\eta^{\frac{1}{3}}} + \left(\frac{G'_T}{G_0}\right) (T - 300)\right],$$

where $G_0$ represents the shear modulus at the reference state, $G'_P$ represents the pressure derivative of $G$ at the reference state, $G'_T$ represents the temperature derivative of $G$ at the reference state, and

$$\eta = \frac{v_0}{v}$$

represents the compression, where $v_0$ is the initial specific volume and $v$ is the specific volume [130].

The model calculates the yield stress $Y$ as

$$Y = Y_0 \left[1 + \beta \left(\epsilon + \epsilon_i\right)\right]^n \left[1 + \left(\frac{Y'_p}{Y_0}\right) \frac{P}{\eta^{\frac{1}{3}}} + \left(\frac{G'_T}{G_0}\right) (T - 300)\right],$$

subject to the constraint

$$Y_0 \left[1 + \beta \left(\epsilon + \epsilon_i\right)\right]^n \leq Y_{\max},$$

where $Y_0$ is the yield stress at the reference state, $Y_P'$ is the pressure derivative of $Y$ at the reference state, $\beta$ is the work-hardening coefficient, $n$ is the work-hardening exponent, $\epsilon_i$ is the initial equivalent plastic strain, and $Y_{\max}$ is the saturation value for the hardening term [130].

### *6.2.5 Preston-Tonks-Wallace*

The Preston-Tonks-Wallace (PTW) model describes the flow stress required to plastically deform metals at high strain rates and temperatures close to melt [115]. The model considers the thermal activation regime, in which dislocation movement is driven by energy from thermal vibrations, and the overdriven-shock regime, in which dislocation movement is hindered by drag [115]. The thermal activation regime covers strain rates up to $10^4$, and the overdriven-shock regime covers strain rates in the $[10^9, 10^{12}]$ range. The PTW model describes a link between these two regimes for strain rates not covered by either thermal activation or overdriven-shocks [115]. The model calculates the dimensionless work hardening saturation stress $\dot{\tau}_s$ and yield stress $\dot{\tau}_y$:

$$\begin{aligned}
\dot{\tau}_s &= \max\left\{ s_0 - (s_0 - s_\infty)\operatorname{erf}\left[\kappa\hat{T}\ln\left(\frac{\gamma\dot{\xi}}{\dot{\epsilon}}\right)\right], s_0\left(\frac{\dot{\epsilon}}{\gamma\dot{\xi}}\right)^b\right\}, \\
\dot{\tau}_y &= \max\left\{ y_0 - (y_0 - y_\infty)\operatorname{erf}\left[\kappa\hat{T}\ln\left(\frac{\gamma\dot{\xi}}{\dot{\epsilon}}\right)\right], \min\left[y_1\left(\frac{\dot{\epsilon}}{\gamma\dot{\xi}}\right)^{y_2}, s_0\left(\frac{\dot{\epsilon}}{\gamma\dot{\xi}}\right)^b\right]\right\},
\end{aligned}$$

where $s_0$ and $s_\infty$ represent the respective saturation stresses at 0 temperature and high (near melt) temperature, $y_0$ and $y_\infty$ represent the respective yield stresses at 0 temperature and high (near melt) temperatures, and $y_1, y_2$, and $b$ are dimensionless material parameters [115]. $\kappa\hat{T}\ln\left(\frac{\gamma\dot{\xi}}{\dot{\epsilon}}\right)$ is the dimensionless analog of $k_B T\ln\left(\frac{\dot{\epsilon}_0}{\dot{\epsilon}}\right)$,

where:

$k_B$ : Boltzmann constant,

$\kappa$ : dimensionless material constant,

$T$ : temperature,

$\hat{T}$ : $T$ normalized with respect to melt as a function of density $\left(\frac{T}{T_m(\rho)}\right)$,

$\gamma$ : dimensionless material constant,

$\frac{\dot{\epsilon}}{\dot{\xi}}$ : dimensionless strain rate variable,

$\dot{\epsilon}$ : plastic strain rate as a function of $\dot{\epsilon}_0, k_B$, and activation energy [115].

The strain rate in the thermal activation regime $\dot{\epsilon}$ is defined as

$$\dot{\epsilon} = \dot{\epsilon}_0 \exp\left[-\frac{\Delta\Phi(\tau)}{k_B T}\right],$$

where $\dot{\epsilon}_0$ is proportional to the dislocation vibration frequency and $\Delta\Phi(\tau)$ represents the activation energy as function of the flow stress $\tau$, equal to $\frac{1}{2}$ the von Mises equivalent deviatoric stress $\sigma$ [115]. The model defines $\dot{\xi}^{-1}$ as the time for a transverse wave to cross an atom, and the model calculates $\dot{\xi}$ as follows:

$$\dot{\xi} = \frac{1}{2}\left(\frac{4\pi\rho}{3M}\right)^{\frac{1}{3}}\left[\frac{G(\rho,T)}{\rho}\right],$$

where $M$ is the atomic mass [114].

The dimensionless stress variable in the model is

$$\hat{\tau} = \frac{\tau}{G(\rho,T)},$$

where

$$G(\rho,T) = G_0(\rho)\left(1 - \alpha\hat{T}\right).$$

$G$ represents the shear modulus as a function of temperature $T$ and density $\rho$ [115]. The model calculates $\hat{\tau} =$

$$\hat{\tau}_s + \frac{1}{p}\left(s_0 - \hat{\tau}_y\right) \ln\left\{1 - \left[1 - \exp\left(-p\frac{\hat{\tau}_s - \hat{\tau}_y}{s_0 - \hat{\tau}_y}\right)\right] \exp\left(-\frac{p\theta\epsilon}{\left(s_0 - \hat{\tau}_y\right)\left[\exp\left(p\frac{\hat{\tau}_s - \hat{\tau}_y}{s_0 - \hat{\tau}_y}\right) - 1\right]}\right)\right\},$$

where $p$ is a dimensionless material parameter [115].

In the overdriven-shock regime, the model assumes saturation of work hardening [115]:

$$\hat{\tau}_s = \hat{\tau}_y \propto \left(\frac{\dot{\epsilon}}{\dot{\xi}}\right)^b.$$

## 6.3 Verification

To verify FLAG, I consider an aluminum impactor striking an aluminum target at impact velocities of 5 km/s and 20 km/s. The aluminum impactor is a sphere of diameter 1 km. Because the same material comprises both impactor and target, the particle velocity for the target and impactor are the same, and this value is equal to one-half the impact velocity [96]. I use Al-6061 for both the target and impactor material, and I determine the maximum pressure analytically for such an impact in one dimension to be 58.725 GPa for an impact velocity of 5 km/s and 506.25 GPa for an impact velocity of 20 km/s using Equation (6.1):

$$P = \rho_0 \left(C_0 + SU_p\right) U_p, \tag{6.1}$$

where $P$ is the maximum pressure in GPa, $\rho_0$ is the initial density $\left(2.7\ \mathrm{g/cm^3}\right)$, $C_0$ is the sound velocity at 0 pressure (5.35 mm/$\mu$s), $S$ is the linear EOS coefficient (1.34), and $U_p$ is the particle velocity (1/2 impact velocity)[96].

I use FLAG to simulate these impacts in 1D, 2D, and 3D using Al-6061 (see Appendix F for simulation details). For 1D simulations, I use a Mie-Grüneisen linear EOS for both target and impactor to better match the 1D analytic solution. For 2D

and 3D simulations, I use a SESAME tabular EOS for both impactor and target [83] to stay consistent with the verification simulations in Pierazzo et al. [110]. I choose a resolution of 40 cppr, equivalent to a cell side length of 12.5 m. I use Eulerian (static) tracer particles located 200 m into the target for the 5 km/s impact and 685 m into the target for the 20 km/s impact. For artificial viscosity, I use a Barton model [87] with quadratic coefficient 2 and linear coefficient 0. I use free boundary conditions.

For the 1D simulations in FLAG, I use a projectile of 1 km and a target of 10 km, which allows us to measure peak pressure and shock pressure decay while avoiding boundary effects. For the EOS, I use 2700 kg/m$^3$ for the reference density, 890 J/kg/K for the specific heat, 5350 m/s for the sound speed, 2.0 for $\gamma$, and 1.34 as the linear coefficient [96]. I initialize the aluminum with density 2.7 g/cm$^3$ and an energy of 0 J. I use a pure Lagrangian approach for these simulations. For the 5 km/s impact, I obtain a maximum pressure of 63.68 GPa at the point of impact with a relative error of 8.44% with respect to the analytical solution. For the 20 km/s impact at the tracer particle, I obtain a maximum pressure of 521.93 GPa with a relative error of 3.01%. I attribute these deviations from the analytical solution to the effects of artificial viscosity, not included in Equation (6.1) but required by the hydrocode to spread the shock over multiple time steps to avoid discontinuities. Figure 6.2 shows the pressure wave in the FLAG simulation 0.7 seconds after the 20 km/s impact.

Similarly in 2D, the aluminum projectile is a circle of diameter 1 km, and the

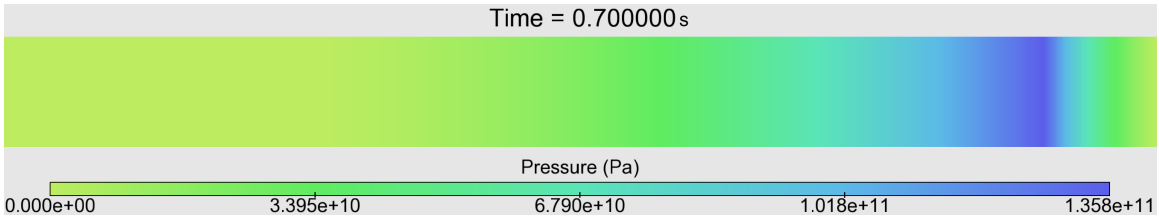


**Figure 6.2:** Pressure Wave for FLAG Simulation of 1D Al-Al 20 km/s Impact 0.7 Seconds after Impact.

aluminum target is a rectangle of length 25 km and width of 10 km. The surrounding material is air with length and width of 25 km and 23.5 km, respectively. The air is treated as a $\gamma$-law gas, with $\gamma = 1.4$. I initialize the air with a density of $1.2922 \times 10^{-3}$ g/cm$^3$ at 273 K. For these simulations, I use FLAG's ALE capabilities to relax the mesh by geometry. Whenever a zone has an angle measure less than or equal to the specified threshold (15 degrees at first and 30 degrees when needed), I relax the mesh at that zone and up to three zones away. Simulated results for the stages of contact and compression, and excavation are shown in Figure 6.3a for the 5-km/s impact. In this case, I obtain maximum pressures at the tracer particle 200 m below impact ranging from 51.02 GPa to 55.77 GPa depending on mesh resolution, with deviations from the 1D analytic solution ranging from -13.12% to -5.15%. In comparison, the mean maximum pressure from the results of the eight codes tested by Pierazzo et al. [110] was 40.4 GPa with a mean deviation from the analytic solution of -33.3%. I also examined the maximum pressure at a tracer particle at the point of impact, with values ranging from 56.29 GPa to 61.16 GPa and deviations from the analytic solution ranging from -4.15% to 4.15%, with a best case of 59.58 GPa and deviation of 1.46%. The cases with the smallest (in magnitude) errors in peak shock pressure at impact and 200 m into the target are listed in Table 6.2. Figure 6.3b shows the pressure wave of the FLAG simulation 0.161265 seconds after the 5-km/s impact.

For the 20-km/s impact, I obtain maximum pressures at tracer particles located 685 m into the target ranging from 388.64 GPa to 407.99 GPa depending on mesh resolution, with deviations from the 1D analytic solution ranging from -23.23% to -19.41%, which can be compared to a mean maximum pressure of 379.0 GPa with mean deviation from the analytic solution of -27.5% obtained by Pierazzo et al. [110]. I also measured the maximum pressure at impact and 200 m into the target, as in the 5 km/s impact, and found the highest pressure value 200 m into the target. At

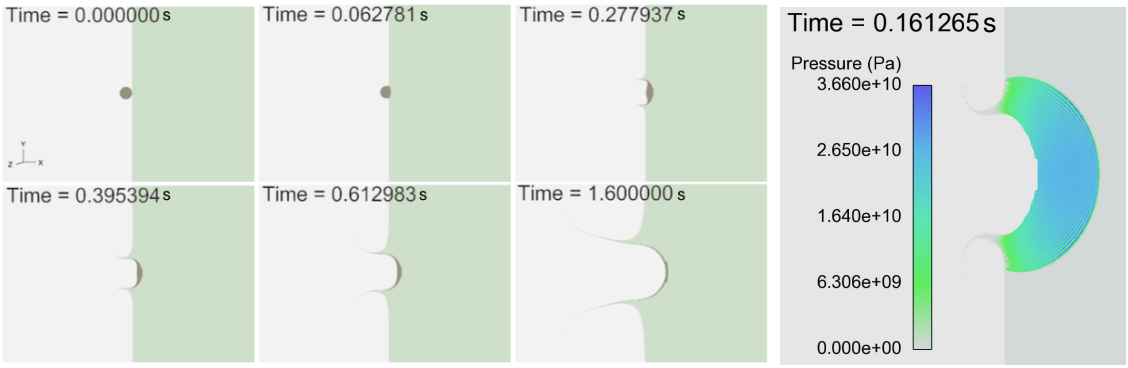


(a) (b)

**Figure 6.3:** (a) Stages of Impact Cratering in 2D FLAG Simulation of an Aluminum Projectile (Brown) Impacting an Aluminum Target (Green) at 5 km/s, Zoomed in to Show Detail. (b) Pressure Wave for FLAG Simulation of 2D Al-Al 5 km/s Impact 0.161265 Seconds after Impact, Zoomed in to Show Detail.

this point, the maximum pressure of FLAG simulations ranged from 466.98 GPa to 494.81 GPa, depending on mesh resolutions, with deviations from the analytic solution ranging from -7.76% to -2.26%. The maximum pressure does not occur at the point of impact because I am measuring pressure with a static tracer particle. The higher impact velocity in this simulation results in the crater forming more quickly, and after the first time step, the static tracer particle no longer contains any target material. In order to more accurately capture the maximum pressure, I used a Lagrangian tracer particle located at the point of impact at time zero, after which the particle moves with the material throughout the simulation. From this tracer particle, I obtain the maximum pressure of 559.44 GPa, with a deviation from the 1D analytic solution of 10.51%, at the tracer particle initialized at the point of impact. The cases with the smallest (in magnitude) errors in peak shock pressure 200 m and 685 m into the target are listed in Table 6.2 to allow for a direct comparison with the results from Pierazzo et al. [110]. To allow for a more direct comparison between the 5 km/s and 20 km/s impact velocities, the maximum pressures from both simulations 200 m into

the target and at the point of also appear in Table 6.2.

For the 3D FLAG simulations, the projectile is an aluminum sphere of diameter 1 km, and the target is an aluminum rectangular prism of length 25 km, width 10 km, and height 10 km. The surrounding material is air with length 25 km, width 23.5 km, and height 10 km. I simulated impact velocities of 5 km/s and 20 km/s and impact angles normal to the target surface and at a 45-degree angle. I ran all 3D simulations using a resolution of 5 cppr, resulting in approximately 8.3 million zones. I used FLAG's ALE capabilities to relax the mesh by geometry. I set the angle threshold to be 30, 45, or 60 degrees, as needed, and relaxed up to five zones away. For the 5 km/s normal impact, the maximum pressure occurred at the point of impact and measured 52.39 GPa with a deviation from the analytic solution of -10.79%. For the 20 km/s normal impact, the maximum pressure occurred 200 m into the target and measured 555.74 GPa with a deviation from the analytic solution of 9.78%. The 45-degree angle impacts do not have an associated analytic solution. Nevertheless, FLAG was able to complete these simulations, producing results consistent with impact craters. For these oblique impacts, the impactor breaks apart, with pieces of the impactor ending up more than 5 km outside the crater. The 5 km/s oblique impact simulation is shown in Figure 6.4. Figure 6.5 shows the pressure wave 0.732070 seconds after impact for the same simulation. These simulations ran on 360 processors. The 5 km/s normal impact took about 5.75 hours for the pressure wave to propagate 10 km into the target, and the 20 km/s normal impact took about 6.5 hours.

One possible explanation for the lower percent deviation from the analytic solution with FLAG is its ALE capability, which reduces advection between cells. FLAG's interface reconstruction prevents numerical diffusion, which may also contribute to the lower errors in 1D and deviations from the 1D analytic maximum pressure in 2D and 3D. FLAG's Lagrange step also conserves internal energy [24, 25]. The advancement

| 2D FLAG Simulation | 1D Analytic Solution | FLAG | Pierazzo et al. Mean[110] |
|---|---|---|---|
| Maximum Pressure, 5 km/s 200 m into target | 58.725 GPa | 55.77 GPa | 40.4 GPa |
| Percent Deviation from 1D Analytic | – | -5.15% | -33.3% |
| Maximum Pressure, 5 km/s point of impact | 58.725 | 59.58 GPa | – |
| Relative Error | – | 1.46% | – |
| Maximum Pressure, 20 km/s 685 m into target | 506.25 | 407.99 GPa | 379.0 GPa |
| Percent Deviation from 1D Analytic | – | -19.41% | -27.5% |
| Maximum Pressure, 20 km/s 200 m into target | 506.25 | 479.10 | – |
| Percent Deviation from 1D Analytic | – | -5.36% | – |
| Maximum Pressure, 20 km/s impact point, Lagrangian tracer | 506.25 | 492.63 GPa | – |
| Percent Deviation from 1D Analytic | – | -2.69% | – |

**Table 6.2:** Maximum Pressure of FLAG Simulation of Aluminum Impacting Aluminum from Eulerian (Static) Tracer Particles Located in the Target. The Results Shown are from the Tracer Particle Locations Used by Pierazzo et al. [110] As Well As the Location of the Maximum Pressure Obtained from 20 Tracer Particles Approximately Evenly Spaced in the Target.

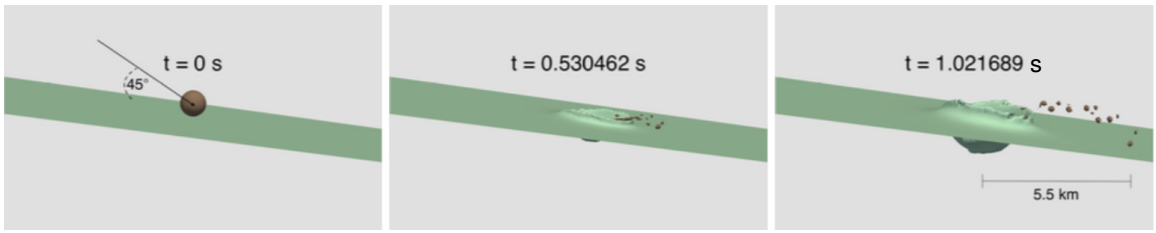


**Figure 6.4:** Visualization of 3D FLAG Simulation of an Aluminum Sphere (Brown) Impacting an Aluminum Target (Green) at 5 km/s at an Impact Angle of 45 Degrees Relative to the Surface of the Target.

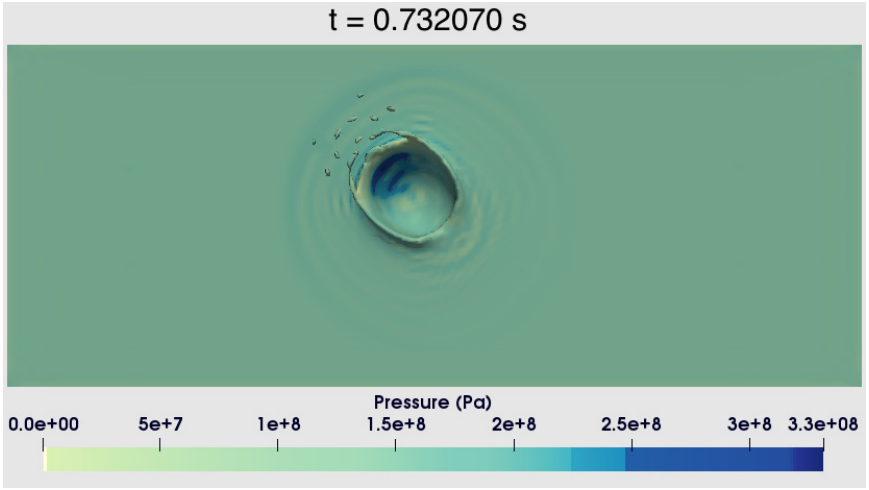


**Figure 6.5:** Pressure Wave for FLAG Simulation of 3D Aluminum-on-Aluminum 5 km/s 45-Degree Impact 0.732070 Seconds after Impact, Shown Looking into the Crater from Above.

of interface reconstruction algorithms since the results from Pierazzo et al. [110] were first reported may help reduce such deviations. In the hydrocodes tested by Pierazzo et al [110], the best result for the maximum pressure was 48 GPa for the 5 km/s impact and 411 GPa for the 20 km/s impact, resulting in respective deviations of -18.26% and -18.82% relative to the 1D analytic solution. Running these simulations in FLAG resulted in respective errors of 8.44% and 3.01% in 1D and deviations from the 1D analytic solution of 1.46% and -2.26% in 2D and -10.79% and 9.78% in 3D. I attribute the higher error in the 1D 5 km/s simulation to artificial viscosity, which has a greater effect in lower velocity impacts. The different EOSs used by Pierazzo et al.

[110] likely contributed to the differences in results among the codes. One hydrocode tested by Pierazzo et al. [110], RAGE, also used a SESAME tabular EOS. Comparing these two codes, both implementing the SESAME EOS, I see a maximum pressure of 35.5 GPa in RAGE and 55.7 GPa in FLAG. The RAGE maximum pressure deviates from the 1D analytic by -39.55%, while the FLAG maximum pressure deviates from the 1D analytic by -5.15%. Thus, variations in the results among the codes are unlikely to be solely because of the choice of EOS.

### *6.3.1 Mesh Resolution Study*

I conducted a mesh resolution study to determine at what resolutions FLAG converges for both impact velocities in the 2D aluminum-on-aluminum verification problem. To do this study, I measured the shock pressure decay 10 km into the aluminum target by placing 20 approximately evenly spaced static tracer points normal to the target surface, with the first located at the point of impact and the last located 10 km into the target. I recorded the pressure at each tracer point and plotted the maximum at each point. Mesh resolutions 5, 10, 20, and 40 cppr were tested, and the results are shown in Figure 6.6.

The shock pressure decay convergence of the hydrocodes tested by Pierazzo et al. [110] ranges from 20 cppr to 80 cppr for both impact velocities (see Figure 6.7), while FLAG appears to converge at 10 cppr for the 5 km/s impact velocity. For the 20 km/s impact velocity, FLAG performs well at 10 cppr, but the difference between the 10 cppr resolution and higher resolutions is evident. This difference may be a result of the increased material deformation that occurs at higher impact velocities, which requires more precise physics modeling. From this study, I can expect reasonable results using a 10 cppr resolution for lower impact velocities. For higher impact velocities, a higher resolution may be necessary, although 10 cppr may be suf-

ficient in some cases. The convergence at coarser resolutions could be a result of how FLAG handles multi-material zones. FLAG keeps interfaces sharp so numerical diffusion is not an issue at interfaces. FLAG also does not enforce pressure-temperature equilibrium (PTE), which allows zones to have two distinct materials with distinct pressures and temperatures. These properties aide in the implementation of the EOS, as multi-material zones will deform based on the bulk moduli of the materials in the zone. These features allow FLAG to run a coarser mesh without numerical smearing, heating, and cooling [24, 25].

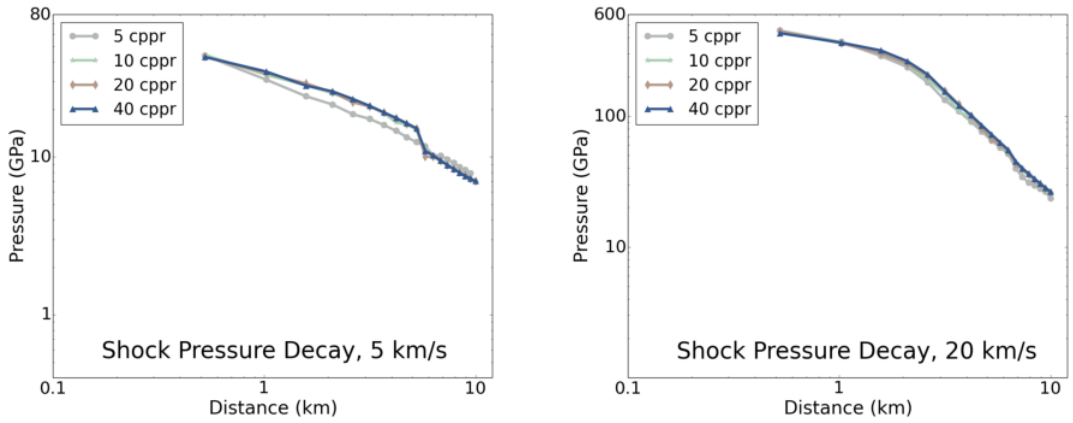


(a) (b)

**Figure 6.6:** Shock Pressure Decay of Aluminum-on-Aluminum Verification Problem with Resolutions Ranging from 5 to 40 cppr. (a) For an Impact Velocity of 5 km/s, FLAG Appears to Converge at a Resolution of 10 cppr. (b) For an Impact Velocity of 20 km/s, FLAG Appears to Converge at a Slightly Higher Resolution, Although at 10 cppr, Results May Be Sufficient in Some Cases.

The lower resolution required for FLAG simulations means the computational cost of these simulations can be greatly reduced. Figure 6.8 shows the computation time for the pressure wave to propagate 10 km into the aluminum target. The highest resolution, 40 cppr, ran for approximately 28 hours, while the 10 cppr resolution simulation ran for approximately 25 minutes. For the 5 km/s impact, which converged

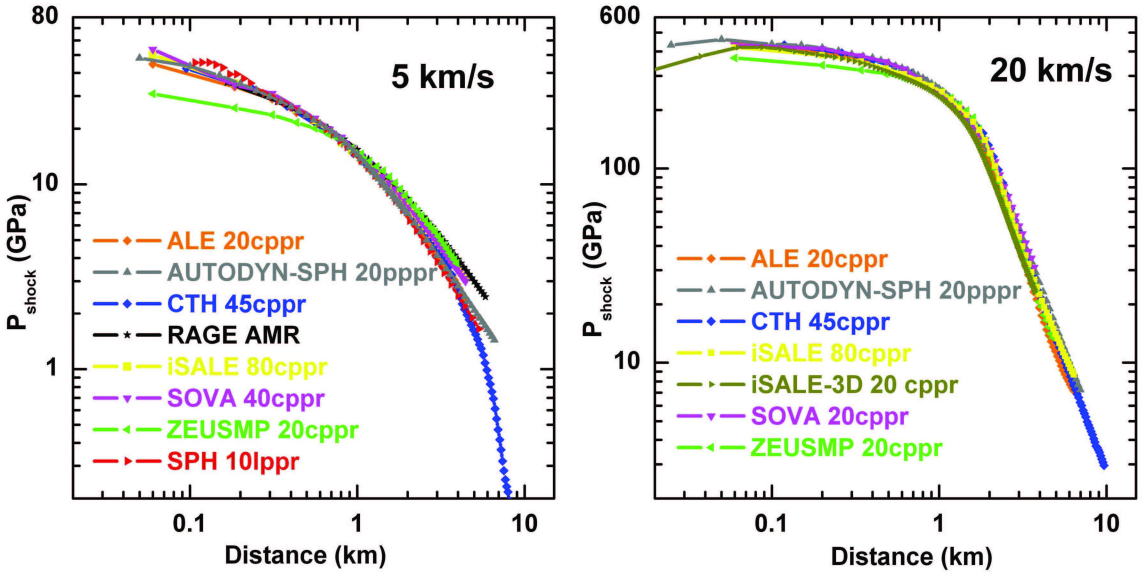


**Figure 6.7:** Fig. 1 from Pierazzo et al. [110], Showing the Shock Pressure Decay for a Variety of Tested Hydrocodes for the Aluminum-on-Aluminum Verification Problem. As Indicated by the Figures, the Majority of Hydrocodes Tested Converged at 20 cppr or Higher for the 5 km/s Impact and at 20 cppr for the 20 km/s Impact. This Figure was Approved for Reproduction in This Dissertation by John Wiley and Sons under License Number 4518410513813.

at 10 cppr, using FLAG reduces the computational cost considerably. All 5 km/s impact simulations ran on 108 processors, and all 20 km/s impact simulations ran on 144 processors.

### *6.3.2 2D Strength Results*

To further demonstrate FLAG's modeling capabilities, I simulate the verification problems with material strength. At high impact velocities, the target material is analogous to a strengthless material. At lower impact velocities, target strength affects the final crater. Because Pierazzo et al. [110] did not consider material strength for the verification problems presented here, I compare the maximum pressures from the FLAG simulations with material strength to my strengthless FLAG simulations. I simulated the verification problem in 2D using five constitutive models for mate-

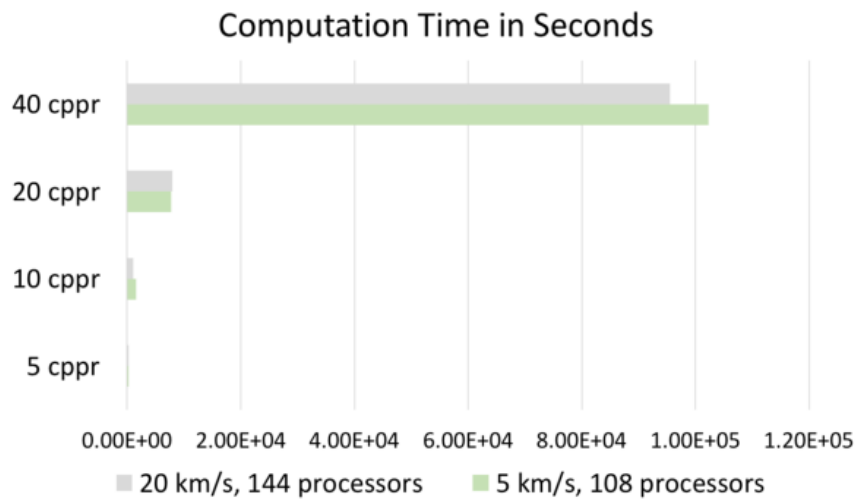


**Figure 6.8:** Computational Times for FLAG Simulations of the Pressure Wave Propagation 10 km into Target in an Aluminum-on-Aluminum Verification Problem. Simulations of the 5 km/s Impact Ran on 108 Processors, and Simulations of the 20 km/s Impact Ran on 144 Processors.

rial strength (described in Section 6.2) to account for the material response. Using constitutive models should result in lower maximum pressures because solid metals undergo reversible deformation until the yield threshold is reached. Prior to reaching the yield threshold, the material remains in the elastic regime, where energy is not required for deformation. My results were consistent with expectations, with lower maximum pressures in the strength runs than in the strengthless runs. Maximum pressures for the 20 km/s were considerably lower when using strength, consistent with my expectations that impacts at such high velocities render the material essentially strengthless for the purposes of modeling. Furthermore, the constitutive models I used may not account for the material physics at high strain rates. In addition, the 1D analytic solution depends on density and sound speed. At higher impact velocities, the compression stage of impact cratering results in an increase in material density, leading to a reduction in the material sound speed. The results from these runs are listed alongside results from the strengthless FLAG runs in Tables 6.3 and

6.4. As in Table 6.2, the maximum pressures listed in the table were measured at the point of impact using a static Eulerian tracer particle for the 5 km/s impacts and a Lagrangian tracer particle for the 20 km/s impacts. All of the strength runs had a resolution of 40 cppr. A complete list of parameter values for each material model can be found in Appendix E.

Impact Velocity: 5 km/s

| Strength Model | Maximum Pressure | Deviation from 1D Analytic |
|---|---|---|
| Strengthless | 59.58 GPa | 1.46% |
| Perfect Plasticity | 57.96 GPa | -1.30% |
| Linear Hardening | 57.96 GPa | -1.30% |
| Johnson-Cook | 57.86 GPa | -1.47% |
| Steinberg-Guinan | 57.86 GPa | -1.47% |
| Preston-Tonks-Wallace | 57.84 GPa | -1.51% |

**Table 6.3:** Maximum Pressures at the Point of Impact Obtained from 2D FLAG Simulations of the Aluminum-on-Aluminum Verification Problem Using Strength Models for the 5 km/s Impact.

Impact Velocity: 20 km/s

| Strength Model | Maximum Pressure | Deviation from 1D Analytic |
|---|---|---|
| Strengthless | 494.81 GPa | -2.26% |
| Perfect Plasticity | 483.90 GPa | -4.41% |
| Linear Hardening | 483.90 GPa | -4.41% |
| Johnson-Cook | 483.91 GPa | -4.41% |
| Steinberg-Guinan | 483.91 GPa | -4.41% |
| Preston-Tonks-Wallace | 483.90 GPa | -4.41% |

**Table 6.4:** Maximum Pressures from a Lagrangian Tracer Particle Initialized at the Point of Impact Obtained from 2D FLAG Simulations of the Aluminum-on-Aluminum Verification Problem Using Strength Models for the 20 km/s Impact.

## 6.4 Validation

To validate FLAG for impact cratering, I use the same validation problem as in Pierazzo et al. [110], a laboratory experiment of glass impacting water (see Appendix F for simulation details). In this experiment, a 2-mm-diameter glass sphere impacts a rectangular target of dimension 76 cm $\times$ 38 cm $\times$ 23 cm. The target as a 1.25 cm aluminum liner, with the remaining volume filled with water. The impact velocity is 4.64 km/s.

Table 3 in Pierazzo et al. [110] shows the experimental data for crater radius and depth over time. The first data point occurs 0.191 ms after impact, and the last occurs 83.187 ms after impact. The crater obtains its maximum radius of 14.357 cm at the last data point and its maximum depth of 12.1 cm at the penultimate data point, 65.335 ms after impact. These experimental data are displayed in Table 6.5.

In order to avoid boundary effects in the validation problem, I use a computational mesh extending from 0 cm to 36.75 cm in the $x$ direction and 1.25 cm to 1000 cm in the $y$ direction. Because of the relatively small size of the glass impactor compared to the water target, I vary the mesh resolution, using a finer mesh around the impactor and a coarser mesh far from impact. The zone sizes range from 0.02 cm, equivalent to 5 cppr, at impact and 0.5 cm, equivalent to 0.2 cppr, at the boundaries. To further reduce the computational cost, I omit the aluminum liner and only include the right half of the water, choosing a 2D axisymmetric mesh. The glass impactor is a semicircle of radius 1 mm, positioned at the top of the water at initialization. The surrounding air extends to a height of 10 m to avoid top boundary effects. The 10 km boundary is high enough to prevent the ejected water from contacting the top boundary and splashing down into the crater while the crater is forming. I use a constant gravity of -9.8 m/s$^2$ in the $y$ direction. Figure 6.9 shows the problem at

| Time (ms) | Radius (cm) | Depth (cm) |
|---|---|---|
| 0.191 | 1.608 | 2.35 |
| 0.382 | 2.297 | 2.6 |
| 0.764 | 2.963 | 3.32 |
| 1.146 | 3.423 | 3.85 |
| 1.91 | 4.112 | 4.61 |
| 3.436 | 5.031 | 5.39 |
| 5.72 | 6.064 | 6.41 |
| 9.516 | 7.098 | 7.514 |
| 15.18 | 8.316 | 8.83 |
| 22.666 | 9.487 | 9.7 |
| 31.9 | 10.636 | 10.602 |
| 44.553 | 11.807 | 11.46 |
| 65.334 | 13.3 | 12.1 |
| 83.187 | 14.357 | 12.054 |

**Table 6.5:** Experimental Data of Crater Radius and Depth over Time for the Glass-on-Water Validation Problem [110].

initial time.

This problem was considerably more computationally expensive than the aluminum verification problem. The small size of the impactor relative to the target limited the resolution size. Many of the hydrocodes tested by Pierazzo et al. [110] did not run to completion, and, instead, the authors displayed the crater dimensions that coincided with the first several experimental data points. Because of the computational intensity of the problem, I ran the simulation up to 9.516 ms, which encompasses eight experimental data points. The hydrocodes tested by Pierazzo et

(a) (b)

**Figure 6.9:** Glass into Water Validation Problem at Initial Time of FLAG Simulation Showing the Glass Impactor (White), Water Target (Blue), and Surrounding Air (Grey). (a) The Entire Computational Space for the Glass into Water Validation Problem. (b) Glass into Water Computational Space, Zoomed to Show Detail.

al. [110] used resolutions ranging from 5 cppr to 20 cppr for this validation problem. I used a resolution of 5 cppr at the point of impact, which is the coarsest resolution tested in the verification problem. I chose such a coarse resolution because of the computational cost as well as the relative size of the impactor when compared to the target. Finer resolutions cause the adaptive time step to become arbitrarily small, prohibiting the simulation from providing meaningful results in an acceptable time frame. I ran the simulation in blocks of 10 hours on 360 processors. The first 10-hour run resulted in seven data points. The second 10-hour run provided the 8th data point. An additional eleven 10-hour runs produced no additional data points. In addition to the coarse resolution, I chose to run this simulation using FLAG's Eulerian mesh relaxer to prevent tangling during the excavation stage of crater formation.

Because I used a coarse mesh, I anticipated that the FLAG simulations results would underestimate crater dimensions as had hydrocodes tested by Pierazzo et al.

[110] when run with the 5 cppr resolution. At this resolution, these codes underestimated the crater radius by about 11% on average and underestimated the the depth by about 14% [110], while FLAG overestimated the crater depth by an average of 2.44% and underestimated the radius by an average of 6.2%. The overestimation of the depth could be a result of the axisymmetric boundary condition, which tends to result in jets that are too thin and penetrate too far because movement is allowed in only one direction and will be dominated by gravity. I measured the crater radius at 0.1 cm below the initial water line, and I measured the crater depth 0.3 cm to the right of the crater's center. The results of the FLAG simulation as well as the corresponding experimental data are listed in Table 6.6 and shown in Figure 6.10.

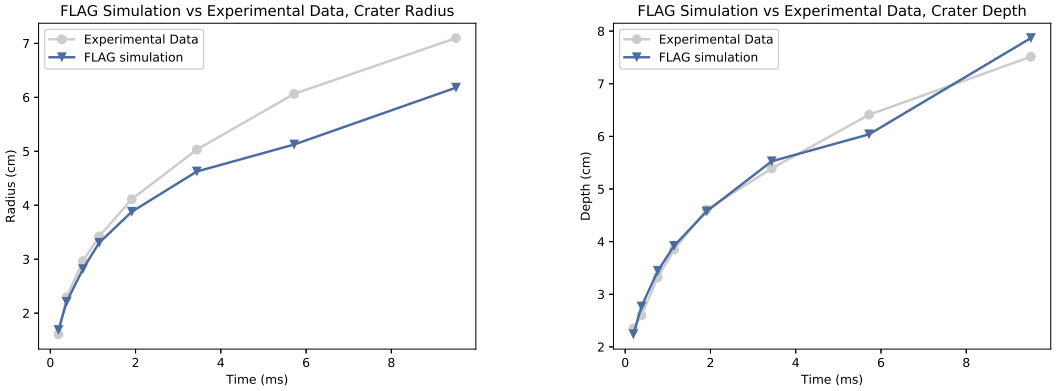


(a) (b)

**Figure 6.10:** Experimental Data and FLAG Simulation Results for the Glass-on-Water Validation Problem for Crater Radius (Left) and Crater Depth (Right) over Time. The FLAG Simulation Had an Average Relative Error of about -6.2%, and the Depth Had an Average Relative Error of 2.44%.

The depth-to-radius ratios of both the FLAG simulations and experimental data are listed in Table 6.7 and shown in Figure 6.11a. The resulting FLAG simulation crater 1.146 ms after impact, reflected about the axis of symmetry, is shown in Figure 6.11b.

| Time (ms) | Experimental Radius (cm) | FLAG Radius (cm) | Relative Error | Experimental Depth (cm) | FLAG Depth (cm) | Relative Error |
|---|---|---|---|---|---|---|
| 0.191 | 1.608 | 1.68713 | 4.92% | 2.35 | 2.23934 | -4.71% |
| 0.382 | 2.297 | 2.20879 | -3.84% | 2.6 | 2.7669 | 6.42% |
| 0.764 | 2.963 | 2.81574 | -4.97% | 3.32 | 3.44335 | 3.72% |
| 1.146 | 3.423 | 3.30393 | -3.48% | 3.85 | 3.91973 | 1.81% |
| 1.91 | 4.112 | 3.87845 | -5.68% | 4.61 | 4.57374 | -0.79% |
| 3.436 | 5.031 | 4.62491 | -8.07% | 5.39 | 5.52639 | 2.53% |
| 5.72 | 6.064 | 5.12498 | -15.49% | 6.41 | 6.03864 | 5.79% |
| 9.516 | 7.098 | 6.179 | -12.95% | 7.514 | 7.868 | 4.71% |

**Table 6.6:** FLAG Simulation Results of Glass-on-Water Impact Validation Problem with Relative Errors, Rounded to Two Decimal Places. The Codes Tested by Pierazzo et al. Had an Average Error of about -11% for Radius and -14% for Depth [110].

I used FLAG's subcycling capability on this validation problem in order to ob-

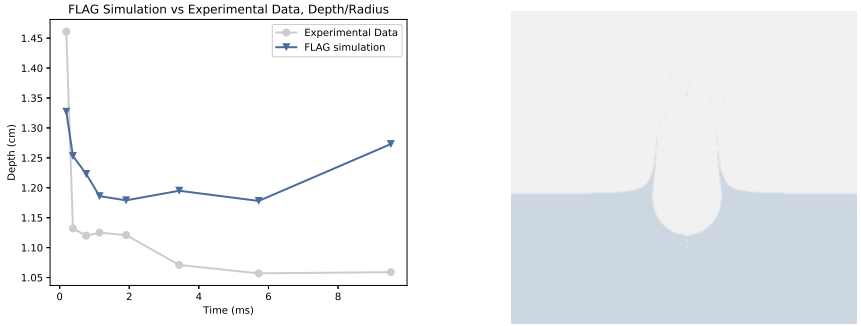


(a) (b)

**Figure 6.11:** (a) Depth/Radius Ratio of Experimental Data and FLAG Simulation for the Glass-on-Water Validation Problem. (b)

FLAG Simulation Crater 1.146 ms after a 2 mm Diameter Glass Sphere Impacts a Water Target at 4.64 km/s, Reflected about the Axis of Symmetry.

| Time (ms) | Experimental Depth/Radius | FLAG Depth/Radius | Relative Error |
|---|---|---|---|
| 0.191 | 1.461 | 1.327 | -9.17% |
| 0.382 | 1.132 | 1.253 | 10.69% |
| 0.764 | 1.120 | 1.223 | 9.20% |
| 1.146 | 1.125 | 1.186 | 5.42% |
| 1.91 | 1.121 | 1.179 | 5.17% |
| 3.436 | 1.071 | 1.195 | 11.58% |
| 5.72 | 1.057 | 1.178 | 11.45% |
| 9.516 | 1.059 | 1.273 | 20.21% |

**Table 6.7:** FLAG Simulation Results of the Depth-to-Radius Ratio Compared to Experimental Data for the Glass-on-Water Validation Problem.

tain more accurate results without increasing the mesh resolution, which proved too computationally intensive. Subcycling allows for extra iterations during the mesh remapping process. This method provided fewer data points for the same computational time, but the results for the early simulation time resulted in errors as low as -0.17%. The average error for the crater radius was -5.04%, and the average error for the crater depth was -5.03%. Subcycling resulted in a nearly identical average error for both the crater radius and crater depth.

## 6.5 Conclusions

Based upon the verification and validation problems, I conclude that the FLAG hydrocode can be used for impact cratering simulations. I have shown through the verification problem that FLAG captures the important shock dynamics in early stages of crater formation, and I have shown through the validation problem that FLAG

matches experimental data with a low relative error. These problems have been accepted by the planetary science community as adequate tests for hydrocodes. FLAG simulated the verification problem of aluminum into aluminum producing maximum pressure values close to the analytical solutions, with errors as low as 4.2% compared to a mean error of 33.3% in results from the hydrocodes tested by Pierazzo et al. [110]. The mesh resolution study demonstrated FLAG's potential to handle impact cratering problems at coarser resolutions than other hydrocodes, reducing the computational time from 28 hours to 25 minutes. The validation problem of a glass impactor and water target was used to measure FLAG's ability to match experimental data. The FLAG simulation of this problem gave promising results despite a very coarse resolution, with errors an order of magnitude better than other hydrocodes tested at the same resolution [110]. The results from Pierazzo et al. [110], which I used for comparison with FLAG results, are from 2008. Although it is likely that many of these codes have undergone improvements since these results were first published, I was only able to compare to results available in the literature for these V&V problems. Accounting for material strength in the verification problems resulted in lower errors compared to the strengthless simulations for the lower velocity impact, indicating FLAG is able to correctly model material properties that play a key role in crater formation. FLAG's variety of EOS options, multiple material models, ALE capabilities, and relatively good run times contribute to its accurate modeling for both theoretical and experimental physical problems. These V&V problems tested FLAG's Lagrange, ALE, and Eulerian features, demonstrating FLAG's reliability for a variety of problem approaches.

# Chapter 7

# MODELING IMPACT STRUCTURES ON ASTEROID 16 PSYCHE

## 7.1 Introduction

Asteroid 16 Psyche is the largest M-type (metallic) asteroid in the Main Asteroid Belt (MBA) [82]. The upcoming NASA mission Psyche: Journey to a Metal World, set to launch in 2022, will reach Psyche in 2026 and orbit the asteroid for 21 months [69, 105]. Psyche is the largest exposed metallic body in the MBA, and the mission will be the first of its kind to visit a metallic body rather than one composed of rock or ice [45]. Psyche is likely the remnant of a differentiated planet core from a time when planetary accretion was disrupted by frequent solid-body collisions [45]. Hence, the mission to Psyche will provide an opportunity to explore a planetary core and provide insight into formation of the solar system [45]. The mission will be able to collect data to answer important questions about planetary formation and metallic bodies, including questions about crater formation in metallic bodies, topography of the asteroid, alloys present in the core, and how the once-molten body cooled to its current state [45].

Until this mission launches, our current means for collecting information about Psyche include radar, Infrared Astronomical Satellite (IRAS), and lightcurve inversion [72, 82, 124]. Hence, even basic information about Psyche is under debate. For example, estimates of Psyche's diameter range from 213 km to 264 km [82]. Estimates on Psyche's material properties vary considerably, particularly for bulk density and porosity. Radar albedo data indicate Psyche's surface is rich in metallic content [90]. Bulk density estimates typically range from $1.4 \pm 0.3$ g/cm$^3$ to $4.5 \pm 1.4$ g/cm$^3$, with

some as high as 7.6 g/cm$^3$, resulting in porosity estimates typically ranging from 30% to 70%, with some as low as 0% [74, 82, 124, 141]. M-type asteroids like Psyche have historically been viewed as differentiated planet cores [90]. Thus, information about Psyche could provide information into the early stages of the universe and planetary formation. Because estimates concerning Psyche are widely varied, there is a need for additional predictions leading up to the mission launch. More accurate predictions on the compositions of Psyche can ensure the mission is equipped with the appropriate tools for analyzing Psyche.

Psyche has two large impact structures in its Southern hemisphere [124]. These structures are estimated to be about 50 km to 70 km in diameter and up to 6.4 km deep [124]. The smaller of the two craters is the deepest location on Psyche, with an estimated depth of about 6.4 $\pm$ 0.64 km and estimated diameter of 53 $\pm$ 15 km, and the larger crater is estimated to be slightly less deep with an estimated diameter of 67 $\pm$ 15 km [124]. Modeling the formation of Psyche's craters can provide additional predictions for Psyche's material composition and bulk density by testing multiple compositions and densities and comparing the simulation results to the estimated crater dimensions. Because shock waves play a key role in crater formation, and because shock waves propagate differently through different material compositions, the resulting craters from varied compositions should also vary, and compositions closer to Psyche's actual composition should result in craters that better match the actual crater dimensions. The FLAG hydrocode, previously shown to be effective in modeling impact craters [30], is an ideal choice to model this crater. The probable impact velocities involving Psyche are between 4.434 km/s and 4.639 km/s [47]. In the previous chapter, I showed that FLAG converges at relatively low resolutions for velocities of 5 km/s. Velocities in this range indicate that material strength is a factor in crater formation, which FLAG is able to model well [30, 95]. Based upon the

probable impact velocity, local gravity, and bulk density estimates, the formation of Psyche's largest crater was dominated by strength rather than gravity [47, 65, 82, 124]. The transition between target strength and target local gravitational acceleration as the dominant effect that determines impact crater size and shape is a function of gravitational acceleration, impactor radius, and impact velocity [66]:

$$Y = \frac{ga}{U^2},$$

where $g$ is the gravitational constant, $a$ is the impactor radius, and $U$ is the impact velocity. The transition $Y$ is analogous to the $\pi_2$ scaling constant [95]:

$$\pi_2 = \frac{1.61g(2a)}{U^2},$$

with the same notation. Using 0.29 m/s$^2$ for Psyche's gravity, 5 km for the impactor radius, and 4.5 km/s for the impact velocity [47, 65, 66], the strength to gravity transition occurs at $Y = .323$. Calculating $\pi_2$ with the same values, $\pi_2 = 2.31 \times 10^{-4}$. Thus, the crater is in the strength regime.

## 7.2 Estimating Psyche's Largest Crater Profile in 2D

Crater classification involves many factors, including the size of the crater, the geographic features of the crater, and the body on which the crater exists [95]. Simple craters are bowl-shaped and typically have diameters less than 15 km on the moon and less than 3 km on Earth. The crater floor consists of broken rock, known as breccia, the result of debris falling into the crater after impact. Meteor Crater in Arizona in an example of a terrestrial simple crater [95]. Complex craters typically have diameters greater than 20 km on the moon and greater than 3 km on Earth. Complex craters are thought to be the result of the collapse of an initial bowl-shaped crater. The crater floor consists of highly shocked and melted debris, with the possibility of melt pools

[95]. The transition between simple and complex craters scales as the inverse of the gravitational acceleration $g$ [95]. Using $k$ to represent the proportionality constant, the transition can be expressed as $\frac{k}{g}$. Using Earth's gravitational acceleration of 9.8 m/s$^2$ converted to km/s$^2$, $k = 0.029$. To verify against the lunar gravitational acceleration of 1.6 m/s$^2$ converted to km/s$^2$, the transition to complex craters occurs when crater diameter reaches about 18 km, which is consistent with the expected transition [95]. Using this same process and Psyche's gravitational acceleration of 0.29 m/s$^2$ convert to km/s$^2$, the transition to complex craters on Psyche occurs when crater diameter reaches about 100 km.

Psyche's largest crater is estimated to be about 70 km in diameter, so I expect this to be a simple crater [124]. Psyche's deepest point is estimated to be about 6.4 km [124]. However, there is no information about the curvature of the crater profile. Using these depth and diameter estimates, I created two possible crater profiles. The first assumes that the crater is part of a circle, and the second assumes the crater is part of an ellipse. The impact angle plays a key role in crater shape. The most probable impact angle is 45$^o$ relative to vertical [95]. A crater that results from an oblique impact has bilateral symmetry with an asymmetric ejecta blanket. This effect becomes more pronounced as angle obliquity increases [95]. Circular impact craters result from high-velocity impacts with low obliquity [95]. I expect these profiles to be overestimates because Psyche's largest crater is slightly more shallow than the smaller crater [124].

For the circular profile, I assume the crater is a portion of circle cut by a chord having the same length as the crater's diameter, 70 km. The resulting crater has a depth of 6.4 km, the deepest possible estimate for the actual crater. To determine the radius, I let $r$ represent the circle's radius, and I define the angle between the the radius bisecting the crater and the radius intersecting the end of the chord to be $a$.

The resulting right triangle has sides of length 3.2 km (half of the chord length) and $r - 6.4$ km (length from center of circle to chord) and hypotenuse of length $r$. Figure 7.1 shows a schematic of such a circle. Using the Pythagorean Theorem, I determine the circle's radius (all units are in km):

$$\begin{aligned} (r-6.4)^2 + 35^2 &= r^2 \\ r^2 - 12.8r + 40.96 + 1225 &= r^2 \\ 1265.96 &= 12.8r \\ r &\approx 98.903125 \text{ km.} \end{aligned}$$

Thus, the equation for the circular crater profile is

$$x^2 + y^2 = 9781.82813,$$

where

$$x \in [-35, 35] \text{ and } y < 0.$$

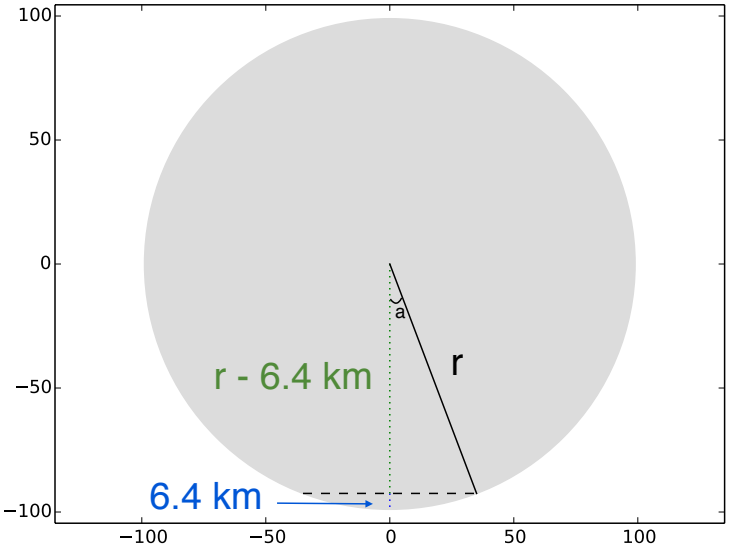


**Figure 7.1:** Depiction of Psyche's Largest Crater As Part of a Circle. The Dashed Black Line Is a Chord of Length 70 km, the Crater's Estimated Diameter. The Dotted Blue Line Has Length 6.4 km, the Maximum Depth on Psyche. The Crater is the Area Within the Circle Below the Dashed Black Chord.

For the elliptical profile, I assume the major axis is the crater diameter (70 km) and the minor axis is twice the crater depth (12.8 km). Using the formula for an ellipse, the equation of the crater profile is

$$\frac{x^2}{35^2} + \frac{y^2}{6.4^2} = 1,$$

where

$$x \in [-35, 35] \text{ and } y < 0.$$

Figure 7.2 shows these two crater profiles.

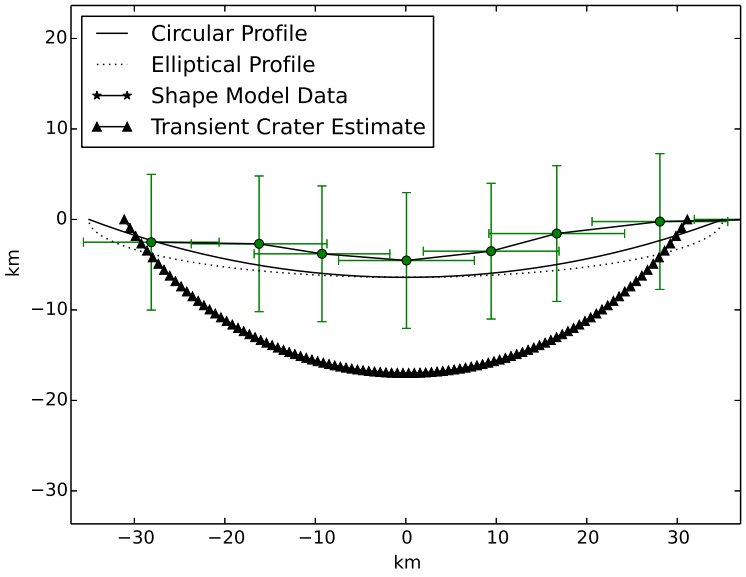


**Figure 7.2:** Crater Profiles of Psyche's Largest Crater As Part of a Circle (Solid) and Part of an Ellipse (Dashed). The Transient Crater Estimate Is In Black with Triangles, and the Shape Model Profile Is Shown with Error Bars (Green).

## 7.3 2D Simulations

I began with a series of 2D axisymmetric simulations in order to investigate a variety of materials with reduced computational resources (see Appendix F for simulation details). For these runs, I modeled Psyche as a circle of radius 125 km and

the impactor as a circle of radius 5 km, consistent with estimates in the literature [65, 124], and I modeled the surrounding material as a void. The choice of using a circle for Psyche has several benefits in 2D. If Psyche is the remnant of a differentiated planetessimal, the gravity of the parent body could have hydrostatically pulled the core into a round shape. Because these 2D simulations are primarily to explore material aspects of Psyche, I chose to run them axisymmetric to make better use of computational resources while still allowing meaningful predictions from simulation results. These 2D simulations will indicate whether future simulations should include different shapes for Psyche. I chose an impact velocity of 4.5 km/s, consistent with the probable impact velocities of collisions involving Psyche, and an impact angle normal to Psyche's surface [47]. The computational domain ranged from 0 to 500 km in both the $x$ and $y$ dimensions, and the resolution was about 15 cells per projectile radius, for a total of 2301285 zones. I used an Eulerian remap after each time step.

### *7.3.1 Strengthless Results*

In Chapter 6, I discussed when material strength is expected to play an important role in impact crater formation. For an impact velocity of 4.5 km/s, I expect results incorporating material strength to be a better match for the crater dimensions than results using strengthless materials.

To verify that strength indeed plays a role, and to rule out very high impact velocities, I ran strengthless simulations with three materials for both target and impactor: nickel; iron; silicon dioxide. I chose nickel and iron because M-type asteroids are assumed to be rich in these metals [90]. I chose silicon dioxide ($SiO_2$) because silicon and oxygen may be present in liquid core, and $SiO_2$ crystalizes as the core cools [62]. As I expected, these simulations resulted in craters much larger than the estimates for the actual crater, with depths around 65 km and radii around 42–43 km. Figure

7.3 shows the crater profiles from these strengthless simluations plotted alongside the circular and elliptical profiles based on crater dimension estimates.

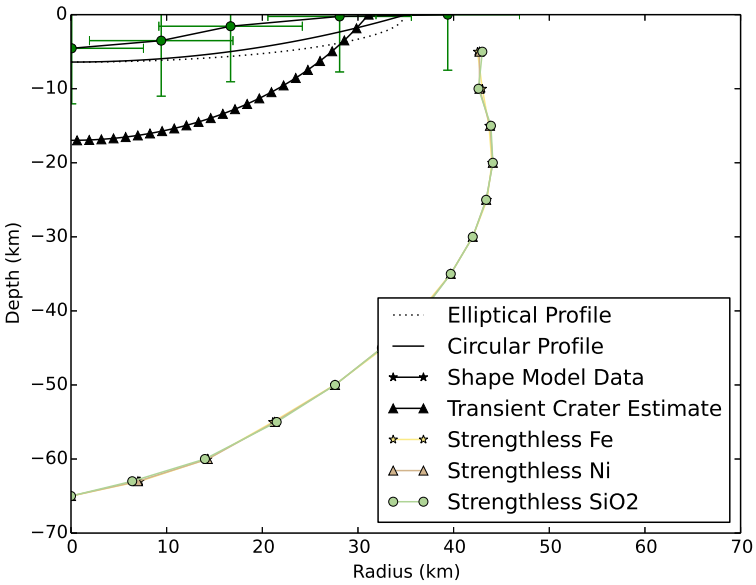


**Figure 7.3:** Crater Profiles from 2D Strengthless Simulations Using Iron, Nickel, and Silicon Dioxide Compared to Crater Profiles Created from Crater Dimension Estimates.

### *7.3.2 Solid Material Results*

Because I expect strength to play a role in the formation of Psyche's largest crater, and because my strengthless results supported this hypothesis, I ran simulations using a variety of materials and models for both impactor and Psyche. A detailed description of the materials models is located in Chapter 6, Section 6.2. The materials I used for Psyche were iron, nickel, and Monel, a nickel-copper alloy that contains titanium, aluminum, silicon, and iron [126]. Monel was modeled after ore from Sudbury basin, a large impact structure in Canada [117, 126]. The location of the metal in an impact structure indicates it could have come from the impactor that formed the structure and is likely to have similar properties to extraterrestrial metallic bodies. Table 7.1

lists the materials and models used in each simulation. The material models are abbreviated as follows: Preston-Tonks-Wallace (PTW) [115]; Steinberg-Guinan (SG) [130]; perfect plasticity (pp) [128]. The Mie-Grüneisen EOS is abbreviated MG (see Chapter 5, Section 5.4). The material model equations are in Chapter 6, Section 6.2. Parameter values are listed in Appendix E. Figure 7.4 shows the crater profiles of these simulations.

| Impactor Material | Impactor Material Model | Impactor EOS | Psyche Material | Psyche Material Model | Psyche EOS |
|---|---|---|---|---|---|
| Monel | SG | MG | Monel | SG | MG |
| Iron | PTW | SESAME | Iron | PTW | SESAME |
| Silicon dioxide | pp | SESAME | Iron | PTW | SESAME |
| Silicon dioxide | pp | SESAME | Monel | SG | MG |
| Silicon dioxide | pp | SESAME | Nickel | SG | SESAME |

**Table 7.1:** Material Information for Simulations of the Formation of Psyche's Largest Impact Crater.

Figure 7.5 shows the crater formation in the simulation using silicon dioxide as the impactor and Monel as Psyche. The images in the figure show the progression of crater formation as material is ejected from the crater. As this happens, the material that follows the excavation trajectory but is not ejected results in an overturned flap with inverted stratigraphy [125].

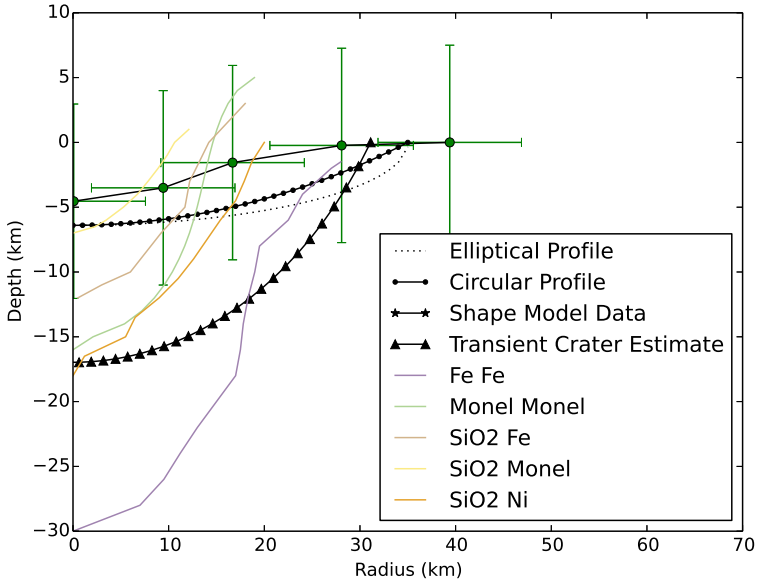


**Figure 7.4:** Crater Profiles from Simulations Run with Material Models. The First Listed Material Indicates the Impactor Material, and the Second Listed Material Indicates the Material Used for Psyche.

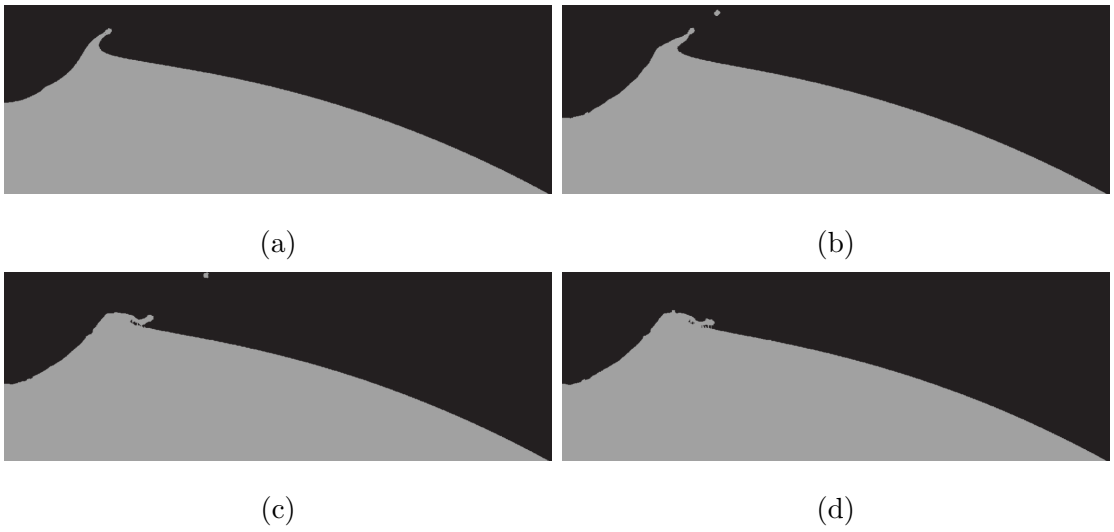


**Figure 7.5:** Images from the $SiO_2$-Monel Simulation Showing the Eventual Overturned Flap.(a) Ejected Material Follows Expected Trajectory out of Crater; (b) Hinge Forms During Crater Excavation; (c) Material Collapses at Hinge; (d) Flap of Hinged Ejected Material Has Overturned.

### *7.3.3 EOS Effects*

I chose the alloy Monel because of its probable extraterrestrial origin. However, unlike the other materials used in these models, there is not an associated SESAME EOS for Monel. Instead, I used a Mie-Grüneisen analytical EOS using parameters available in the literature [131]. This EOS, however, does not account for phase transitions. Thus, there is neither melted nor vaporized material in the Monel-Monel impact, while other simulations have a noticeable vapor plume. The Monel-Monel simulation does not reach melt temperature, while simulations using SESAME EOSs do in a small portion of the crater. In the later times of these simulations, the hot material has very low density and has either been ejected from the crater or exists in the vapor plume. In impact velocities below 12 km/s, which is the regime of these simulations, the melt mass is very low [95]. Thus, melted or vaporized material is unlikely to play a large role in the crater formation.

To better understand the effects of the EOS, I examined the pressures in these simulations at the same time step for several times during the simulation. The pressures in simulations model Psyche as iron with a SESAME EOS versus Monel with a Mie-Grüneisen EOS were comparable, varying on the order of $10^{-2}$ GPa. Because these simulations used distinct yet similar materials, I concluded that the EOS was unlikely to be affecting the shock wave from the impact in a significant way.

When zones have mixed materials in FLAG, a volume fraction tolerance is implemented to remove materials below tolerance. In my simulations, I set this value to be 1e-13 so that the maximum material removed from any one cell would be 1 part in 10 trillion. This tolerance ensures that the amount of energized low-density material removed does not adversely affect the energy conservation of the simulation. I verified this by using FLAG's built-in energy check at a simulation time of 4 seconds, which

is sufficient for the pressure wave to have passed through the crater area and lessened in intensity. For the Monel-Monel simulation, the amount of energy lost was slightly less than 0.01%.

### *7.3.4 Porosity Study*

After running simulations of strictly solid materials, I chose Monel for a porosity study. I chose Monel because of its origin from an impact structure, indicating it is likely similar to metallic solid bodies in the solar system. Another justification for Monel is that solid simulations ran well, showing an overturned flap, and did so in relatively short computational time. For the porosity study, I initialized Psyche with 30%, 50%, 60%, 70%, and 80% porosity. I kept the impactor as solid. In these simulations, pore collapse was not accounted for. Hence, the pores in the target material deform consistently with the solid target material, resulting in a stiffer material. I expect this additional stiffness to affect crater modification and result in a smaller crater. Figure 7.6 shows the crater profiles from the porosity simulations.

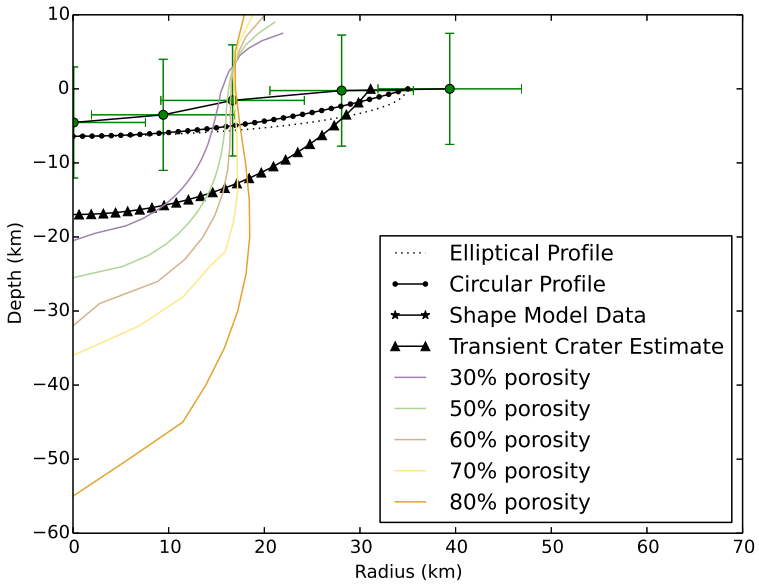


**Figure 7.6:** Crater Profiles from Monel-Monel Simulations with Porosity.

### *7.3.5 Conclusions from 2D Simulations*

Based on these simulations, I predict that Psyche's composition is indeed highly metallic. I also predict that Psyche's composition is porous rather than solid. From the resulting craters in these simulations, I predict that the impact angle that formed the crater was oblique rather than normal. This prediction is based largely on Psyche's reported crater dimensions as well as the V&V results from Chapter 6, which indicate a depth-to-radius ratio close to 1 for normal impacts. Because I predict an oblique impact, 3D simulations are the next logical step. In order to ensure the 3D simulations provide more realistic results than the 2D simulations, I will use a shape model for Psyche to better capture it's geometric features.

## 7.4 3D Simulations

The 2D axisymmetric scoping tested a variety of materials, material models, and porosities. Based on the solid runs, a Monel target with either a silicon dioxide impactor or a Monel impactor showed the most promising results. The Monel-Monel solid impact showed an overturned flap, and the $SiO_2$-Monel impact showed good agreement with crater depth. However, it is important to note that impact gardening — continued impacts over time — affect the shape of the crater. On Earth, crater evidence erodes through natural processes such as volcanic activity, water flow, and wind erosion. On bodies without these processes, and without atmosphere, crater evidence erodes through continued impacts, which can deposit new material into an existing crater.

My porosity study indicated that increased porosity resulted in increased crater dimensions, consistent with experimental results of vertical impacts into porous targets. In several such experiments, crater depth increased as porosity increased [23, 119, 120]. This depth increase could be the result of the increased ejected mass in such impacts, which can result in a vapor plume of mass 5–6 times the mass of the impactor [119]. For both solid and porous runs, the crater shape did not match well, because the actual crater is estimated to be considerably wider than it is deep. The crater shapes from the 2D simulations were similar to those from the 2D validation problem presented in Chapter 6, which was a normal impact. For this reason, I expect the impact angle that formed the crater was not a normal (vertical) impact but rather an oblique one. Thus, my 3D simulations incorporated oblique impact angles.

To set up my 3D simulation, I used a shape model of Psyche [70]. I added a spherical cap to cover the existing craters. This cap contained the same material composition that I used to model Psyche in each simulation so that the target com-

position remained constant. I ran 3D simulations of $SiO_2$ impacting Monel and Monel impacting Monel at impact angles of 30° and 60° relative to vertical (see Appendix F for simulation details). I used solid materials for the impactor, and I used solid, 30% porous, and 50% porous materials for Psyche. All material models in the 3D simulations were the same as in the 2D simulations. Table 7.2 lists the dimensions of the craters in these simulations as well as the estimated dimensions of the actual crater.

| Crater | Dimension | | | 6.4 ± 0.64 km [124] | 67 ± 15 km [124] |
|---|---|---|---|---|---|
| Impactor | Psyche | Porosity | Angle | Depth | Diameter |
| Monel | Monel | Solid | 45° | 7 km * | 35.1438 km |
| Monel | Monel | Solid | 60° | 5.3 km | 36.8 km |
| $SiO_2$ | Monel | Solid | 45° | 0.1 km | 41.0122 km |
| $SiO_2$ | Monel | Solid | 60° | 1.1 m | 28.5 km |
| Monel | Monel | 30% | 45° | 5.5 km | 39.598 km |
| Monel | Monel | 30% | 60° | 10.4 km | 51.5 km † |
| Monel | Monel | 50% | 45° | 14.5 km | 42.4264 km |
| Monel | Monel | 50% | 60° | 12 km | 60 km * |

**Table 7.2:** Crater Dimensions from 3D Simulations. * Indicates the Simulation Value Was within the Error Bar of the Actual Crater Dimensions. † Indicates That the Simulation Value Lies within the Error Bar of the Actual Crater Dimensions after Correcting for the Expected Numerical Error from the Validation Simulation in Chapter 6 (up to 15.5% Underestimation for Radius and up to 6.5% Overestimation for Depth). The Material Models and EOSs Are the Same As in Table 7.1.

As expected, the porosity simulations resulted in crater dimensions closer to the actual estimates. The 3D simulations showed the crater formation as well as ejected material leaving the body of the asteroid. Figure 7.7 shows the Monel-Monel simulation with a 45-degree impact angle and no porosity about 92 seconds after impact.

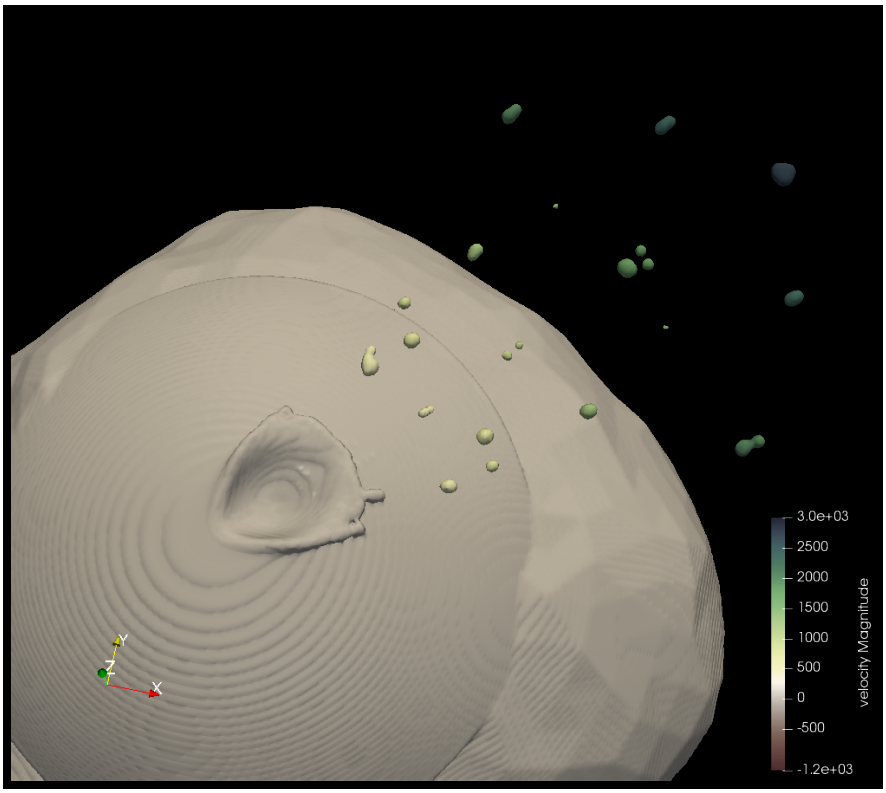


**Figure 7.7:** Simulation of Crater Formation from a Monel-Monel 45-Degree Impact about 92 Seconds after Impact, Colored by Velocity.

Figure 7.8 shows the crater formation over time for the Monel-Monel 60-degree impact with 50% porosity. The images show the contact and compression, excavation, and crater modification stages.

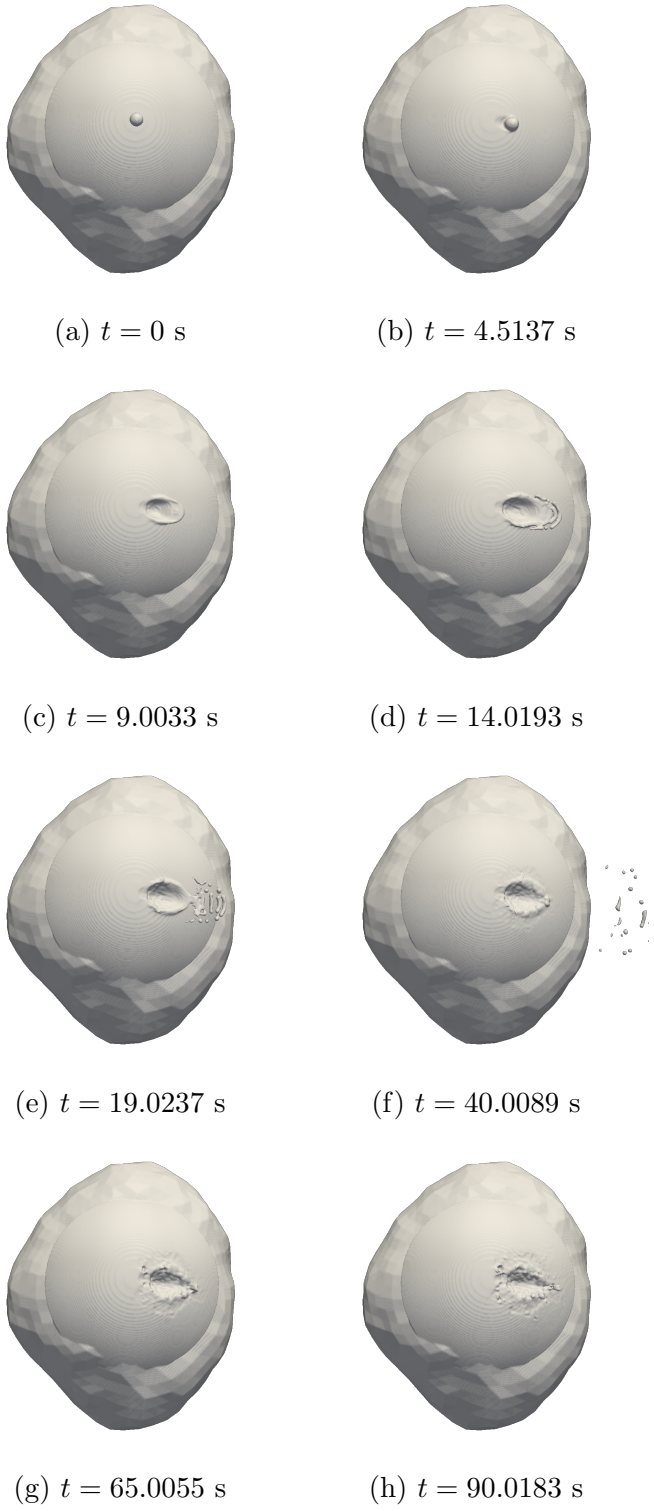

(a) $t = 0$ s (b) $t = 4.5137$ s

(c) $t = 9.0033$ s (d) $t = 14.0193$ s

(e) $t = 19.0237$ s (f) $t = 40.0089$ s

(g) $t = 65.0055$ s (h) $t = 90.0183$ s

**Figure 7.8:** Crater Formation from a Monel-Monel 60-Degree Impact with a 50% Porous Target.

From the V&V of the FLAG hydrocode in Chapter 6, I expect that my simulations may overestimate the depth by about 1.8% to 6.5%, and I expect the radius to be underestimated by about 3.4% to 15.5%. Considering the 67 ± 15 km crater diameter estimate, several of the simulations had acceptable crater diameters. The 6.4 ± 0.64 km depth estimate is likely to be an overestimate because this crater is shallower than the smaller crater [124]. The diameter of the Monel-Monel 60° impact with 50% porosity was within the error bars of the data, and the depth of the Monel-Monel 45° solid impact was within the error bars from the data as well. When accounting for expected numerical errors from the validation problem in Chapter 6, the Monel-Monel 60° impact with 30% porosity had a diameter within the error bars from the data. I predict that a silicon dioxide impactor was unlikely at the tested impact angles because the resulting craters were far too shallow. Several of the Monel-Monel impacts were very near the error bars and may match better at different impact angles.

## 7.5 Conclusions

I modeled the formation of Psyche's largest impact crater in order to determine Psyche's likely material composition using the FLAG hydrocode. I determined that silicon dioxide and Monel were the two materials that resulted in craters with the closest match to the actual estimated crater dimensions through 2D solid simulations. While silicon dioxide as an impactor had a good match with crater depth in 2D, the crater diameter was much smaller than the actual crater. Monel impacting Monel led to the only instance of the overturned flap in 2D, indicating the models in that simulation better matched the actual physics involved in cratering. However, the Monel-Monel impact was too deep as well as too small in diameter. My porosity study in 2D showed that increased porosity in Psyche led to larger craters. I concluded that

Psyche is likely porous because the solid material simulations had craters that were too small in diameter, porosity is likely present in Psyche. The overestimate of the depth in most of the 2D simulations indicated that the impact itself was likely oblique rather than normal.

I set up 3D full scale simulations using the results from my 2D scoping runs. I chose Monel for the material of Psyche, and I varied the porosity. I used a silicon dioxide impactor as well as a Monel impactor, and I used two different impact angles. Several of my 3D simulations matched well with the estimated crater dimensions. One simulation achieved a crater diameter of 60 km compared to the estimated 70 km, and another had a depth of 7 km compared to an estimate of 6.4 km.

From my simulations, I predict that Psyche is indeed likely mostly metallic with a porosity of about 50%. These predictions are consistent with the idea that M-type asteroids such as Psyche are differentiated planet cores. I also predict that the impact angle that led to Psyche's largest crater was likely an oblique impact of at least 45° from vertical, possibly more. Future work will include modeling the smaller of the two impact structures, estimated to be smaller in diameter but slightly deeper than the larger counterpart.

# Chapter 8

# CONCLUSIONS

The purpose of this work was to demonstrate the important role of differential equation models when addressing problems beyond experimental capabilities. In this work, I addressed two different types of problems by developing and analyzing ordinary differential equation models and using computer simulations of partial differential equation models.

In Chapter 3, I used an $SIR$ modeling approach for a novel use: prescription drug abuse. In this chapter, I developed two ODE models to describe the most common path to Vicodin abuse in the United States. Through adjoint sensitivity analysis, I determined that prevention is more effective than treatment at mitigating the number of people abusing Vicodin. The work in this chapter introduces a novel tool to address the prescription drug abuse epidemic. While the models presented in this chapter concerned Vicodin specifically, they could be adapted to include a number of substances for which the most common path to abuse begins with a prescription.

In Chapter 4, I proved that solutions to the SIAD model are non-negative and exist for all non-negative time. I also proved that both models have unique solutions. For the SIAD model, I found a condition for which the positive steady state is asymptotically stable. I used the $\mathfrak{R}_0$ value to determine when an epidemic could occur. The work presented in this chapter strengthens the results from Chapter 3 by showing the biological relevance. The work in this chapter presents the first rigorous mathematical analysis of the Vicodin abuse models.

In Chapter 6, I presented a novel use for the FLAG hydrocode by demonstrating its ability to model impact cratering. My results in FLAG matched well with

both theoretical and experimental results, with agreement considerably better than previously published results testing hydrocodes commonly used for impact cratering problems. The work in this chapter verifies and validates FLAG for impact cratering and provides information on expected errors in crater dimensions and maximum pressures based on mesh resolution and problem set up. FLAG's success for these V&V problems indicates FLAG can be an additional tool for impact cratering problems.

In Chapter 7, I used 2D and 3D FLAG simulations of the formation of the largest impact crater on Asteroid 16 Psyche to determine its likely material composition and porosity. This novel method for predicting material properties of Psyche corroborated other predictions in the literature that indicate Psyche is likely composed of a large portion of metallic content and is porous. My models also indicated that the impact angle that formed the crater was likely at least 45° from vertical, possibly 60° or greater. The models confirmed that hardening behavior and damage played a role in the crater's formation.

## 8.1 Ongoing and Future Work

The SIAD model for Vicodin abuse is being modified to include an undesirable exit from abuse, either from overdose death or as a gateway effect to another substance. This modified model will explore the interesting dynamics of a system in which the goal is to reduce the population in one compartment in a favorable manner rather than through death or another substance. This work will be the subject of an undergraduate honors thesis project.

I have combined the CVT and SIAD Vicodin abuse models into one model, the Multiple Relapse Vicodin Abuse (MRVA) model, for which the CVT and SIAD models are special cases. For the MRVA model, I am working on the same type of analysis presented in Chapter4.

I am currently working on validating FLAG for explosion cratering and comparing these results to results from the HOSS code, a code used strictly for modeling solid materials. The validation will evaluate how FLAG's solid material modeling compares to that of a code developed for geologic applications. This work will also test FLAG's capability to model geologic materials and help to determine if different material models should be implemented in FLAG for terrestrial cratering problems.

I am modeling the smaller of Psyche's two largest impact craters, beginning with 2D scoping runs as I did for the larger crater in Chapter 7. When the scoping runs are complete, I plan to model the crater formation in 3D using the same shape model that I used for the larger crater. I will also vary the angle of impact and materials if the 2D scoping runs indicate that is necessary.

[1] Abel, N. H., *Mémoire sur les équations algébrique: où on démontre l'impossiblité de la résolution de l'equation générale du cinquième dégré* (Grøndahl & Søn, 1824).

[2] Accuratus Ceramic Corporation, "Fused Silica Material Properties", URL `https://www.accuratus.com/pdf/SiO2props.pdf` (2018).

[3] A'Hearn, M. F., M. Belton, W. Delamere, J. Kissel, K. Klaasen, L. McFadden, K. Meech, H. Melosh, P. Schultz, J. Sunshine *et al.*, "Deep Impact: Excavating Comet Tempel 1", Science (2005).

[4] Ahrens, T. J. and A. W. Harris, "Deflection and fragmentation of near-Earth asteroids", Nature **360**, 6403, 429 (1992).

[5] Aida, T., J. W. Walter, T. D. Aslam and M. Short, "Verification of 2-D Detonation Shock Dynamics in conjunction with Los Alamos Lagrangian hydrocode", Tech. rep., Los Alamos National Laboratory, lA-UR-12-20792 (2013).

[6] Amsden, A., H. Ruppel and C. Hirt, "SALE: A Simplified ALE Computer Program for Fluid Flow at All Speeds", Tech. rep., Los Alamos Scientific Lab. (1980).

[7] Anderson Jr., C. E., "An overview of the theory of hydrocodes", International Journal of Impact Engineering **5**, 1-4, 33–59 (1987).

[8] Artalejo, J. R., A. Economou and M. J. Lopez-Herrero, "The stochastic SEIR model before extinction: Computational approaches", Applied Mathematics and Computation **265**, 1026–1043 (2015).

[9] Asphaug, E. and A. Reufer, "Mercury and other iron-rich planetary bodies as relics of inefficient accretion", Nature Geoscience **7**, 8, 564–568 (2014).

[10] Autodyn, A., "Theory Manual Revision 4.3", Century Dynamics, Concord, CA (2005).

[11] Avila, J. and M. Murray, "Prescription Painkiller Use at Record High for Americans", ABC News Internet Ventures, `abcnews.go.com/US/prescription-painkillers-record-number-americans-pain-medication/print?id=13421828` (2011).

[12] Azzopardi, V., "Controlling Controlled Substances: The balance between proper pain management and preventing drug abuse", rxethics.org, `http://rxethics.org/Azzopardi%20Edited%20PDF.pdf` (2013).

[13] Bardak, B. and M. Tan, "Prediction of influenza outbreaks by integrating wikipedia article access logs and google flu trend data", in "Bioinformatics and Bioengineering (BIBE), 2015 IEEE 15th International Conference on", pp. 1–6 (IEEE, 2015).

[14] Belof, J. L., R. M. Cavallo, R. T. Olson, R. S. King, G. T. Gray III, D. Holtkamp, S.-R. Chen, R. E. Rudd, N. Barton, A. Arsenlis *et al.*, "Rayleigh-taylor strength experiments of the pressure-induced $\alpha$? $\varepsilon$? $\alpha$? phase transition in iron", in "AIP Conference Proceedings", vol. 1426, pp. 1521–1524 (AIP, 2012).

[15] Benson, D. J., "Computational methods in Lagrangian and Eulerian hydrocodes", Computer Methods in Applied Mechanics and Engineering **99**, 2-3, 235–394 (1992).

[16] Benz, W. and E. Asphaug, "Simulations of brittle solids using smooth particle hydrodynamics", Computer Physics Communications **87**, 1-2, 253–265 (1995).

[17] Birnbaum, N., M. Cowler, M. Itoh, M. Katayama and H. Obata, "Autodyn–an interactive non-linear dynamic analysis program for microcomputers through supercomputers", in "Transactions of the 9th international conference on structural mechanics in reactor technology. Vol. B", (1987).

[18] Black, W., N. Denissen and J. McFarland, "Evaporation Effects in Shock-Driven Multiphase Instabilities", Journal of Fluids Engineering **139**, 24, 071204 (2017).

[19] Boslough, M. and D. Crawford, "Low-altitude airbursts and the impact threat", International Journal of Impact Engineering **35**, 12, 1441–1448 (2008).

[20] Bradley, A. M., "PDE-constrained optimization and the adjoint method", Stanford University, `https://cs.stanford.edu/~ambrad/adjoint_tutorial.pdf` (2010).

[21] Brauer, F. and C. Castillo-Chavez, *Mathematical Models in Population Biology and Epidemiology* (Springer, 2012), 2 edn.

[22] Brewer, C., "What to Know About Finding Rehab for Hydrocodone Addiction", Rehabs.com, Recover Brands LLC, `http://www.rehabs.com/about/hydrocodone-rehab` (2013).

[23] Burchell, M. J. and E. Johnson, "Impact craters on small icy bodies such as icy satellites and comet nuclei", Monthly Notices of the Royal Astronomical Society **360**, 2, 769–781 (2005).

[24] Burton, D., "Connectivity Structures and Differencing Techniques for Staggered-Grid Free-Lagrange Hydroynamics", Tech. Rep. UCRL-JC-110555, Lawrence Livermore National Laboratory, Livermore, CA (1992).

[25] Burton, D., "Consistent Finite-Volume Discretization of Hydrodynamic Conservation Laws for Unstructured Grids", Tech. Rep. UCRL-JC-118788, Lawrence Livermore National Laboratory, Livermore, CA (1994).

[26] Burton, D., "Multidimensional Discretization of Conservation Laws for Unstructured Polyhedral Grids", Tech. Rep. UCRL-JC-118306, Lawrence Livermore National Laboratory, Livermore, CA (1994).

[27] Burton, D., N. Morgan, M. Charest, M. Kenamond and J. Fung, "Compatible, energy conserving, bounds preserving remap of hydrodynamic fields for an extended ALE scheme", Journal of Computational Physics **355**, 492–533 (2018).

[28] Byrnside, N. C. and P. J. Torvik, "The effect of projectile strength on crater formation", Tech. Rep. AFML-TR-70-309, Air Force Institute of Technology, Wright-Patterson Air Force Base, Ohio (1971).

[29] Caldwell, W. K., B. Freedman, L. Settles, M. M. Thomas, E. T. Camacho *et al.*, "The Vicodin Abuse Problem: A Mathematical Approach", In Revision at Journal of Theoretical Biology (2018).

[30] Caldwell, W. K., A. Hunter, C. S. Plesko and S. Wirkus, "Verification and Validation of the FLAG Hydrocode for Impact Cratering Simulations", Journal of Verification, Validation and Uncertainty Quantification (2018).

[31] Camacho, E. T., M. A. C. Vélez, D. J. Hernández, U. R. Bernier, J. Van Laarhoven and S. Wirkus, "A mathematical model for photoreceptor interactions", Journal of theoretical biology **267**, 4, 638–646 (2010).

[32] Cao, Y., S. Li, L. Petzold and R. Serban, "Adjoint Sensitivity Analysis for Differential-Algebraic Equations: The Adjoint DAE System and Its Numerical Solution", SIAM Journal on Scientific Computing **24**, 3, 1076–1089 (2003).

[33] Centers for Disease Control and Prevention, "Vital signs: overdoses of prescription opioid pain relievers—United States, 1999–2008.", Morbidity and Mortality Weekly Report **60**, 43, 1487 (2011).

[34] Centers for Disease Control and Prevention, "Policy Impact: Prescription Painkiller Overdoses", Centers for Disease Control and Prevention (2011).

[35] Collins, G. S., "An Introduction to Hydrocode Modeling", Applied Modelling and Computation Group, Imperial College London pp. 2–11 (2002).

[36] Colon-Rentas, O., L. Gordon, L. D. Montejo, P. Reitsma, F. A. Sánchez *et al.*, "The Impacts of the Sleeper Effect and Relapse on the Dynamics of Cigarette Smoking Among Adolescents", Tech. Rep. MTBI-03-04M, Mathematical and Theoretical Biology Institute (2006).

[37] Comer, S. D. and J. B. Ashworth, "The Growth of Prescription Opioid Abuse", Pain and Chemical Dependency **18**, 19 (2008).

[38] Compton, W. M. and N. D. Volkow, "Major increases in opioid analgesic abuse in the United States: Concerns and strategies", Drug and Alcohol Dependence **81**, 2, 103–107 (2006).

[39] Cooley, J., R. Olson and D. Oro, "Modeling and analysis of high-explosive driven perturbed plate experiments at Los Alamos", Journal of Physics: Conference Series **500**, 152003 (2014).

[40] Crook, S. M., G. B. Ermentrout, M. C. Vanier and J. M. Bower, "The Role of Axonal Delay in the Synchronization of Networks of Coupled Cortical Oscillators", Journal of computational neuroscience **4**, 2, 161–172 (1997).

[41] Daugherty, D., T. Roque-Urrea, J. Urrea-Roque, J. Troyer, S. Wirkus and M. A. Porter, "Mathematical models of bipolar disorder", Communications in Nonlinear Science and Numerical Simulation **14**, 7, 2897–2908 (2009).

[42] Diversion Control Division, "Schedules of Controlled Substances: Rescheduling of Hydrocodone Combination Products From Schedule III to Schedule II", Docket No. DEA-389 (2014).

[43] DrugAbuse.com, "Vicodin abuse signs", DrugAbuse.com, Recovery Brands LLC, `http://drugabuse.com/library/vicodin-abuse` (2013).

[44] Edlund, M. J., B. C. Martin, M.-Y. Fan, A. Devries, J. B. Braden *et al.*, "Risks for opioid abuse and dependence among recipients of chronic opioid therapy: Results from the TROUP study", Drug and Alcohol Dependence **112**, 1, 90–98 (2010).

[45] Elkins-Tanton, L., E. Asphaug, J. Bell, D. Bercovici, B. Bills, R. Binzel, W. Bottke, I. Jun, S. Marchi, D. Oh *et al.*, "Journey to a metal world: concept for a discovery mission to Psyche", in "Lunar and Planetary Science Conference", vol. 45, p. 1253 (2014).

[46] Eymard, R., T. Gallouët and R. Herbin, "Finite Volume Methods", Handbook of Numerical Analysis **7**, 713–1018 (2000).

[47] Farinella, P. and D. R. Davis, "Collision Rates and Impact Velocities in the Main Asteroid Belt", Icarus **97**, 1, 111–123 (1992).

[48] Fishbain, D. A., B. Cole, J. Lewis, H. L. Rosomoff and R. S. Rosomoff, "What Percentage of Chronic Nonmalignant Pain Patients Exposed to Chronic Opioid Analgesic Therapy Develop Abuse/Addiction and/or Aberrant Drug-Related Behaviors? A Structured Evidence-Based Review", Pain Medicine **9**, 4, 444–459 (2008).

[49] Fugate, M., D. Higdon, B. Williams, K. M. Hanson, T. Wallstrom, W. Blumenthal and S.-R. Chen, "Calibration of the Preston-Tonks-Wallace (PTW) Plastic Deformation Model: Fiscal Year 2008", Tech. Rep. LA-UR-08-5866, Los Alamos National Laboratory, Los Alamos, NM (2008).

[50] Fung, J., A. K. Harrison, S. Chitanvis and J. Margulies, "Ejecta source and transport modeling in the FLAG hydrocode", Computers & Fluids **83**, 177–186 (2013).

[51] Generous, N., G. Fairchild, A. Deshpande, S. Y. Del Valle and R. Priedhorsky, "Global disease monitoring and forecasting with wikipedia", PLoS Comput Biol **10**, 11, e1003892 (2014).

[52] Getz, W. M. and J. O. Lloyd-Smith, "Basic Methods for Modeling the Invasion and Spread of Contagious Diseases", in "Disease Evolution: Models, Concepts, and Data Analyses", pp. 87–112 (Citeseer, 2006).

[53] Gittings, M., R. Weaver, M. Clover, T. Betlach, N. Byrne, R. Coker, E. Dendy, R. Hueckstaedt, K. New, W. R. Oakes *et al.*, "The RAGE radiation-hydrodynamic code", Computational Science & Discovery **1**, 1, 015005 (2008).

[54] Granzier, H. L. and S. Labeit, "The Giant Muscle Protein Titin is an Adjustable Molecular Spring", Exercise and Sport Sciences Reviews **34**, 2, 50–53 (2006).

[55] Gustafson, P., C. Srinivasan and L. Wasserman, "Local Sensitivity Analysis", Bayesian statistics **5**, 197–210 (1996).

[56] Hartmann, W. K. and G. Neukum, "Cratering Chronology and the Evolution of Mars", in "Chronology and Evolution of Mars", pp. 165–194 (Springer, 2001).

[57] Hayes, J. C., M. L. Norman, R. A. Fiedler, J. O. Bordner, P. S. Li, S. E. Clark, M.-M. Mac Low *et al.*, "Simulating Radiating and Magnetized Flows in Multiple Dimensions with ZEUS-MP", The Astrophysical Journal Supplement Series **165**, 1, 188 (2006).

[58] Hayne, P. O., B. T. Greenhagen, M. C. Foote, M. A. Siegler, A. R. Vasavada and D. A. Paige, "Diviner Lunar Radiometer Observations of the LCROSS Impact", Science **330**, 6003, 477–479 (2010).

[59] Hethcote, H. W., "The Mathematics of Infectious Diseases", SIAM review **42**, 4, 599–653 (2000).

[60] Hickmann, K. S., G. Fairchild, R. Priedhorsky, N. Generous, J. M. Hyman, A. Deshpande and S. Y. Del Valle, "Forecasting the 2013–2014 influenza season using wikipedia", PLoS Comput Biol **11**, 5, e1004239 (2015).

[61] Hill, J. L., *User's Manual for FLAG version 3.6.0*, The Lagrangian Applications Project, Los Alamos National Laboratory, LA-CP-17-20057 (2017).

[62] Hirose, K., G. Morard, R. Sinmyo, K. Umemoto, J. Hernlund, G. Helffrich and S. Labrosse, "Crystallization of silicon dioxide and compositional evolution of the Earth?s core", Nature **543**, 7643, 99 (2017).

[63] Hodgkin, A. L. and A. F. Huxley, "Currents carried by sodium and potassium ions through the membrane of the giant axon of Loligo", The Journal of physiology **116**, 4, 449–472 (1952).

[64] Holsapple, K., "The Scaling of Impact Processes in Planetary Sciences", Annual Review of Earth and Planetary Sciences **21**, 1, 333–373 (1993).

[65] Holsapple, K. A., "Impact and Explosion Effects", URL `http://keith.aa.washington.edu/craterdata/scaling/index.htm` (2018).

[66] Housen, K. R. and K. A. Holsapple, "Ejecta from impact craters", Icarus **211**, 1, 856–875 (2011).

[67] IMS Institute for Healthcare Informatics, "The Use of Medicine in the United States: Review of 2010", IMS Institute for Healthcare Informatics p. 33 (2011).

[68] Ivanov, B., D. Deniem and G. Neukum, "Implementation of dynamic strength models into 2D hydrocodes: Applications for atmospheric breakup and impact cratering", International Journal of Impact Engineering **20**, 1-5, 411–430 (1997).

[69] Jet Propulsion Laboratory, "Mission to a Metal World psyche", URL `https://www.jpl.nasa.gov/missions/psyche/` (2018).

[70] Jet Propulsion Laboratory, "Psyche shape model", URL `https://echo.jpl.nasa.gov/asteroids/shapes/shapes.html` (2018).

[71] Johhson, G. R. and W. H. Cook, "A Constitutive Model and Data for Metals Subjected to Large Strains, High Strain Rates and High Temperatures", in "Proceedings Seventh International Symposium on Ballistics", pp. 541–547 (The Hague, The Netherlands, 1983).

[72] Kaasalainen, M. and J. Torppa, "Optimization Methods for Asteroid Lightcurve Inversion: I. Shape Determination", Icarus **153**, 1, 24–36 (2001).

[73] Kermack, W. O. and A. G. McKendrick, "A Contribution to the Mathematical Theory of Epidemics", Proceedings of the Royal Society **115A**, 5, 700–721 (1927).

[74] Kochetova, O., "Application of New Criteria for the Selection of Perturbed Minor Planets to the Determination of the Masses of Perturbing Minor Planets by the Dynamical Method", Soobshch. In-ta Prikladnoi Astronomii RAN , 165, 42 (2003).

[75] Korycansky, D., C. S. Plesko, M. Jutzi, E. Asphaug and A. Colaprete, "Predictions for the LCROSS mission", Meteoritics & Planetary Science **44**, 4, 603–620 (2009).

[76] Lahrouz, A., L. Omari, D. Kiouach and A. Belmaâti, "Deterministic and stochastic stability of a mathematical model of smoking", Statistics & Probability Letters **81**, 8, 1276–1284 (2011).

[77] Lee, S., E. Jung and C. Castillo-Chavez, "Optimal control intervention strategies in low- and high-risk problem drinking populations", Socio-Economic Planning Sciences **44**, 4, 258–265 (2010).

[78] Li, M. Y. and J. S. Muldowney, "Global Stability for the SEIR Model in Epidemiology", Mathematical Biosciences **125**, 2, 155–164 (1995).

[79] Lindelöf, E., "Sur l'application de la méthode des approximations successives aux équations différentielles ordinaires du premier ordre", Comptes rendus hebdomadaires des séances de l?Académie des sciences **116**, 3, 454–457 (1894).

[80] Lodders, K. and B. Fegley Jr, "An Oxygen Isotope Model for the Composition of Mars", Icarus **126**, 2, 373–394 (1997).

[81] Los Alamos National Laboratory, "Trinity to Trinity", URL `http://www.lanl.gov/about/history-innovation/trinity-to-trinity/index.php` (2017).

[82] Lupishko, D., "On the Bulk Density of the M-type Asteroid 16 Psyche", Solar System Research **40**, 3, 214–218 (2006).

[83] Lyon, S. P. and J. D. Johnson, "SESAME: The Los Alamos National Laboratory Equation of State Database", Tech. rep., Los Alamos National Laboratory, LA-UR-92-3407 (1992).

[84] Mack, A. H. and R. J. Frances, "Substance-Related Disorders", FOCUS: The Journal of Lifelong Learning in Psychiatry **1**, 2, 125–146 (2003).

[85] Mackun, P. and S. Wilson, "Population Distribution and Change: 2000 to 2010", Tech. Rep. C2010BR-01, United States Census Bureau (2011).

[86] Manchikanti, L., "National Drug Control Policy and Prescription Drug Abuse: Facts and Fallacies", Pain Physician **10**, 3, 399 (2007).

[87] Margolin, L., "A centered artificial viscosity for cells with large aspect ratio", NASA STI/Recon Technical Report N **89** (1988).

[88] Marino, S., I. B. Hogue, C. J. Ray and D. E. Kirschner, "A methodology for performing global uncertainty and sensitivity analysis in systems biology", Journal of Theoretical Biology **254**, 1, 178–196 (2008).

[89] Marzari, F. and S. J. Weidenschilling, "Eccentric Extrasolar Planets: The Jumping Jupiter Model", Icarus **156**, 2, 570–579 (2002).

[90] Matter, A., M. Delbo, B. Carry and S. Ligori, "Evidence of a metal-rich surface for the Asteroid (16) Psyche from interferometric observations in the thermal infrared", Icarus **226**, 1, 419–427 (2013).

[91] McCabe, S. E., J. A. Cranford, C. J. Boyd and C. J. Teter, "Motives, diversion and routes of administration associated with nonmedical use of prescription opioids", Addictive Behaviors **32**, 3, 562–575 (2007).

[92] McGlaun, J. M., S. Thompson and M. Elrick, "CTH: a three-dimensional shock wave physics code", International Journal of Impact Engineering **10**, 1-4, 351–360 (1990).

[93] Mechcatie, E., "Advisory Panel Backs Withdrawal of Vicodin", Rheumatology News **8**, 8, 12–12 (2009).

[94] Melosh, H. J., "Impact cratering: A geologic process", Oxford University Press (Oxford Monographs on Geology and Geophysics, No. 11), 1989, 253 p. **11** (1989).

[95] Melosh, H. J., *Planetary Surface Processes*, vol. 13 (Cambridge University Press, 2011).

[96] Meyers, M. A., *Dynamic Behavior of Materials* (John Wiley & Sons, 1994).

[97] Michael's House, "How Vicodin Addiction Starts–And What You Can Do to Prevent It", Michael's House Treatment Centers, `https://www.michaelshouse.com/featured-articles/how-vicodin-addiction-starts` (2013).

[98] Michael's House, "Hydrocodone Rehab", Michael's House Treatment Centers, `www.michaelshouse.com/featured-articles/hydrocodone-rehab` (2013).

[99] Michael's House, "Vicodin Rehab Statistics", Michael's House Treatment Centers, `http://www.michaelshouse.com/vicodin-rehab/real-statistics` (2013).

[100] Moon, B. S., H. S. Kim and S. I. Hong, "Plastic flow and deformation homogeneity of 6061 Al during equal channel angular pressing", Scripta Materialia **46**, 2, 131–136 (2002).

[101] Mulone, G. and B. Straughan, "Modeling binge drinking", International Journal of Biomathematics **5**, 01, 1250005 (2012).

[102] Murray, J. D., *Mathematical Biology I: An Introduction* (Interdisciplinary Applied Mathematics, New York, Springer, 2002), 3 edn.

[103] National Center for Injury Prevention and Control, "Unintentional Drug Poisoning in the United States", Centers for Disease Control and Prevention (2010).

[104] Nolan, M. C., E. Asphaug, H. J. Melosh and R. Greenberg, "Impact Craters on Asteroids: Does Gravity or Strength Control Their Size?", Icarus **124**, 2, 359–371 (1996).

[105] Oh, D. Y., D. M. Goebel, L. Elkins-Tanton, C. Polanskey, P. Lord, S. Tilley, J. S. Snyder, G. Carr, S. Collins, G. Lantoine *et al.*, "Psyche: Journey to a Metal World", in "52nd AIAA/SAE/ASEE Joint Propulsion Conference", p. 4541 (2016).

[106] O'Neill, S., "Kaiser program leads to huge reduction in Vicodin and Oxycontin prescriptions", Southern California Public Radio, `http://www.scpr.org/news/2013/04/22/36881/kaiser-program-leads-to-huge-reduction-in-vicodin` (2013).

[107] Paulozzi, L., G. Baldwin, G. Franklin, G. Kerlikowske, C. M. Jones, N. Ghiya and T. Popovic, "CDC Grand Rounds: Prescription Drug Overdoses – a U.S. Epidemic", Morbidity and Mortality Weekly Report **61**, 1, 10–13 (2012).

[108] Perelson, A. S., A. U. Neumann, M. Markowitz, J. M. Leonard, D. D. Ho *et al.*, "Hiv-1 dynamics in vivo: virion clearance rate, infected cell life-span, and viral generation time", Science **271**, 5255, 1582–1586 (1996).

[109] Perko, L., *Differential Equations and Dynamical Systems*, vol. 7 (Springer Science & Business Media, 2013).

[110] Pierazzo, E., N. Artemieva, E. Asphaug, E. Baldwin, J. Cazamias, R. Coker, G. Collins, D. Crawford, T. Davison, D. Elbeshausen *et al.*, "Validation of numerical codes for impact and explosion cratering: Impacts on strengthless and metal targets", Meteoritics & Planetary Science **43**, 12, 1917–1938 (2008).

[111] Plesko, C. S., *Automated feature detection and hydrocode modeling of impact-related structures on Mars* (University of California, Santa Cruz, 2009).

[112] Polgreen, P. M., Y. Chen, D. M. Pennock, F. D. Nelson and R. A. Weinstein, "Using internet searches for influenza surveillance", Clinical infectious diseases **47**, 11, 1443–1448 (2008).

[113] PrescriptionDrugAbuse.org, "Effects of vicodin abuse", PrescriptionDrugAbuse.org, `https://www.prescriptiondrugabuse.org/Effects-of-Vicodin-Abuse.htm` (2013).

[114] Preston, D. L., "PTW Mod 1", Tech. Rep. LA-UR-10-06436, Los Alamos National Laboratory (2010).

[115] Preston, D. L., D. L. Tonks and D. C. Wallace, "Model of plastic deformation for extreme loading conditions", Journal of Applied Physics **93**, 1, 211–220 (2003).

[116] Priedhorsky, R., D. Osthus, A. R. Daughton, K. R. Moran, N. Generous, G. Fairchild, A. Deshpande and S. Y. Del Valle, "Measuring global disease with wikipedia: Success, failure, and a research agenda", in "Proceedings of the 2017 ACM Conference on Computer Supported Cooperative Work and Social Computing", pp. 1812–1834 (ACM, 2017).

[117] Riller, U., "Structural characteristics of the Sudbury impact structure, Canada: Impact-induced versus orogenic deformation?A review", Meteoritics & Planetary Science **40**, 11, 1723–1740 (2005).

[118] Sánchez, F., X. Wang, C. Castillo-Chávez, D. M. Gorman and P. J. Gruenewald, "Drinking as an Epidemic–A Simple Mathematical Model with Recovery and Relapse", Therapist's Guide to Evidence-Based Relapse Prevention p. 353 (2007).

[119] Schultz, P. H., C. A. Eberhardy, C. M. Ernst, M. F. A'Hearn, J. M. Sunshine and C. M. Lisse, "The Deep mpact oblique impact cratering experiment", Icarus **191**, 2, 84–122 (2007).

[120] Schultz, P. H., C. M. Ernst and J. L. B. Anderson, "Expectations for crater size and photometric evolution from the deep impact collision", Space Science Reviews **117**, 1-2, 207–239 (2005).

[121] Scovel, C. A. and R. Menikoff, "A verification and validation effort for high explosives at Los Alamos National Lab", in "AIP Conference Proceedings", vol. 1195, pp. 169–172 (AIP, 2009).

[122] Shabana, A. A., *Computational Continuum Mechanics* (Cambridge University Press, 2008).

[123] Sharp, R., "Users Manual for ALE3D: An Arbitrary Lagrange/Eulerian 3D Code System", Lawrence Livermore National Laboratory (2005).

[124] Shepard, M. K., J. Richardson, P. A. Taylor, L. A. Rodriguez-Ford, A. Conrad, I. de Pater, M. Adamkovics, K. de Kleer, J. R. Males, K. M. Morzinski *et al.*, "Radar observations and shape model of asteroid 16 Psyche", Icarus **281**, 388–403 (2017).

[125] Shoemaker, E. M., "Penetration mechanics of high velocity meteorites, illustrated by Meteor Crater, Arizona", Meteorite Craters, Benchmark Papers in Geology p. 170 (1977).

[126] Shoemaker, L. E. and G. D. Smith, "A Century of Monel Metal: 1906–2006", JOM **58**, 9, 22–26 (2006).

[127] Shuvalov, V., "Multi-dimensional hydrodynamic code SOVA for interfacial flows: Application to the thermal layer effect", Shock Waves **9**, 6, 381–390 (1999).

[128] Simo, J. C. and T. J. R. Hughes, *Computational Inelasticity*, vol. 7 (Springer Science & Business Media, 2006).

[129] Smith, H. L., L. Wang and M. Y. Li, "Global Dynamics of an SEIR Epidemic Model with Vertical Transmission", SIAM Journal on Applied Mathematics **62**, 1, 58–69 (2001).

[130] Steinberg, D., S. Cochran and M. Guinan, "A constitutive model for metals applicable at high-strain rate", Journal of Applied Physics **51**, 3, 1498–1504 (1980).

[131] Steinberg, D. J., "Equation of State and Strength Properties of Selected Materials", Tech. Rep. UCRL-MA-106439, Lawrence Livermore National Laboratory, Livermore, CA (1996).

[132] Stickle, A., E. Rainey, M. B. Syal, J. Owen, P. Miller, O. Barnouin and C. Ernst, "Modeling impact outcomes for the Double Asteroid Redirection Test (DART) mission", Procedia Engineering **204**, 116–123 (2017).

[133] Substance Abuse and Mental Health Services Administration, "Results from the 2011 National Survey on Drug Use and Health: Summary of National Findings", NSDUH Series H-44, HHS Publication No. (SMA) 12-4713. Rockville, MD: Substance Abuse and Mental Health Services Administration (2012).

[134] Sullivan, M. D., M. J. Edlund, M.-Y. Fan, A. DeVries, B. Braden *et al.*, "Trends in use of opioids for non-cancer pain conditions 2000–2005 in commercial and Medicaid insurance plans: The TROUP study", Pain **138**, 2, 440–449 (2008).

[135] Surdej, J. and A. Surdej, "Asteroid Lightcurves Simulated by the Rotation of a Three-axes Ellipsoid Model", Astronomy and Astrophysics **66**, 31–36 (1978).

[136] Szalavitz, M., "FDA Action on Vicodin May Mean More Pain, Not Less Addiction or Overdose", TIME (2013).

[137] Thieme, H. R., *Mathematics in Population Biology* (Princeton University Press, 2003).

[138] Tobler, N. S. and H. H. Stratton, "Effectiveness of School-Based Drug Prevention Programs: A Meta-Analysis of the Research", Journal of Primary Prevention **18**, 1, 71–128 (1997).

[139] Tonks, D., D. Paisley, P. Peralta, S. Greenfield, D. Byler, S. Luo, D. Swift and A. Koskelo, "Spallation damage in copper with columnar grains", AIP Conference Proceedings **955**, 605–608 (2007).

[140] United States Drug Enforcement Administration, "Drug scheduling", United States Drug Enforcement Administration, `https://www.dea.gov/druginfo/ds.shtml` (2018).

[141] Viateau, B., "Mass and density of asteroids (16) Psyche and (121) Hermione", Astronomy and Astrophysics **354**, 725–731 (2000).

[142] Viken, R. J., T. A. Treat, R. M. Nosofsky, R. M. McFall and T. J. Palmeri, "Modeling Individual Differences in Perceptual and Attentional Processes Related to Bulimic Symptoms.", Journal of Abnormal Psychology **111**, 4, 598 (2002).

[143] Volkow, N. D., "Prescription Drugs: Abuse and Addiction", National Institute on Drug Abuse, U.S. Department of Health and Human Services, National Institutes of Health (2005).

[144] Volkow, N. D., T. A. McLellan, J. H. Cotto, M. Karithanom and S. R. B. Weiss, "Characteristics of opioid prescriptions in 2009", JAMA: The Journal of the American Medical Association **305**, 13, 1299–1301 (2011).

[145] White, E. and C. Comiskey, "Heroin epidemics, treatment and ODE modelling", Mathematical Biosciences **208**, 1, 312–324 (2007).

# APPENDIX A

# PERMISSION

Portions of Chapter 3 are included in the manuscript "The Vicodin Abuse Problem: A Mathematical Approach," which is in revision at *Journal of Theoretical Biology* as of April 4, 2019. This manuscript was co-authored by Benjamin Freedman, Luke Settles, Michael M. Thomas, Erika T. Camacho, and Stephen Wirkus.

Portions of Chapter 6 are included in the manuscript "Verification and Validation of the FLAG Hydrocode for Impact Cratering Simulations," which has been accepted at Journal of Verification, Validation and Uncertainty Quantification. This manuscript was co-authored by Abigail Hunter, Catherine S. Plesko, and Stephen Wirkus.

A manuscript containing the results presented in Chapter 7 in is preparation as of April 4, 2019. This manuscript is co-authored by Abigail Hunter, Catherine S. Plesko, and Stephen Wirkus.

I certify that I have obtained permission from all of my co-authors to include the content of these manuscripts in my dissertation.

Wendy K. Caldwell, April 4, 2019

# APPENDIX B

# ESTIMATION OF PARAMETER VALUES AND INITIAL CONDITIONS

## B.1 CVT Model Parameter Values

Using information concerning Vicodin use in the United States, I was able to establish estimated ranges for each of our parameters, listed in Table 3.1.

To estimate the number of people receiving new Vicodin prescriptions each month, I first considered the number of Vicodin prescriptions written each year, 131.2 million [67]. I assumed the same number of prescriptions each month and divide this number by 12, indicating 10.93333 million Vicodin prescriptions each month. I then determined the number of new prescriptions by multiplying by the percentage of new prescriptions, 43% [144]. Because the CVT model only considered initial prescriptions of three or fewer months, I divided by the average supply per person, which ranges from 42.7 days to 52.8 days [134]. Converting this average supply to months, assuming 30 days to be one month, led to an average supply of $1.42\bar{3}$ to 1.76 months. I used these supply ranges to find the upper and lower bounds for Lambda:

$$\begin{aligned}
\Lambda_{\text{lower}} &\approx \underbrace{\left(\frac{131.2 \text{ million}}{12}\right)}_{\text{monthly R}_\text{x}} \underbrace{(0.43)}_{\text{new R}_\text{x}} \left(\frac{1}{\underbrace{1.76}_{\text{average supply in months}}}\right) \\
\Lambda_{\text{lower}} &\approx 2.671212 \text{ million} \\
\Lambda_{\text{upper}} &\approx \underbrace{\left(\frac{131.2 \text{ million}}{12}\right)}_{\text{monthly R}_\text{x}} \underbrace{(0.43)}_{\text{new R}_\text{x}} \left(\frac{1}{\underbrace{1.42\bar{3}}_{\text{average supply in months}}}\right) \\
\Lambda_{\text{upper}} &\approx 3.404044 \text{ million.}
\end{aligned}$$

This led to the estimated range for $\Lambda$: $[2671212, 3404044]$.

I estimated the rate at which acute medical users become chronic users ($\alpha_1$) and the rate at which acute medical users stop using Vicodin ($\alpha_2$) by considering the average time for acute medical use (less than or equal to three months). For the model, this is the average time an individual is in the $M$ compartment, $\frac{1}{\alpha_1+\alpha_2}$. Thus, $1 \leq \frac{1}{\alpha_1+\alpha_2} \leq 3$, which is equivalent to

$$\frac{1}{3} \leq \alpha_1 + \alpha_2 \leq 1. \tag{B.1}$$

To further determine this value, I considered multiple studies that estimate the average percentage of all opioid users with prescriptions for three or fewer months. This estimate is between 63.8% and 88.7% [134]. In the model, this percentage is $\frac{\alpha_2}{\alpha_1+\alpha_2}$. Equating these values led to the following inequality for $\alpha_2$:

$$\underbrace{0.638}_{\text{\% of acute users, lower bound}} \leq \underbrace{\frac{\alpha_2}{\alpha_1+\alpha_2}}_{\text{model \% of acute users}} \leq \underbrace{0.887}_{\text{\% of acute users, upper bound}}.$$

Considering each side of the inequality leads to the following bounds for $\alpha_2$:

$$\begin{aligned}
\alpha_{2\text{ lower}} : \alpha_2 &= 0.638\alpha_1 + 0.638\alpha_2 \\
0.362\alpha_2 &= 0.638\alpha_1 \\
\alpha_{2\text{ lower}} &\approx 1.762\alpha_1 \\
\alpha_{2\text{ upper}} : \alpha_2 &= 0.887\alpha_1 + 0.887\alpha_2 \\
0.113\alpha_2 &= 0.887\alpha_1 \\
\alpha_{2\text{ upper}} &\approx 7.850\alpha_1 \\
1.762\alpha_1 &\leq \alpha_2 \leq 7.850\alpha_1. \qquad \text{(B.2)}
\end{aligned}$$

I found an inequality for $\alpha_1$ by substituting the bounds for $\alpha_2$ from (B.2) into (B.1):

$$\begin{aligned}
\frac{1}{3} &\leq \alpha_1 + \alpha_2 \leq 1 \\
\frac{1}{3} - \alpha_2 &\leq \alpha_1 \leq 1 - \alpha_2.
\end{aligned}$$

Considering each side of the inequality leads to the following bounds for $\alpha_1$:

$$\begin{aligned}
\alpha_{1\text{ lower}} : \alpha_1 &= \frac{1}{3} - \underbrace{\alpha_2}_{\leq 7.850\alpha_1} \\
8.85\alpha_1 &= \frac{1}{3} \\
\alpha_{1\text{ lower}} &\approx 0.0377 \\
\alpha_{1\text{ upper}} : \alpha_1 &= 1 - \underbrace{\alpha_2}_{\geq 1.762\alpha_1} \\
2.762\alpha_1 &= 1 \\
\alpha_{1\text{ upper}} &\approx 0.362. \qquad \text{(B.3)}
\end{aligned}$$

This led to the estimated range for $\alpha_1$: $[0.0377, 0.362]$. Substituting these bounds into (B.1) and (B.2), I found the bounds for $\alpha_2$:

$$\begin{aligned}
\alpha_{2\text{ lower}} &= 1.762\alpha_1 \\
\alpha_{2\text{ lower}} &= 1.762 \underbrace{(0.0377)}_{\text{lower bound for } \alpha_1} \\
\alpha_{2\text{ lower}} &\approx 0.0664 \\
\alpha_{2\text{ upper}} &= 1 - \alpha_1 \\
\alpha_{2\text{ upper}} &= 1 - \underbrace{0.0377}_{\text{lower bound for } \alpha_1} \\
\alpha_{2\text{ upper}} &\approx 0.962.
\end{aligned}$$

These bounds led to the estimated range for $\alpha_2$: $[0.0664, 0.962]$.

To estimate the rate at which chronic users become abusers ($\delta$) and the rate at which chronic users cease Vicodin treatment ($\beta$), I began by considering the average

treatment time for chronic pain patients. It is important to note that for the purposes of these models, I considered chronic pain to be chronic non-cancer pain. The available data make this distinction. The average opioid exposure time for chronic pain patients is estimated between 10.8 and 26.2 months [48]. I subtracted the initial three months spent in the $M$ compartment, and I had the average time for chronic Vicodin use to be between 7.8 and 23.2 months. By model construction, the average time an individual is in the chronic use $(C_1, C_2)$ compartments is $\frac{2}{\delta+\beta}$. Combining these chronic use upper and lower bounds with the model average time for chronic use, I arrived at an inequality for $\beta$:

$$7.8 \leq \frac{2}{\delta+\beta} \leq 23.2,$$

where the left-hand side represents the lower bound of average number of months in chronic use from data [48], the right-hand side represents the upper bound of average number of months in chronic use from data [48], and the center term represents the model average number of months in chronic use. From this inequality, I found the bounds for $\beta$:

$$\begin{aligned} 3.9 \leq \quad & \tfrac{1}{\delta+\beta} & \leq 11.6 \\ 0.08621 \leq \quad & \delta+\beta & \leq 0.25641 \\ 0.08621-\delta \leq \quad & \beta & \leq 0.25641-\delta. \end{aligned} \tag{B.4}$$

To further solidify the bounds for $\delta$ and $\beta$, I considered the percentage of chronic opioid patients who become opioid abusers, which is estimated to be between 2.9% and 11.5% [44, 48]. Because the model assumes individuals in the $A$ compartment have passed through both the $C_1$ and $C_2$ compartments, I concluded $0.029 \leq \left(\frac{\delta}{\delta+\beta}\right)^2 \leq 0.115$. Using these bounds, I arrived at an inequality for $\delta$:

$$\underbrace{0.029}_{\text{\% of chronic users to abusers, lower}} \leq \underbrace{\left(\frac{\delta}{\delta+\beta}\right)^2}_{\text{model \% of chronic users to abusers}} \leq \underbrace{0.115}_{\text{\% of chronic users to abusers, upper}}$$

$$\begin{aligned} \sqrt{0.029} \quad & \leq \quad \frac{\delta}{\delta+\beta} \leq \sqrt{0.115} \\ \delta\sqrt{0.029}+\beta\sqrt{0.029} \quad & \leq \quad \delta \leq \delta\sqrt{0.115}+\beta\sqrt{0.115} \\ \frac{\beta\sqrt{0.029}}{1-\sqrt{0.029}-\sqrt{0.115}} \quad & \leq \quad \delta \leq \frac{\beta\sqrt{0.115}}{1-\sqrt{0.029}-\sqrt{0.115}}. \end{aligned}$$

Rounding down for the lower bound and rounding up for the upper bound, I concluded

$$0.347\beta \leq \delta \leq 0.692\beta. \tag{B.5}$$

Substituting the bounds for $\delta$ from (B.5) into the bounds for $\beta$ in (B.4), I found upper and lower bounds for $\beta$:

$$\begin{aligned}
\beta_{\text{lower}} : \beta &\approx 0.08621 - \underbrace{0.692\beta}_{\delta \text{ upper bound}} \\
\beta_{\text{lower}} &\approx \frac{0.08621}{1.692} \\
\beta_{\text{lower}} &\approx 0.051.
\end{aligned}$$

$$\begin{aligned}
\beta_{\text{upper}} : \beta &\approx 0.25641 - \underbrace{0.347\beta}_{\delta \text{ lower bound}} \\
\beta_{\text{upper}} &\approx \frac{0.25641}{1.347} \\
\beta_{\text{upper}} &\approx 0.190.
\end{aligned}$$

These bounds led to the estimated range for $\beta$: $[0.051, 0.190]$. Using these values with the $\delta$ bounds from (B.5), I found upper and lower bounds for $\delta$:

$$\begin{aligned}
\delta_{\text{lower}} &\approx 0.347 \underbrace{(0.051)}_{\beta \text{ lower bound}} \\
\delta_{\text{lower}} &\approx 0.0177 \\
\delta_{\text{upper}} &\approx 0.692 \underbrace{(0.190)}_{\beta \text{ upper bound}} \\
\delta_{\text{upper}} &\approx 0.131.
\end{aligned}$$

This result led to the estimated range for $\delta$: $[0.0177, 0.131]$.

I estimated the rate at which Vicodin abusers seek treatment ($\varepsilon$) by considering the average time in abuse before entering treatment. The average time a person remains an abuser before seeking treatment is estimated to be between 24 and 72 months [84]. Thus, $24 \leq \frac{1}{\varepsilon} \leq 72$. This produced the range of $\varepsilon$ to be $[0.014, 0.042]$.

I estimated the relapse rate ($\gamma_1$) successful treatment ($\gamma_2$) rates using data on treatment success as well as the duration of treatment, which I defined to last from 1 to 12 months. Thus, I concluded $1 \leq \frac{1}{\gamma_1+\gamma_2} \leq 12$. Equivalently,

$$\frac{1}{12} \leq \gamma_1 + \gamma_2 \leq 1. \tag{B.6}$$

The percentage of those in treatment who return to pre-treatment abuse levels within one year is estimated to be 45% [99]. I categorized the remaining 55% as having successfully completed treatment. In the model, this percentage is $\frac{\gamma_2}{\gamma_1+\gamma_2}$. Equating these two, I defined $\gamma_2$ in terms of $\gamma_1$:

$$\begin{aligned}
\underbrace{\frac{\gamma_2}{\gamma_1 + \gamma_2}}_{\text{model successful treatment \%}} &= \underbrace{0.55}_{\text{successful treatment \%}} \\
\gamma_2 &= 0.55\gamma_1 + 0.55\gamma_2 \\
0.45\gamma_2 &= 0.55\gamma_1 \\
\gamma_2 &= 1.\bar{2}\gamma_1.
\end{aligned} \tag{B.7}$$

Substituting the definition of (B.7) into (B.6), I found upper and lower bounds for $\gamma_1$:

$$\begin{aligned} \frac{1}{12} \leq \quad & \gamma_1 + \underbrace{1.\bar{2}\gamma_1}_{=\gamma_2} && \leq 1 \\ \frac{1}{12} \leq \quad & 2.\bar{2}\gamma_1 && \leq 1 \\ 0.0375 \leq \quad & \gamma_1 && \leq 0.45. \end{aligned}$$

This result led to the estimated range for $\gamma_1$: $[0.0375, 0.45]$.

To find the range for $\gamma_2$, I substituted the bounds for $\gamma_1$ into Equation (B.7):

$$\begin{aligned} \gamma_{2\text{lower}} &= 1.\bar{2}\gamma_1 \\ \gamma_{2\text{lower}} &= (1.\bar{2}) \quad \underbrace{(0.0375)}_{\text{lower bound for } \gamma_1} \\ \gamma_{2\text{lower}} &\approx 0.0458 \\ \gamma_{2\text{upper}} &= (1.\bar{2}) \quad \underbrace{(0.45)}_{\text{upper bound for } \gamma_1} \\ \gamma_{2\text{upper}} &= 0.55. \end{aligned}$$

This result led to the estimated range for $\gamma_2$: $[0.0458, 0.55]$.

## B.2 SIAD Model Parameter Values

The parameter values in the SIAD model take on the same values as in the CVT model, with two exceptions. In the SIAD model, the relapse parameter $\gamma_1$ has unit $\frac{1}{\text{month} \times \text{people}}$. Thus, I scaled the $\gamma_1$ range from the CVT model by the total model population at initial time, 49.7 million people, to obtain the range for the SIAD model:

$$\begin{aligned} \underbrace{(0.0375)}_{\text{CVT lower bound}} \left( \frac{1}{\underbrace{49.7 \text{ million}}_{\text{initial model population}}} \right) \leq \quad & \gamma_1 \quad \leq \underbrace{(0.45)}_{\text{CVT upper bound}} \left( \frac{1}{\underbrace{49.7 \text{ million}}_{\text{initial model population}}} \right) \\ 7.545 \times 10^{-10} \leq \quad & \gamma_1 \quad \leq 9.054 \times 10^{-9}. \end{aligned}$$

This led to the estimated range for $\gamma_1$: $[7.545 \times 10^{-10}, 9.054 \times 10^{-9}]$.

To find the range of $\rho$, we consider studies that indicate how prescribers respond when they suspect prescription drug abuse. In the study with the greatest reduction in new prescriptions, Vicodin prescriptions dropped by 95% when prescribers were educated on the risks over a two-year period [106]. I used this value to determine the

upper bound for $\rho$:

$$\rho_{\text{upper}}: \quad \underbrace{\frac{\Lambda}{1+\rho A}}_{\text{monthly new prescriptions with } \rho \neq 0} = \underbrace{0.05\Lambda}_{\text{monthly new prescriptions with } \rho = 0}$$

$$\begin{aligned}
\frac{\Lambda}{0.05\Lambda} &= 1+\rho A \\
20 &= 1+\rho A \\
19 &= \rho A \\
\rho &= \frac{19}{\underbrace{A}_{\text{initial value = 2 million}}} \\
\rho_{\text{upper}} &= 9.5 \times 10^{-6}.
\end{aligned}$$

I set the lower bound to be 0 to accommodate the case of a constant new prescription rate, which led to the estimated range for $\rho$: $[0, 9.5 \times 10^{-6}]$.

### B.3 Initial Conditions

About 47 million patients receive prescriptions for drugs containing hydrocodone each year [136]. Thus, $M + C_1 + C_2 \approx 47$ million. About nine million people report long-term medical use of opioids [107]. Thus, $C_1 + C_2 \approx 9$ million. There are approximately two million Vicodin abusers in the United States [43], so $A \approx 2$ million. Data sources suggest the percentage of opioid users in acute medical use could be as high as 86.6%–88.7% or could have a more conservative representation from 63.8%–72.2% [134]. For the initial population of acute medical users, I considered 80% of the total 47 million, 37.6 million. This leaves a total of 9.4 million between the two chronic compartments, which is consistent with data source estimates of approximately nine million. I divided this population into the two chronic compartments, placing 60% (5.64 million) in $C_1$ and 40% (3.76 million) in $C_2$. Initially, there are two million people in the $A$ compartment. Finally, for treatment, the most recent available data suggest 726,000 people in treatment for all pain relievers [133]. Because this includes all pain relievers (not only Vicodin), and because this number is lower than the previous year's, I began the simulations with 700,000 people in the $T$ compartment.

# APPENDIX C

# SENSITIVITES OF TREATMENT PARAMETERS IN THE SIAD MODEL

Recall Equation (4.15):

$$\rho\varepsilon\gamma_2\left(\alpha_1+\alpha_2\right)\left(\delta+\beta\right)^2A^{*2}+\left[\varepsilon\gamma_2\left(\alpha_1+\alpha_2\right)\left(\delta+\beta\right)^2-\gamma_1\alpha_2\delta^2\Lambda\right]A^*-\alpha_1\delta^2\gamma_2\Lambda=0.$$

To further explore the sensitivities of the treatment parameters $\gamma_1$ and $\gamma_2$, I find the partial derivative of $A^*$ with respect to both $\gamma_1$ and $\gamma_2$ separately. Define

$$\begin{aligned}
W_1 &:= \rho\varepsilon\left(\alpha_1+\alpha_2\right)\left(\delta+\beta\right)^2\\
W_2 &:= \varepsilon\left(\alpha_1+\alpha_2\right)\left(\delta+\beta\right)^2\\
W_3 &:= -\gamma_1\alpha_2\delta^2\Lambda\\
W_4 &:= -\alpha_1\delta^2\Lambda\ ,
\end{aligned}$$

so that

$$W_1\gamma_2A^{*2}+\left(W_2\gamma_2+W_3\right)A^*+W_4\gamma_2=0. \tag{C.1}$$

Using implicit differentation by taking $\frac{\partial}{\partial\gamma_2}$ of both sides:

$$\begin{aligned}
W_1A^{*2}+W_1\gamma_2\cdot 2A^*\frac{\partial A^*}{\partial\gamma_2}+W_2A^*+W_2\gamma_2\frac{\partial A^*}{\partial\gamma_2}+W_3\frac{\partial A^*}{\partial\gamma_2}+W_4&=0\\
\frac{\partial A^*}{\partial\gamma_2}\left(2AW_1\gamma_2+W_2\gamma_2+W_3\right)&=-W_1A^{*2}-W_2A^*-W_4\\
\frac{\partial A^*}{\partial\gamma_2}&=\frac{-W_1A^{*2}-W_2A^*-W_4}{2AW_1\gamma_2+W_2\gamma_2+W_3}\\
\frac{\gamma_2}{A^*}\frac{\partial A^*}{\partial\gamma_2}&=\frac{-W_1\gamma_2A^{*2}-W_2\gamma_2A^*-W_4\gamma_2}{2A^{*2}W_1\gamma_2+W_2\gamma_2A^*+W_3A^*}\\
&=\frac{-W_3}{2A^*W_1\gamma_2+W_2\gamma_2+W_3}\ \text{from Equation (C.1)}\ .
\end{aligned}$$

Solving Equation (4.15), $A^*|_{\gamma_2=0.293}\approx 999997.719837$. Varying over the $\gamma_2$ values in the plots gives numbers approximately:

$$\left.\frac{\gamma_2}{A^*}\frac{\partial A^*}{\partial\gamma_2}\right|_{\gamma_2=0.293}\approx -4.23323415779\times10^{-9}\ .$$

Now consider the sensitivity with respect to $\gamma_1$. Define

$$\begin{aligned}
K_1 &:= \rho\varepsilon\gamma_2\left(\alpha_1+\alpha_2\right)\left(\delta+\beta\right)^2\\
K_2 &:= \varepsilon\gamma_2\left(\alpha_1+\alpha_2\right)\left(\delta+\beta\right)^2\\
K_3 &:= \alpha_2\delta^2\Lambda\\
K_4 &:= \alpha_1\delta^2\gamma_2\Lambda\ ,
\end{aligned}$$

so that

$$K_1A^{*2}+\left[K_2-\gamma_1K_3\right]A^*-K_4=0\ .$$

Using implicit differentiation by taking $\frac{\partial}{\partial \gamma_1}$ of both sides:

$$K_1 \cdot 2A^* \frac{\partial A^*}{\partial \gamma_1} + K_2 \frac{\partial A^*}{\partial \gamma_1} - \left( K_3 A^* + \gamma_1 K_3 \frac{\partial A^*}{\partial \gamma_1} \right) = 0$$

$$\frac{\partial A^*}{\partial \gamma_1} = \frac{K_3 A^*}{2A^* K_1 + K_2 - \gamma_1 K_3}$$

$$\frac{\gamma_1}{A^*} \frac{\partial A^*}{\partial \gamma_1} = \frac{K_3 \gamma_1}{2K_1 A^* + K_2 - \gamma_1 K_3} \ .$$

Substituting the value for $A^*$ and varying over the $\gamma_1$ values in the plots give numbers approximately:

$$\left. \frac{\gamma_1}{A^*} \frac{\partial A^*}{\partial \gamma_1} \right|_{\gamma_1 = 8e-10} \approx 4.2332413575 \times 10^{-9} \ .$$

These low sensitivities indicate why the treatment parameters appear to have sensitivities of 0.

# APPENDIX D

# $A^*$ DEFINED IN TERMS OF PARAMETER VALUES

$$E^* = (M^*, C_1^*, C_2^*, A^*, T^*)$$

$$M^* = \frac{\Lambda\left(\alpha_1+\alpha_2\right)^{-1}}{\left(1+\left[\frac{-[\varepsilon\gamma_2(\alpha_1+\alpha_2)(\delta+\beta)^2-\gamma_1\alpha_1\delta^2\Lambda]+\sqrt{[\varepsilon\gamma_2(\alpha_1+\alpha_2)(\delta+\beta)^2-\gamma_1\alpha_1\delta^2\Lambda]^2-4\rho\varepsilon\gamma_2(\alpha_1+\alpha_2)(\delta+\beta)^2\alpha_1\delta^2\gamma_2\Lambda}}{2\varepsilon\gamma_2(\alpha_2+\alpha_2)(\delta+\beta)^2}\right]\right)}$$

$$C_1^* = \frac{\alpha_1\Lambda\left(\alpha_1+\alpha_2\right)^{-1}\left(\delta+\beta\right)^{-1}}{\left(1+\left[\frac{-[\varepsilon\gamma_2(\alpha_1+\alpha_2)(\delta+\beta)^2-\gamma_1\alpha_1\delta^2\Lambda]+\sqrt{[\varepsilon\gamma_2(\alpha_1+\alpha_2)(\delta+\beta)^2-\gamma_1\alpha_1\delta^2\Lambda]^2-4\rho\varepsilon\gamma_2(\alpha_1+\alpha_2)(\delta+\beta)^2\alpha_1\delta^2\gamma_2\Lambda}}{2\varepsilon\gamma_2(\alpha_2+\alpha_2)(\delta+\beta)^2}\right]\right)}$$

$$C_2^* = \frac{\alpha_1\delta\Lambda\left(\alpha_1+\alpha_2\right)^{-1}\left(\delta+\beta\right)^{-2}}{\left(1+\left[\frac{-[\varepsilon\gamma_2(\alpha_1+\alpha_2)(\delta+\beta)^2-\gamma_1\alpha_1\delta^2\Lambda]+\sqrt{[\varepsilon\gamma_2(\alpha_1+\alpha_2)(\delta+\beta)^2-\gamma_1\alpha_1\delta^2\Lambda]^2-4\rho\varepsilon\gamma_2(\alpha_1+\alpha_2)(\delta+\beta)^2\alpha_1\delta^2\gamma_2\Lambda}}{2\varepsilon\gamma_2(\alpha_2+\alpha_2)(\delta+\beta)^2}\right]\right)}$$

$$A^* = -\frac{\left[\varepsilon\gamma_2\left(\alpha_1+\alpha_2\right)\left(\delta+\beta\right)^2-\gamma_1\alpha_1\delta^2\Lambda\right]}{2\rho\varepsilon\gamma_2\left(\alpha_1+\alpha_2\right)\left(\delta+\beta\right)^2}$$
$$+\frac{\sqrt{\left[\varepsilon\gamma_2\left(\alpha_1+\alpha_2\right)\left(\delta+\beta\right)^2-\gamma_1\alpha_1\delta^2\Lambda\right]^2-4\rho\varepsilon\gamma_2\left(\alpha_1+\alpha_2\right)\left(\delta+\beta\right)^2\alpha_1\delta^2\gamma_2\Lambda}}{2\rho\varepsilon\gamma_2\left(\alpha_1+\alpha_2\right)\left(\delta+\beta\right)^2}$$

$$T^* = \frac{\varepsilon\left(-\frac{\left[\varepsilon\gamma_2(\alpha_1+\alpha_2)(\delta+\beta)^2-\gamma_1\alpha_1\delta^2\Lambda\right]+\sqrt{[\varepsilon\gamma_2(\alpha_1+\alpha_2)(\delta+\beta)^2-\gamma_1\alpha_1\delta^2\Lambda]^2-4\rho\varepsilon\gamma_2(\alpha_1+\alpha_2)(\delta+\beta)^2\alpha_1\delta^2\gamma_2\Lambda}}{2\rho\varepsilon\gamma_2(\alpha_1+\alpha_2)(\delta+\beta)^2}\right)}{\gamma_1\left(-\frac{[\varepsilon\gamma_2(\alpha_1+\alpha_2)(\delta+\beta)^2-\gamma_1\alpha_1\delta^2\Lambda]+\sqrt{[\varepsilon\gamma_2(\alpha_1+\alpha_2)(\delta+\beta)^2-\gamma_1\alpha_1\delta^2\Lambda]^2-4\rho\varepsilon\gamma_2(\alpha_1+\alpha_2)(\delta+\beta)^2\alpha_1\delta^2\gamma_2\Lambda}}{2\rho\varepsilon\gamma_2(\alpha_1+\alpha_2)(\delta+\beta)^2}\right)+\gamma_2}$$

# APPENDIX E

# MATERIAL MODEL PARAMETER VALUES

This appendix contains the parameter values for the material models used in each simulation. Each table lists the FLAG parameter notation, the parameter description and notation used in the related dissertation chapter, the parameter value, and units. Sources are listed in the table captions. If multiple sources were used for a model, citations appear within the table as well.

## E.1 Chapter 6

### *E.1.1 Perfect Plasticity Parameters*

| **FLAG Parameter** | **Description** | **Value** | **Units** |
|---|---|---|---|
| sm0 | shear modulus ($G$) | 2.8e10 [131] | Pa |
| yf | material flow stress ($\sigma_y$) | 2.9e8 [100] | Pa |
| tmelt | melt temperature ($T_m$) | 1220. [131] | K |

**Table E.1:** Perfect Plasticity Simulation Parameters for Al-6061 [100, 131].

The material saturation flow stress was not altered, and the default value is $10^{99}$ dyne/cm$^2$ [61].

### *E.1.2 Linear Hardening Parameters*

| **FLAG Parameter** | **Description** | **Value** | **Units** |
|---|---|---|---|
| sm0 | shear modulus ($G$) | 2.8e10 [131] | Pa |
| yf | initial yield stress ($\sigma_y$) | 2.9e8 [100] | Pa |
| tmelt | melt temperature ($T_m$) | 1220 [131] | K |
| yh | hardening parameter $\left(K\right)$ | 0.1 [131] | – |

**Table E.2:** Linear Hardening Simulation Parameters for Al-6061 [100, 131].

The material flow stress was not altered, and the default value in FLAG is $10^{99}$ dyne/cm$^2$ [61].

### *E.1.3 Johnson-Cook Parameters*

| FLAG Parameter | Description | Value | Units |
|---|---|---|---|
| sm0 | shear modulus ($G$) | 2.76e10 | Pa |
| a | quasistatic room temperature flow stress ($A$) | 2.44e8 | Pa |
| b | strain hardening effect ($B$) | 4.88e8 | Pa |
| c | strain-rate coefficient ($C$) | 0. | – |
| x_m | temperature exponent ($m$) | 3. | – |
| x_n | hardening exponent ($n$) | 0.5 | – |
| t_melt | melt temperature ($T_m$) | 1220. | K |
| t_ref | reference temperature ($T_0$) | 800. | K |

**Table E.3:** Johnson-Cook Simulation Parameters for Al-6061 [110].

No temperature-dependent specific heat was enabled. The material saturation flow stress was not listed and was thus not altered, and the default value in FLAG is $10^{99}$ Mbar [61].

#### *E.1.3.1 Steinberg-Guinan Parameters*

| FLAG Parameter | Description | Value | Units |
|---|---|---|---|
| r0 | reference density ($\rho_0$) | 2700. | $kg/m^3$ |
| sm0 | reference shear modulus ($G_0$) | 2.76e10 | Pa |
| y0 | reference yield strength ($Y_0$) | 0.29 | Pa |
| xn | work-hardening exponent ($n$) | 0.1 | – |
| yb | work-hardening coefficient ($\beta$) | 125. | – |
| yx | upper limit on hardening term ($Y_{\max}$) | 6.8e8 | Pa |
| au | pressure-dependence parameter $\left(\frac{G'_P}{G_0}\right)$ | 6.52e-13 | $Pa^{-1}$ |
| bu | temperature-dependence parameter $\left(\frac{G'_T}{G_0}\right)$ | 6.16e-4 | $K^{-1}$ |

**Table E.4:** Steinberg-Guinan Simulation Parameters for Al-6061 [130].

The relative heat capacity, initial plastic strain, minimum compression, melt shaping parameter for the shear modulus, and melt shaping parameter for the flow stress were not altered, and their default values in FLAG are 0. The maximum compression was not altered, and it's default value in FLAG is $10^{99}$ [61].

### *E.1.4 Preston-Tonks-Wallace Parameters*

| FLAG Parameter | Description | Value | Units |
|---|---|---|---|
| r | rate smoothing parameter ($r$) | 0. | – |
| p | Voce hardening law constant ($p$) | 3.0 | – |
| theta0 | initial strain hardening ($\theta$) | 1.84e-2 | – |
| kappa | temperature dependence constant $\kappa$ | 0.2 | – |
| gamma | strain dependence constant | 5.e-5 | – |
| alpha | temperature parameter ($\alpha$) | 0.475 | – |
| g0 | reference shear modulus ($G_0$) | 2.8e10 | Pa |
| tm | melt temperature ($T_m$) | 932. | K |
| am | average mass per atom ($M$) | 4.4967e-26 | kg |
| s0 | maximum $\hat{\tau}_s$ (at 0 K) ($s_0$) | 1.42e-2 | – |
| sinf | minimum $\hat{\tau}_s$ (near $T_m$) ($s_\infty$) | 8.56e-3 | – |
| y0 | maximum $\hat{\tau}_y$ (at 0 K) ($y_0$) | 8.98e-3 | – |
| y1 | material parameter $y_1$ | 1.42e-2 | – |
| y2 | material parameter $y_2$ | 0.4 | – |
| yinf | minimum $\hat{\tau}_y$ (near $T_m$) ($y_\infty$) | 5.96e-3 | – |
| beta | material exponent ($b$) | 0.23 | – |

**Table E.5:** Preston-Tonks-Wallace Simulation Parameters for Al-6061 [49].

The PTW parameter $\gamma_{\text{drag}}$ was not altered, and the FLAG default value is 0 [61].

## E.2 Chapter 7

### *E.2.1 Monel Steinberg-Guinan*

| FLAG Parameter | Description | Value | Units |
|---|---|---|---|
| r0 | reference density ($\rho_0$) | 8810. | kg/m$^3$ |
| sm0 | reference shear modulus ($G_0$) | 6.88e10 | Pa |
| y0 | reference yield strength ($Y_0$) | 8.3e8 | Pa |
| xn | work-hardening exponent ($n$) | 0.23 | – |
| yb | work-hardening coefficient ($\beta$) | 36. | – |
| yx | upper limit on hardening term ($Y_{\max}$) | 1.92e9 | Pa |
| au | pressure-dependence parameter $\left(\frac{G'_P}{G_0}\right)$ | 2.47e-11 | Pa$^{-1}$ |
| bu | temperature-dependence parameter $\left(\frac{G'_T}{G_0}\right)$ | 1.45e-4 | K$^{-1}$ |

**Table E.6:** Steinberg-Guinan Simulation Parameters for Monel [131].

The relative heat capacity, initial plastic strain, minimum compression, melt shaping parameter for the shear modulus, and melt shaping parameter for the flow stress

were not altered, and their default values in FLAG are 0. The maximum compression was not altered, and it's default value in FLAG is $10^{99}$ [61].

### *E.2.2 Iron Preston-Tonks-Wallace*

| FLAG Parameter | Description | Value | Units |
|---|---|---|---|
| r | rate smoothing parameter ($r$) | 0. | – |
| p | Voce hardening law constant ($p$) | 3.0 | – |
| theta0 | initial strain hardening ($\theta$) | 1.5e-2 | – |
| kappa | temperature dependence constant $\kappa$ | 0.35 | – |
| gamma | strain dependence constant | 1.e-5 | – |
| alpha | temperature parameter ($\alpha$) | 0.23 | – |
| g0 | reference shear modulus ($G_0$) | 8.72e10 | Pa |
| tm | melt temperature ($T_m$) | 1810. | K |
| am | average mass per atom ($M$) | 9.27e-26 | kg |
| s0 | maximum $\hat{\tau}_s$ (at 0 K) ($s_0$) | 1.e-2 | – |
| sinf | minimum $\hat{\tau}_s$ (near $T_m$) ($s_\infty$) | 2.5e-3 | – |
| y0 | maximum $\hat{\tau}_y$ (at 0 K) ($y_0$) | 6.625e-3 | – |
| y1 | material parameter $y_1$ | 6.625e-3 | – |
| y2 | material parameter $y_2$ | 0.265 | – |
| yinf | minimum $\hat{\tau}_y$ (near $T_m$) ($y_\infty$) | 7.5e-4 | – |
| beta | material exponent ($b$) | 0.265 | – |
| gam_drag | drag coefficient ($s_{\text{drag}}$) | 0.01 | – |

**Table E.7:** Preston-Tonks-Wallace Simulation Parameters for Iron [14].

### *E.2.3 Silicon Dioxide Perfect Plasticity*

| FLAG Parameter | Description | Value | Units |
|---|---|---|---|
| sm0 | shear modulus ($G$) | 2200. | Pa |
| yf | material flow stress ($\sigma_y$) | 1.108e8 | Pa |
| tmelt | melt temperature ($T_m$) | 1933.15 | K |

**Table E.8:** Perfect Plasticity Simulation Parameters for Al-6061 [2].

The material saturation flow stress was not altered, and the default value is $10^{99}$ dyne/cm$^2$ [61].

### *E.2.4 Nickel Steinberg-Guinan*

| **FLAG Parameter** | **Description** | **Value** | **Units** |
|---|---|---|---|
| r0 | reference density ($\rho_0$) | 8900. | $kg/m^3$ |
| sm0 | reference shear modulus ($G_0$) | 8.55e10 | Pa |
| y0 | reference yield strength ($Y_0$) | 0.14 | Pa |
| xn | work-hardening exponent ($n$) | 0.53 | – |
| yb | work-hardening coefficient ($\beta$) | 46. | – |
| yx | upper limit on hardening term ($Y_{\max}$) | 1.2e9 | Pa |
| au | pressure-dependence parameter $\left(\frac{G'_P}{G_0}\right)$ | 1.6e-13 | $Pa^{-1}$ |
| bu | temperature-dependence parameter $\left(\frac{G'_T}{G_0}\right)$ | 3.3e-4 | $K^{-1}$ |

**Table E.9:** Steinberg-Guinan Simulation Parameters for Nickel [130].

The relative heat capacity, initial plastic strain, minimum compression, melt shaping parameter for the shear modulus, and melt shaping parameter for the flow stress were not altered, and their default values in FLAG are 0. The maximum compression was not altered, and it's default value in FLAG is $10^{99}$ [61].

# APPENDIX F

# SIMULATION DETAILS

## F.1 Chapter 6 Simulations

### *F.1.1 Al-Al Verification: 1D*

Impactor: 1 km
Target: 10 km

| **Simulation** | |
|---|---|
| Zone size | 12.5 m (40 cppr) |
| Number of zones | 882 |
| Number of processors | 1 |
| ALE strategy | Lagrangian |
| EOS | Mie-Grüneisen |
| reference density | 2700 kg/m$^3$ [96] |
| specific heat | 890 J/kg/K [96] |
| sound speed | 5350 m/s [96] |
| $\gamma$ | 2. [96] |
| linear coefficient | 1.34 [96] |
| $q_2$ | 2. |
| $q_1$ | 0. |
| Boundary conditions | free |
| **Initialization** | |
| $\rho_0$ | 2700 kg/m$^3$ |
| $E_0$ | 0 J |

**Table F.1:** Simulation Details for Al-Al 1D Verification Problem

### *F.1.2 Al-Al Verification: 2D*

Impactor: Circle, diameter 1 km
Target: Rectangle, 10 km x 25 km
Air: Rectangle\impactor, 23.5 km x 25 km

| | 5 cppr | 10 cppr | 20 cppr | 40 cppr |
|---|---|---|---|---|
| Zone size | 100 m | 50 m | 25 m | 12.5 m |
| Number of zones | 84,920 | 337,340 | 1,344,680 | 5,369,360 |

**Table F.2:** Resolution Details for Al-Al 2D Mesh Resolution Study

| **Simulation** | |
|---|---|
| Number of processors (5 km/s) | 108 |
| Number of processors (20 km/s) | 144 |
| ALE strategy | geometry |
| Al EOS | SESAME |
| Al SESAME ID | 3317 |
| Air EOS | $\gamma$-law gas |
| reference density | 1.2922 kg/m$^3$ |
| $\gamma$ | 1.4 |
| $T_0$ | 273 K |
| $q_2$ (strengthless) | 2. |
| $q_1$ (strengthless) | 0. |
| $q_2$ (strength) | 1.3 |
| $q_1$ (strength) | 0.3 |
| Boundary conditions | free |
| **Initialization** | |
| Al (impactor and target) $\rho_0$ | 2700 kg/m$^3$ |
| Al (impactor and target) $E_0$ | 0 J |
| Air $\rho_0$ | 1.2922 kg/m$^3$ |
| Air $E_0$ | 0 J |

**Table F.3:** Simulation Details for Al-Al 2D Verification Problem

### *F.1.3 Al-Al Verification: 3D*

Impactor: Sphere, diameter 1 km
Target: Rectangular prism, 10 km x 25 km x 10 km
Air: Rectangular prism\impactor, 23.5 km x 25 km x 10 km

| **Simulation** | |
|---|---|
| Zone size | 100 m (5 cppr) |
| Number of zones | 8,659,500 |
| Number of processors | 360 |
| ALE strategy | geometry |
| Al EOS | SESAME |
| Al SESAME ID | 3317 |
| Air EOS | $\gamma$-law gas |
| $\rho_0$ | 1.2922 kg/m$^3$ |
| $\gamma$ | 1.4 |
| $T_0$ | 273 K |
| $q_2$ | 2. |
| $q_1$ | 0. |
| Boundary conditions | free |
| **Initialization** | |
| Al (impactor and target) $\rho_0$ | 2700 kg/m$^3$ |
| Al (impactor and target) $E_0$ | 0 J |
| Air $\rho_0$ | 1.2922 kg/m$^3$ |
| Air $E_0$ | 0 J |

**Table F.4:** Simulation Details for Al-Al 3D Verification Problem

#### *F.1.4 Glass-Water Validation*

Impactor: Semicircle, 2 mm diameter
Target: Rectangle, 36.75 cm x 21.75 cm
Air: Rectangle\impactor, 36.75 cm x 1000 cm

| **Simulation** | |
|---|---|
| Zone size min | 0.2 mm (5 cppr) |
| Zone size max | 5 mm (0.2 cppr) |
| Number of zones | 626,720 |
| Number of processors | 360 |
| ALE strategy | Eulerian |
| Glass EOS | SESAME |
| Glass SESAME ID | 3811 |
| Water EOS | SESAME |
| Water SESAME ID | 7153 |
| Air EOS | $\gamma$-law gas |
| $\rho_0$ | 0.0012922 g/cm$^3$ |
| $\gamma$ | 1.4 |
| $T_0$ | 273 K |
| $q_2$ | 2. |
| $q_1$ | 0. |
| Boundary conditions (top) | fixed |
| Boundary conditions (bottom) | fixed in $y$ |
| Boundary conditions (left, right) | fixed in $x$ |
| **Initialization** | |
| Glass $\rho_0$ | 2.24254 g/cm$^3$ |
| Glass $P_0$ | 1.e6 Barye |
| Water $\rho_0$ | 0.9998 g/cm$^3$ |
| Water $P_0$ | 1.e6 Barye |
| Air $\rho_0$ | 0.0012922 g/cm$^3$ |
| Air $P_0$ | 1.e6 Barye |

**Table F.5:** Glass-Water Validation Simulation Details

## F.2 Chapter 7 Simulations

### *F.2.1 2D Psyche*

Psyche: Semicircle, 125 km radius
Impactor: Semicircle, 5 km radius
Void: Rectangle\(Psyche $\cup$ Impactor), 500 km x 500 km

| **Simulation** | |
|---|---|
| Zone size | 330 m (∼15 cppr) |
| Number of zones | 2,301,285 |
| Number of processors | 180 |
| ALE strategy | Eulerian |
| Fe EOS | SESAME |
| Fe SESAME ID | 02140 |
| Monel EOS | Mie-Grüneisen |
| $\rho_0$ | 8810 kg/m$^3$ [131] |
| $c$ | 4190 m/s [131] |
| $b$ | 0.49 [131] |
| $\gamma$ | 1.95 [131] |
| linear coefficient | 1.54 [131] |
| Ni EOS | SESAME |
| Ni SESAME ID | 3101 |
| $SiO_2$ EOS | SESAME |
| $SiO_2$ SESAME ID | 7386 |
| $q_2$ (strengthless) | 2. |
| $q_1$ (strengthless) | 0. |
| $q_2$ (strength) | 1.3 |
| $q_1$ (strength) | 0.3 |
| Boundary conditions | axisymmetric (left), free |
| **Initialization** | |
| Fe $\rho_0$ | 7795.08121657211 kg/m$^3$ |
| Fe $E_0$ | 7.1761341305098e8 erg |
| Monel $\rho_0$ | 8800. |
| Monel $T_0$ | 273.0010219214762 |
| Ni $\rho_0$ | 8900 kg/m$^3$ |
| Ni $T_0$ | 298.15033511 |
| $SiO_2$ $\rho_0$ | 2200. |
| $SiO_2$ $P$ | 0 Pa |
| $SiO_2$ $T_0$ | 298 K |

**Table F.6:** 2D Psyche Simulation Details

### *F.2.2 3D Psyche*

Psyche: Shape model, spherical cap 110 km radius
Impactor: Sphere, 5 km radius
Void: Rectangular prism\(Psyche ∪ Impactor), 500 km x 500 km x 500 km

| **Simulation** | |
|---|---|
| Zone size min | 1000 m (5 cppr) |
| Zone size max | 10,000 m (0.5 cppr) |
| Number of zones | 33,382,400 |
| Number of processors | 1080 |
| ALE strategy | Eulerian |
| Monel EOS | Mie-Grüneisen |
| $\rho_0$ | 8810 kg/m$^3$ [131] |
| $c$ | 4190 m/s [131] |
| $b$ | 0.49 [131] |
| $\gamma$ | 1.95 [131] |
| linear coefficient | 1.54 [131] |
| $SiO_2$ $\rho_0$ | 2200. |
| $SiO_2$ $P$ | 0 Pa |
| $SiO_2$ $T_0$ | 298 K |
| $q_2$ (strengthless) | 2. |
| $q_1$ (strengthless) | 0. |
| $q_2$ (strength) | 1.3 |
| $q_1$ (strength) | 0.3 |
| Boundary conditions | fixed |
| Initialization | |
| Monel $\rho_0$ | 8800. |
| Monel $T_0$ | 273.0010219214762 |
| $SiO_2$ $P$ | 0 Pa |
| $SiO_2$ $T_0$ | 298 K |

**Table F.7:** 3D Psyche Simulation Details

# APPENDIX G

# THANKS

I began keeping a list of people to thank my first year. It is far too long to include in the Acknowledgments, so I will include it here. In no particular order: my Arizona acupuncturist Becky Coatsworth; my New Mexico acupuncturist Susan Grubb; Renate Mittleman; Mac Hyman; Roxana Bujack; Geoff Fairchild; Sara Del Valle; Jen May; Debbie Olson; Carl Gardner; Al Boggess; Erika Maestas; Tina Jenkins; Katrin Hammerling; all of XCP-1 at LANL; all of CCS-7 at LANL; the SoMSS staff; John Patchett; Gabe Rockefeller; Genevieve Toutain; Katie Kolossa; Curt Canada; Divya Banesh; Jim Ahrens; David Rogers; Linn Collins; Mark Schraad; Scott Doebling; Ed Dendy; Jessica Baumgaertel; Karen Tsai; Vitaly Ganusov; Remus Nicoara; Judy Day; Sarah El Jamous; Lauren (Johnson) Dickman; Elpiniki Nikolopoulou; the Lille family; Sherry Woodley; Ashely Duncan; Anne Gelb; Ami Radunskaya; Folashade Agusto; MSRI; my blonde math gals (A.J, Caro, and Robyn); Paloma Castillo-Gutierrez; Jason Yalim; Jorly Chatouphonexay; my ASU dance teachers (Carly, Jessica, Melissa); Erica Rutter; Rebecca Everett; Dan Korytowski; Bruce Pell; Andee Thatcher; Lindsey Gamard; Sergei Gavrillets; Eric Kostelich; Ken Knox; Andrew Bremner; Matthias Kawski; Leon Arriola; Stephen Webb; Thomas Callaghan; Leslie Hardcastle; my Tennessee acupuncturist Anita Hill; Jonathan Woodring; Francesca Samsel; Carrie Manore; Maria Pinila; Lois (Fire-Coyote) Smith; Lucas Zeppetello; everyone involved in the 2015 Computational Physics Summer Workshop; the Data Science at Scale School; Mela Hardin; Chris Paulson; Reuben Haynes; Joe Wells; Lauren Crider; SMB; AWM; AMS; Atomic Women; Stephen Lee; Krysten Pampel; Surani Joshua; Mandy Stevenson; Nicole Hamonic; Juliet Meggs; Jeff Springer; Alex Farrell; all of my students.